Astronomy & Astrophysics manuscript no. aa43782_arenou_Gaia
June 14, 2022

Gaia Data Release 3: Stellar multiplicity, a teaser for the hidden treasure

Authors: Gaia Collaboration , F. Arenou , C. Babusiaux , M.A. Barstow , S. Faigler , A. Jorissen , P. Kervella , T. Mazeh , N. Mowlavi , P. Panuzzo , J. Sahlmann , S. Shahaf , A. Sozzetti , N. Bauchet , Y. Damerdji , P. Gavras , P. Giacobbe , E. Gosset , J.-L. Halbwachs , B. Holl , M.G. Lattanzi , N. Leclerc , T. Morel , D. Pourbaix[†] , P. Re Fiorentin , G. Sadowski , D. Ségransan , C. Siopis , D. Teyssier , T. Zwitter , L. Planquart , A.G.A. Brown , A. Vallenari , T. Prusti , J.H.J. de Bruijne , M. Biermann , O.L. Creevey , C. Ducourant , D.W. Evans , L. Eyer , R. Guerra , A. Hutton , C. Jordi , S.A. Klioner , U.L. Lammers , L. Lindegren , X. Luri , F. Mignard , C. Panem , S. Randich , P. Sartoretti , C. Soubiran , P. Tanga , N.A. Walton , C.A.L. Bailer-Jones , U. Bastian , R. Drimmel , F. Jansen , D. Katz , F. van Leeuwen , J. Bakker , C. Cacciari , J. Castañeda , F. De Angeli , C. Fabricius , M. Fouesneau , Y. Frémat , L. Galluccio , A. Guerrier , U. Heiter , E. Masana , R. Messineo , C. Nicolas , K. Nienartowicz , F. Pailler , F. Riclet , W. Roux , G.M. Seabroke , R. Sordo , F. Thévenin , G. Gracia-Abril , J. Portell , M. Altmann , R. Andrae , M. Audard , I. Bellas-Velidis , K. Benson , J. Berthier , R. Blomme , P.W. Burgess , D. Busonero , G. Busso , H. Cánovas , B. Carry , A. Cellino , N. Cheek , G. Clementini , M. Davidson , P. de Teodoro , M. Nuñez Campos , L. Delchambre , A. Dell'Oro , P. Esquej , J. Fernández-Hernández , E. Fraile , D. Garabato , P. García-Lario , R. Haigron , N.C. Hambly , D.L. Harrison , J. Hernández , D. Hestroffer , S.T. Hodgkin , K. Janßen , G. Jevardat de Fombelle , S. Jordan , A. Krone-Martins , A.C. Lanzafame , W. Löffler , O. Marchal , P.M. Marrese , A. Moitinho , K. Muinonen , P. Osborne , E. Pancino , T. Pauwels , A. Recio-Blanco , C. Reylé , M. Riello , L. Rimoldini , T. Roegiers , J. Rybizki , L.M. Sarro , M. Smith , E. Utrilla , M. van Leeuwen , U. Abbas , P. Ábrahám , A. Abreu Aramburu , C. Aerts , J.J. Aguado , M. Ajaj , F. Aldea-Montero , G. Altavilla , M.A. Álvarez , J. Alves , F. Anders , R.I. Anderson , E. Anglada Varela , T. Antoja , D. Baines , S.G. Baker , L. Balaguer-Núñez , E. Balbinot , Z. Balog , C. Barache , D. Barbato , M. Barros , S. Bartolomé , J.-L. Bassilana , U. Becciani , M. Bellazzini , A. Berihuete , M. Bernet , S. Bertone , L. Bianchi , A. Binnenfeld , S. Blanco-Cuaresma , A. Blazere , T. Boch , A. Bombrun , D. Bossini , S. Bouquillon , A. Bragaglia , L. Bramante , E. Breedt , A. Bressan , N. Brouillet , E. Brugaletta , B. Bucciarelli , A. Burlacu , A.G. Butkevich , R. Buzzi , E. Caffau , R. Cancelliere , T. Cantat-Gaudin , R. Carballo , T. Carlucci , M.I. Carnerero , J.M. Carrasco , L. Casamiquela , M. Castellani , A. Castro-Ginard , L. Chaoul , P. Charlot , L. Chemin , V. Chiaramida , A. Chiavassa , N. Chornay , G. Comoretto , G. Contursi , W.J. Cooper , T. Cornez , S. Cowell , F. Crifo , M. Cropper , M. Crosta , C. Crowley , C. Dafonte , A. Dapergolas , P. David , P. de Laverny , F. De Luise , R. De March , J. De Ridder , R. de Souza , A. de Torres , E.F. del Peloso , E. del Pozo , M. Delbo , A. Delgado , J.-B. Delisle , C. Demouchy , T.E. Dharmawardena , S. Diakite , C. Diener , E. Distefano , C. Dolding , H. Enke , C. Fabre , M. Fabrizio , G. Fedorets , P. Fernique , F. Figueras , Y. Fournier , C. Fouron , F. Fragkoudi , M. Gai , A. Garcia-Gutierrez , M. Garcia-Reinaldos , M. García-Torres , A. Garofalo , A. Gavel , E. Gerlach , R. Geyer , G. Gilmore , S. Girona , G. Giuffrida , R. Gomel , A. Gomez , J. González-Núñez , I. González-Santamaría , J.J. González-Vidal , M. Granvik , P. Guillout , J. Guiraud , R. Gutiérrez-Sánchez , L.P. Guy , D. Hatzidimitriou , M. Hauser , M. Haywood , A. Helmer , A. Helmi , M.H. Sarmiento , S.L. Hidalgo , N. Hładczuk , D. Hobbs , G. Holland , H.E. Huckle , K. Jardine , G. Jasniewicz , A. Jean-Antoine Piccolo , Ó. Jiménez-Arranz , J. Juaristi Campillo , F. Julbe , L. Karbevska , S. Khanna , G. Kordopatis , A.J. Korn , Á Kóspál , Z. Kostrzewa-Rutkowska , K. Kruszyńska , M. Kun , P. Laizeau , S. Lambert , A.F. Lanza , Y. Lasne , J.-F. Le Campion , Y. Lebreton , T. Lebzelter , S. Leccia , I. Lecoeur-Taibi , S. Liao , E.L. Licata , H.E.P. Lindstrøm , T.A. Lister , E. Livanou , A. Lobel , A. Lorca , C. Loup , P. Madrero Pardo , A. Magdaleno Romeo , S. Managau , R.G. Mann , M. Manteiga , J.M. Marchant , M. Marconi , J. Marcos , M.M.S. Marcos Santos , D. Marín Pina , S. Marinoni , F. Marocco , D.J. Marshall , L. Martin Polo , J.M. Martín-Fleitas , G. Marton , N. Mary , A. Masip , D. Massari , A. Mastrobuono-Battisti , P.J. McMillan , S. Messina , D. Michalik , N.R. Millar , A. Mints , D. Molina , R. Molinaro , L. Molnár , G. Monari , M. Monguió , P. Montegriffo , A. Montero , R. Mor , A. Mora , R. Morbidelli , D. Morris , T. Muraveva , C.P. Murphy , I. Musella , Z. Nagy , L. Noval , F. Ocaña , A. Ogden , C. Ordenovic , J.O. Osinde , C. Pagani , I. Pagano , L. Palaversa , P.A. Palicio , L. Pallas-Quintela , A. Panahi , S. Payne-Wardenaar , X. Peñalosa Esteller , A. Penttilä , B. Pichon , A.M. Piersimoni , F.-X. Pineau , E. Plachy , G. Plum , E. Poggio , A. Prša , L. Pulone , E. Racero , S. Ragaini , M. Rainer , C.M. Raiteri , P. Ramos , M. Ramos-Lerate , S. Regibo , P.J. Richards , C. Rios Diaz , V. Ripepi , A. Riva , H.-W. Rix , G. Rixon , N. Robichon , A.C. Robin , C. Robin , M. Roelens , H.R.O. Rogues , L. Rohrbasser ,

M. Romero-Gómez , N. Rowell , F. Royer , D. Ruz Mieres , K.A. Rybicki , A. Sáez Núñez , A. Sagristà Sellés , E. Salguero , N. Samaras , V. Sanchez Gimenez , N. Sanna , R. Santoveña , M. Sarasso , M.S. Schultheis , E. Sciacca , M. Segol , J.C. Segovia , D. Semeux , H.I. Siddiqui , A. Siebert , L. Siltala , A. Silvelo , E. Slezak , I. Slezak , R.L. Smart , O.N. Snaith , E. Solano , F. Solitro , D. Souami , J. Souchay , A. Spagna , L. Spina , F. Spoto , I.A. Steele , H. Steidelmüller , C.A. Stephenson , M. Süveges , J. Surdej , L. Szabados , E. Szegedi-Elek , F. Taris , M.B. Taylor , R. Teixeira , L. Tolomei , N. Tonello , F. Torra , J. Torra[†] , G. Torralba Elipe , M. Trabucchi , A.T. Tsounis , C. Turon , A. Ulla , N. Unger , M.V. Vaillant , E. van Dillen , W. van Reeven , O. Vanel , A. Vecchiato , Y. Viala , D. Vicente , S. Voutsinas , M. Weiler , T. Wevers , Ł. Wyrzykowski , A. Yoldas , P. Yvard , H. Zhao , J. Zorec , S. Zucker

[1]

ABSTRACT

Context. The *Gaia* DR3 Catalogue contains for the first time about eight hundred thousand solutions with either orbital elements or trend parameters for astrometric, spectroscopic and eclipsing binaries, and combinations of them.
Aims. This paper aims to illustrate the huge potential of this large non-single star catalogue.
Methods. Using the orbital solutions together with models of the binaries, a catalogue of tens of thousands of stellar masses, or lower limits, partly together with consistent flux ratios, has been built. Properties concerning the completeness of the binary catalogues are discussed, statistical features of the orbital elements are explained and a comparison with other catalogues is performed.
Results. Illustrative applications are proposed for binaries across the H-R diagram. The binarity is studied in the RGB/AGB and a search for genuine SB1 among long-period variables is performed. The discovery of new EL CVn systems illustrates the potential of combining variability and binarity catalogues. Potential compact object companions are presented, mainly white dwarf companions or double degenerates, but one candidate neutron star is also presented. Towards the bottom of the main sequence, the orbits of previously-suspected binary ultracool dwarfs are determined and new candidate binaries are discovered. The long awaited contribution of Gaia to the analysis of the substellar regime shows the brown dwarf desert around solar-type stars using true, rather than minimum, masses, and provides new important constraints on the occurrence rates of substellar companions to M dwarfs. Several dozen new exoplanets are proposed, including two with validated orbital solutions and one super-Jupiter orbiting a white dwarf, all being candidates requiring confirmation. Beside binarity, higher order multiple systems are also found.
Conclusions. By increasing by more than one order of magnitude the number of known binary orbits, *Gaia* DR3 will provide, beside a rich reservoir of dynamical masses, an important contribution to the analysis of stellar multiplicity.

Key words. stars: binaries: general – astrometry – stars: brown dwarfs – stars: planetary systems – stars: fundamental parameters – catalogues

1. Introduction

The success of *Gaia* (Gaia Collaboration et al. 2016b), with parallaxes for around 1.5 billion sources, could overshadow how difficult the path to measuring the first stellar distances was. The two millennia during which this research has been unsuccessfully carried out have been littered with unrelated but equally fundamental discoveries. In particular, Herschel, following the suggestion by Ramponi to Galileo in 1611 (Siebert 2005), observed pairs of stars in order to measure their differential parallaxes, but did not succeed. Instead, what he demonstrated for the first time, in 1802, was the existence of orbits for these stars, changing their nature from unrelated double stars to binaries, proving that the law of gravitation was universal.

After Bessel had obtained the first convincing parallax measurement in 1838, he also deduced in 1844 from the nonlinear proper motion of Sirius and Procyon that there could exist not only visual binaries but also invisible, now called astrometric, binaries. Astrometry and binarity have then been intimately linked from the start. Indeed, it was not until much later, by observing the periodic Doppler shift of Algol's lines, that Vogel correctly deduced in 1889 that this was due to its orbital motion, making Algol the first spectroscopic binary. In fact, Algol had been suspected by John Goodricke in 1782 to be periodically eclipsed, making this star also the first eclipsing binary (Leverington 1995).

Since then, it has been realised that binary stars were not only important to derive their physical properties but also due to their fundamental role in stellar evolution; understanding the statistical properties of binary and multiple stars is then an important ingredient for the knowledge of our Galaxy. The properties of companions down to the substellar regime is another key to understanding stellar formation. Unfortunately, until now, too small samples, selection effects, and also the absence of the required astrometric precision, have always complicated the analysis of the various existing ground-based data.

As a large survey, *Gaia* should be in an ideal place to bring a newer, much broader perspective to these fundamental topics. What makes *Gaia* so unique is its ability to find, and above all to parameterise, most types of binaries at once, whether visual, astrometric, spectroscopic or eclipsing and even through stellar parametrisation, with a remarkable homogeneity of epoch, level of calibration accuracy, data reduction and process organisation.

The *Gaia* precursor, Hipparcos, had already discovered and measured double stars (Lindegren 1997), mostly resolved ones but also several categories of unresolved astrometric binaries, which allowed to determine stellar masses (Söderhjelm et al. 1997; Martin et al. 1997) though for a small number of sources only.

With the successive *Gaia* DR1 (Gaia Collaboration et al. 2016a), DR2 (Gaia Collaboration et al. 2018b) then EDR3 (Gaia Collaboration et al. 2021a), the multiple stars had not yet been handled, the difficulty to analyse the single stars being already

a challenge, these successive releases representing the improvement of the calibrations and source analysis. This does not mean that non-single stars were absent. Whether double or binaries, they are indeed present and processing them as single stars seriously degrades their results, although, fortunately, several flags in the *Gaia* Catalogue inform about the potential duplicity. Beside, the combination of these first *Gaia* releases with Hipparcos data already allowed to detect long period binaries (Kervella et al. 2019a, 2022; Brandt 2021).

The advent of *Gaia* DR3 (Gaia Collaboration et al. 2022b) now presents impressive new data products among which, to quote a few only, variability (Eyer et al. 2022), radial velocities (Katz et al. 2022), astrophysical parameters (Creevey et al. 2022) determined using either high-resolution (RVS) and low-resolution data (BP-RP photometers, De Angeli et al. 2022), for a very large fraction of the Catalogue. *Gaia* DR3 also contains the first analysis of the unresolved binary star contents covering the typical binary classes (astrometric, spectroscopic, photometric) presented into several tables: two-body orbits, astrometric or spectroscopic accelerations, variable binaries. These tables contain the orbital or trend parameters of the found binaries. Above all this offers the prospect of deriving the physical properties of the individual components. Marginally, this should also improve the measurements of these systems in the main catalogue, with better astrometric parameters or systemic radial velocity.

Although the maturity of the analysis of *Gaia* data now makes it possible to obtain for the first time a multi-type catalogue of binaries much larger than has been compiled with difficulty over the previous centuries, it must be stressed that only a small fraction of the binary content of the main catalogue has been analysed for DR3. This data analysis is described in the documentation (Pourbaix & et al. 2022)[1] and the articles accompanying this data release, namely Halbwachs et al. (2022); Holl et al. (2022b); Gosset (2022); Mowlavi et al. (2022); Siopis (2022).

The purposes of this publication are manyfold. It is first intended to describe the possible use cases of the catalogue, illustrating in particular the potential complementarity of the different data processing chains. This is essentially an appetiser that shows the quality of the data, highlighting the basic results that can be readily obtained, in particular estimating masses, these ones not being part of the non-single star tables. Beside, this performance verification paper acts as a final validation step before releasing the data. It is outside of the scope to explore the data in detail, nor to compare it to models, nor to confirm candidates of various kind, as this will be the goal of the scientific exploitation by the community, but we wish to facilitate this exploitation by describing what has been learned from the analysis so far.

We start by describing the data content, then useful statistical properties are clarified together with what is known about the selection function. We then focus on orbits, not acceleration solutions (for astrometry), nor trend solutions (for spectroscopic binaries) and propose for these orbital solutions a catalogue of masses. From this, we present an impressionistic panorama of the potential that lies inside this catalogue, concerning basic statistical properties and candidate sources of various types e.g. EL CVn, compact companions, white dwarfs or high mass ones, then ultracool dwarfs and substellar companions. Multiple systems are finally discussed.

[1] `https://gea.esac.esa.int/archive/documentation/GDR3/index.html`

2. Data description

2.1. Table contents

The non-single star (NSS) tables are presented more by type of solution or period range rather than by kind of binaries. The first of the four tables, `nss_two_body_orbit`, contains the orbital parameters for all three categories, astrometric, spectroscopic or eclipsing binaries, all being unresolved. The table `nss_acceleration_astro` contains accelerations or derivatives of it for sources that have an astrometric motion better described using a quadratic or cubic rather than a linear proper motion. Similarly, the `nss_non_linear_spectro` are trend (long period) solutions of spectroscopic binaries. The solutions in the `nss_vim_fl` table are different in that the photocentre displacement due to the photometric variability of one component of fixed binaries required the correction of the astrometric parameters (variable-induced movers fixed, `VIMF`). A summary of the solutions is given Table 1.

The astrometric orbits in the `nss_two_body_orbit` table have a `nss_solution_type` name starting with `Orbital*` and the orbital parameters are described at Appendix B.1. The spectroscopic binaries with either one component being parametrised (`SB1`) or both (`SB2`) have their parameters described at Appendix B.2 and short periods may have a circular solution (`nss_solution_type = SB1C`). As a source may simultaneously be e.g. astrometric binary and spectroscopic binary, combined solutions have been computed in some cases (`nss_solution_type = AstroSpectroSB1`). For the same reason, the `EclipsingSpectro` solutions are combinations of eclipsing and spectroscopic solutions. However, when no combination has been done, then two solutions for the same source may be present in the `nss_two_body_orbit` table, i.e. a query by `source_id` may return several solutions. These multiple solutions may indicate either triple systems, or some inconsistency that users may wish to sort out, and then possibly combine these solutions offline.

For the same reason, some sources may also have solutions in several tables simultaneously. To take an example, there are 160 eclipsing binaries having also a `VIMF` solution. As the `VIMF` model should have improved their astrometric solution, and distance of eclipsing binaries is of interest, this solution should in principle be preferred over the one given in the `gaia_source` table.

This potential multiplicity of solutions for a given source explains the total number of unique NSS sources being 813 687 while the total number of NSS solutions is larger, 839 098.

The distributions of the various orbital solutions with magnitude are shown Fig. 1. As expected, the brightest are the SB1 and SB2, and consequently also their intersection with astrometric binaries, `AstroSpectroSB1`, and with eclipsing binaries, `EclipsingSpectro`. The orbital astrometric binaries, brighter than $G < 19$, peak at $G \approx 14$ while the `OrbitalTargetedSearch` span the entire magnitude range as the sources were given as input list. The eclipsing binaries are the faintest. Note that the NSS eclipsing binaries are a small subset of the ones detected by photometry (Mowlavi et al. 2022), for which an orbital solution has been computed (Siopis 2022), cf. the much more complete `vari_eclipsing_binary` table.

The distribution of periods, by construction restricted to the `nss_two_body_orbit` table, is depicted in Fig. 2. The short period eclipsing and long period astrometric binaries are nicely bridged by the SBs. In clear, within a few years *Gaia* has covered the impressive 0.28 − 1500 day period range (99% CI) for thousands of sources, that should prove very valuable for the statistics of binary properties. The coverage in the joint distribution of period and magnitude is qualitatively illustrated Fig. 3.

Table 1. Content of the four non-single star tables.

Table	nss_solution_type	Solutions	Description
nss_acceleration_astro	Acceleration7	246 947	Second derivatives of position (acceleration)
	Acceleration9	91 268	Third derivatives of position (jerk)
nss_two_body_orbit	Orbital	134 598	Orbital astrometric solutions
	OrbitalAlternative*	629	Orbital astrometric, alternative solutions
	OrbitalTargetedSearch*	533	Orbital astrometric, supplementary external input list
	AstroSpectroSB1	33 467	Combined orbital astrometric + spectroscopic solutions
	SB1 or SB2	186 905	Orbital spectroscopic solutions
	EclipsingSpectro	155	Combined orbital spectroscopic + eclipsing solutions
	EclipsingBinary	86 918	Orbits of eclipsing binaries
nss_non_linear_spectro	FirstDegreeTrendSB1	24 083	First order derivatives of the radial velocity
	SecondDegreeTrendSB1	32 725	Second order derivatives of the radial velocity
nss_vim_fl	VIMF	870	Variable-induced movers fixed

Notes. The number of solutions is larger than the number of sources. The type of solution OrbitalAlternative* indicates solutions which are either OrbitalAlternative or OrbitalAlternativeValidated.

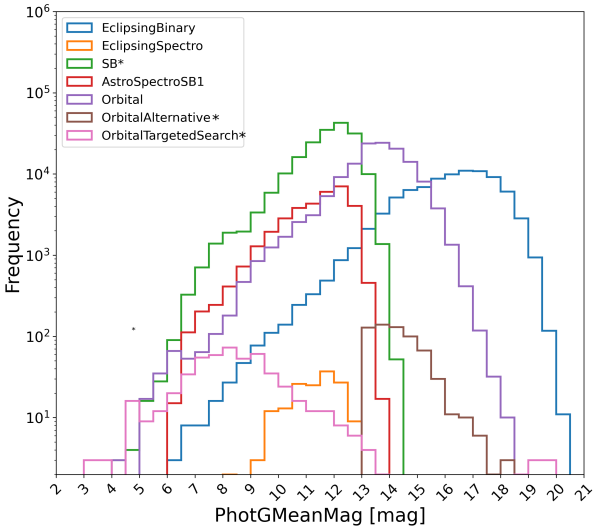

Fig. 1. Magnitude distribution for each solution type in the nss_two_body_orbit table.

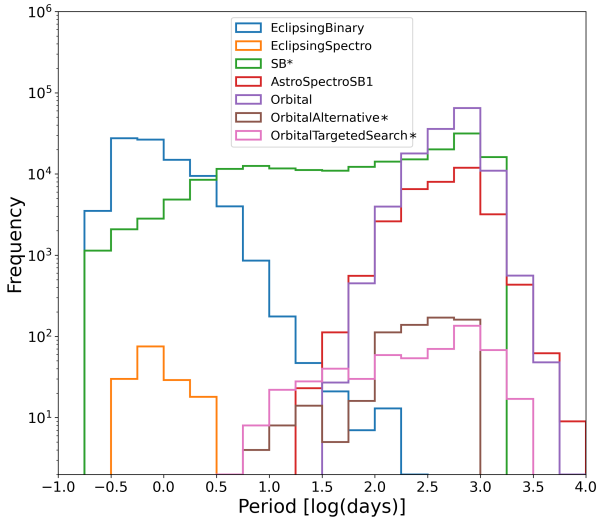

Fig. 2. Number of solutions for each solution type in the nss_two_body_orbit table as a function of period.

The Hertzsprung-Russell diagrams (HRD) for the various categories are represented Fig. 4, for sources with a parallax S/N > 5. Note that the used parallax is the one from the NSS solution for what concerns the putative astrometric binaries, while it is the one from the main catalogue for spectroscopic and eclipsing binaries.

2.2. Table construction

Although we refer to the online documentation and the articles accompanying this data release for a detailed understanding of the data processing, it is of interest to describe how the non-single star data have been obtained, starting with their input data selection, as this is one first key to understand the non-single star selection function.

The basic NSS processing selected its input sources from those that had a bad goodness of fit (GoF) in the upstream results, either in the astrometric or in the spectroscopic processing, or that were detected as eclipsing variables; the only exception is the OrbitalTargetedSearch, Sect. 2.2.2, where a predefined source list was given as input to the astrometric orbital fit, irrespective of their actual GoF in the single star solution.

2.2.1. Astrometric binaries, main processing

As *Gaia* DR3 is the first publication of NSS solutions, it was decided to limit the content to the most significant ones, this criterion being relaxed for further releases, and the motivation for this will appear later. The definition of the input source list started after *Gaia* DR2, where it was assumed that the sources with ruwe > 1.4 represented a reasonable threshold for sources with problematic astrometric solutions[2]. More recent analysis (e.g. Penoyre et al. 2021) may now suggest that a lower threshold could have been chosen, but this value also had the advantage to decrease the processing requirements.

[2] cf. Gaia DR2 documentation

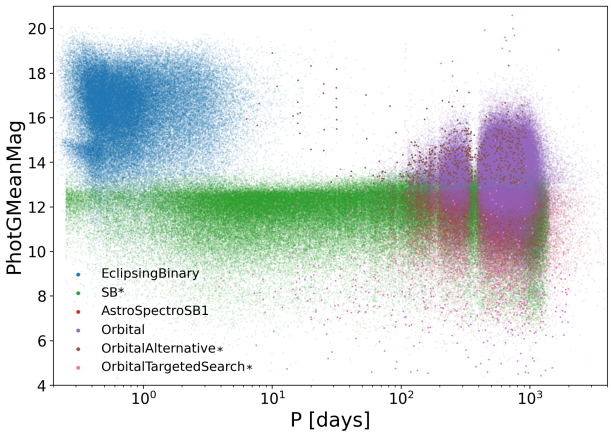

Fig. 3. G apparent magnitude vs period in the `nss_two_body_orbit` table.

To this `ruwe` > 1.4 criterion, $G < 19$ was added in order to keep the best signal-to-noise. Obviously, the sample defined like this contains many contaminants, partially resolved rather than unresolved sources. In particular, for a double star with a projected separation between components between ≈ 9 mas and ≈ 0.27″(Lindegren 2022), depending on the magnitude difference, the epoch position is not exactly on the photocentre[3], so that the astrometry of such sources is perturbed and the source is likely to have been selected.

Consequently the criteria `ipd_frac_multi_peak` ≤ 2 was added to avoid double stars with a large separation and `ipd_gof_harmonic_amplitude` < 0.1 to reject pairs with smaller separations. The `visibility_periods_used` > 11 criteria was also added (> 12 for orbital solutions), in order to avoid spurious solutions. [4]

It was found however that the sample was still polluted so another criterion was added, this time based on photometry, trying to avoid sources with light being contaminated by a neighbour. For this purpose, it was made use of the corrected BP and RP flux excess factor C^* associated to its uncertainty $\sigma_{C^*}(G)$ as defined by Riello et al. (2021, Eqs. 6 and 18), drastically keeping sources with $|C^*| < 1.645\sigma_{C^*}$ only.

2.2.2. Astrometric binaries, alternative processing

As described in Holl et al. (2022b), alternative orbit determination algorithms have been run on two different input lists. The first one is based on astrometric binaries that could not be successfully modelled by any model in the main processing pipeline, for which a more complex handling was attempted, `nss_solution_type = OrbitalAlternative*`. These sources originate from the same list as described in Sect. 2.2.1. The second one is constituted by a sample of sources with detected companions published in the literature, `nss_solution_type = OrbitalTargetedSearch*`, where all sources have been kept for processing.

[3] We coined the word 'Gaiacenter' in Kervella et al. (2022) by analogy with the 'Hippacenter' defining the actual pointing of the epoch Hipparcos observations of double stars (Martin et al. 1997)

[4] Although the DoF is still large enough as there are on the average about 18 astrometric observations per visibility period, one may still be cautious with solutions having a low number of visibility periods.

2.2.3. Spectroscopic binaries

The selection of the sources that had to be treated by the spectroscopic binary pipeline was based on sources with enough measurements, a dispersion of these measurements large enough, rejecting stars of stellar type outside of range, viz. `rv_renormalised_gof` > 4 and `rv_nb_transits` ≥ 10 and 3875 K <`rv_template_teff` < 8125 K, or detected as SB2.

One may notice that there are more than six thousands sources with a SB solution that have no average radial velocity in the `gaia_source` main catalogue. In that case (as in the other cases where a SB solution is given), the `center_of_mass_velocity` gives the systemic velocity. The absence of a mean RV for what concerns SB2s is normal, as the main spectroscopic processing did not compute this value. For SB1s, it may be useful to note that the computation had not been performed for the sources that were considered either peculiar, or potentially SB2, too hot or with emission lines. Consequently, when some SB results appear doubtful, it may then be useful to check whether `gaia_source.radial_velocity is NULL` for these sources. More details are given in Gosset (2022).

2.2.4. Eclipsing binaries

The input list for candidate eclipsing binaries contained about two millions sources that can be found in the `vari_eclipsing_binary` *Gaia* DR3 table. Their selection is described in Mowlavi et al. (2022); see also the online documentation. The selection of the subset therein for which an orbital solution has been computed is described in Siopis (2022).

2.3. Output filtering

Once the first processing results were analysed, it appeared that the cleaning of the input list had still left a very large fraction of spurious solutions. This is why it was decided to keep the most significant solutions for *Gaia* DR3: a general filter was applied to keep those with goodness of fit smaller than 50 and significance > 5 (> 2 for `OrbitalTargetedSearch*`). The `significance` is computed as the S/N ratio of the semi-major axis for astrometric orbits, (a_0/σ_{a_0}), on the S/N ratio of the acceleration module for acceleration solutions, and of the semi-amplitude for spectroscopic binaries, (K_1/σ_{K_1}). Supplementary filtering was applied during the processing or at post-processing level as described for the various models below.

Astrometric binaries, acceleration solutions: One could naively hope that the estimated accelerations would allow to detect binaries of intermediate period and provide some useful information about the binary, e.g. the minimum mass producing the given acceleration on the primary. The situation appears actually more complex. The acceleration values themselves are not discussed, and it can be seen that these solutions improve the baseline solution, e.g. looking at a slightly thinner giant branch for an HRD produced using the parallaxes from the acceleration solution, compared to those from the main catalogue. What is at stake is the interpretation of the acceleration term.

What happens is the combination of two effects. The first one originates from the organisation of the NSS processing: acceleration solutions were attempted before any other solutions, and kept if significant enough with a reasonable GoF. The (unwanted) effect is that some solutions which could have received a full orbit parametrisation were not attempted and appear in the

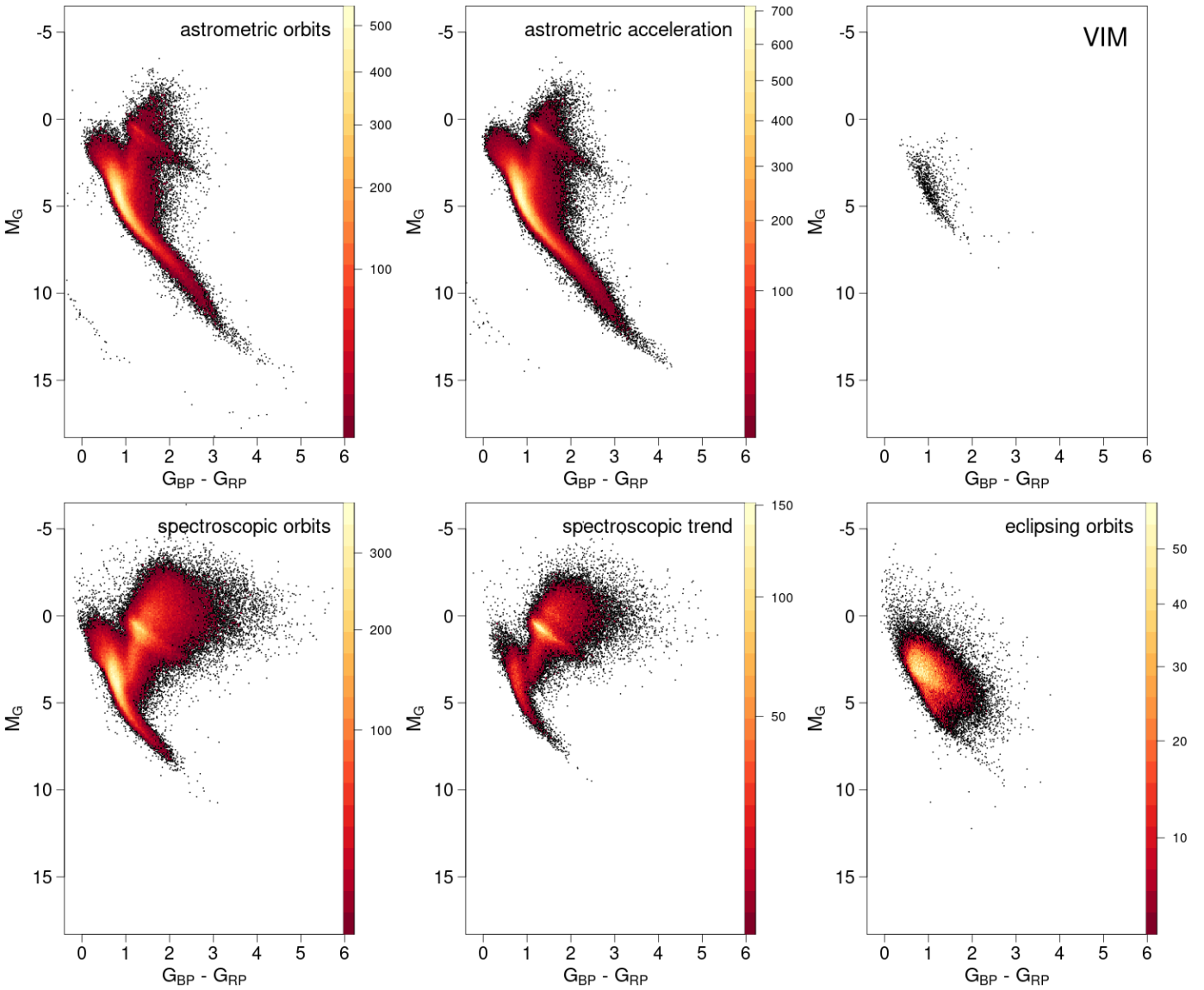

Fig. 4. *Gaia* H-R diagram, uncorrected for extinction, for all NSS solutions with a relative parallax error better than 20%. No selection is done on the photometric quality. The colour scale represents the square root of the relative density of stars. *Top*: Astrometric binaries, (a): `all Orbital* solutions plus AstroSpectroSB1`, (b): `Acceleration` solutions, (c): `VIMF`; *Bottom*: Spectroscopic binaries with (d): `SB*` orbits and (e): `NonLinearSpectro`, (f): eclipsing binaries.

NSS catalogue with an acceleration solution instead. The second effect is that an acceleration term can be significant even for short periods or very long periods. This is demonstrated by the analysis in Lindegren (2022).

The following filtering has been applied (see documentation and Halbwachs et al. 2022, for details): the sources which have been kept were those with significance $s > 20$ and $\varpi/\sigma_\varpi > 1.2\ s^{1.05}$ and GoF < 22 for `Acceleration7` and $\varpi/\sigma_\varpi > 2.1\ s^{1.05}$ and GoF < 25 for `Acceleration9`.

Nevertheless, it is known that a large fraction of the acceleration solutions are not intermediate period binaries as one would expect, rather short or long periods instead.

Astrometric binaries, `Orbital` solutions: The processing of orbital solutions starts by a period search. Unfortunately, this may lead to the detection of periods related to the scan law, rather than due to some true periodic motion: partially resolved objects with fixed position may give a signal depending on the scanning angle with respect to the orientation of the pair. This problem is fully analysed in Holl et al. (2022a). Consequently, most detected periods below $\approx$ 100 days were wrong, leading to solutions with huge and wrong mass functions.

To circumvent this, the following filtering was adopted (Halbwachs et al. 2022): parallax S/N $>$ 20000/`period`, `significance` $s = a_0/\sigma_{a_0} > 5$ and $s > 158/\sqrt{\texttt{period}}$, `eccentricity_error` $< 0.182 * \log_{10}(\texttt{period}) - 0.244$.

Astrometric binaries, alternative processing: Aggressive post-processing filtering approaches for both samples produced subsets of solutions that were assigned `OrbitalAlternative*` and `OrbitalTargetedSearch*` solution types, respectively, in the *Gaia* DR3 archive. For both cases, subsamples of sources that passed a variety of validation procedures were further assigned `OrbitalAlternativeValidated` and

`OrbitalTargetedSearchValidated` solution types (See Holl et al. 2022b, for details).

Inspection of the `OrbitalAlternative` solutions reveals that the caveat of unrealistically large inferred companion masses at short orbital periods is not entirely removed. A few percent of spurious solutions still likely contaminates this sample.

Spectroscopic binaries: Only the sources with GoF < 3, $|$`center_of_mass_velocity`$| < 1000\,\mathrm{km\,s^{-1}}$, $K_1 < 250\,\mathrm{km\,s^{-1}}$and `efficiency` > 0.1 were kept, where `efficiency` is a measure of the correlation between parameters..

One of the most important problems found after processing was the presence of many spurious SB detections with short periods. For this reason, the lower confidence threshold on the period was adapted depending on the period itself: it was set to 0.995 for $P < 1$ d, 0.95 for $P > 10$ d, and $-0.045 \log P + 0.995$ in between. For details on this and other filtering during the spectroscopic processing, see Gosset (2022).

Despite all this, the comparison of NSS results with catalogues of known binaries shows that for a few percent of the SB1 solutions the period may still be wrong, mainly due to the sparse time sampling. When these sources have both an `SB1` and `Orbital` solution, such cases may be spotted by comparing the respective semi-amplitudes. Short periods with large `ruwe` (e.g. > 1.4) are frequently suspect; some may be the inner system of a triple system, but most may instead be some kind of aliases of a longer orbital solution.

Inspecting the SB1 solutions, it can be noted an overdensity of solutions with periods around the precession period (62.97 days), in particular by selecting sources with large astrometric excess noise (see Fig. 5). These solutions are spurious, due to an offset in the astrometric coordinates, which generates a spurious variation of the computed epoch radial velocities, which depends on the scanning angle and thus with a periodicity linked to the precession of the satellite. The inaccuracy of their astrometric coordinates is most probably due to the fact that they are partially resolved binaries/double stars, which is confirmed by the fact that we see this overdensity also selecting sources with `ipd_frac_multi_peak` > 20. Holl et al. (2022a) describes the effect of the scanning law on the NSS solutions in more detail.

Spurious SB1 solutions can be also generated by pulsation of the source, like in RR Lyrae and Cepheids. In many cases, the SB1 solution will have the same period of the pulsation, but in other cases, due to the sparse sampling, the pipeline can find a keplerian fitting solution at a different, typically shorter, period. During the release validation, SB1 solutions of sources identified by *Gaia* as RR Lyrae or Cepheids were removed from the release.

Another cause generating spurious SB1 solutions is the contamination from nearby brighter star. As explained in Seabroke et al. (2021), and noted in Boubert et al. (2019), the RVS spectrum of sources extracted at a given transit can be contaminated by a nearby source, producing spurious values of the radial velocity. In *Gaia* DR3, the RVS pipeline includes a deblending algorithm, which is however limited to spectra with overlapping windows (see Seabroke et al. 2021, for details).

Eclipsing binaries: At post-processing, only the sources with $0.2 <$ `efficiency` ≤ 1 and `g_rank` ≥ 0.6 were kept, where the rank is a measure of the quality of the fit. See the online documentation (Pourbaix & et al. 2022, Sect. 7.6) for details.

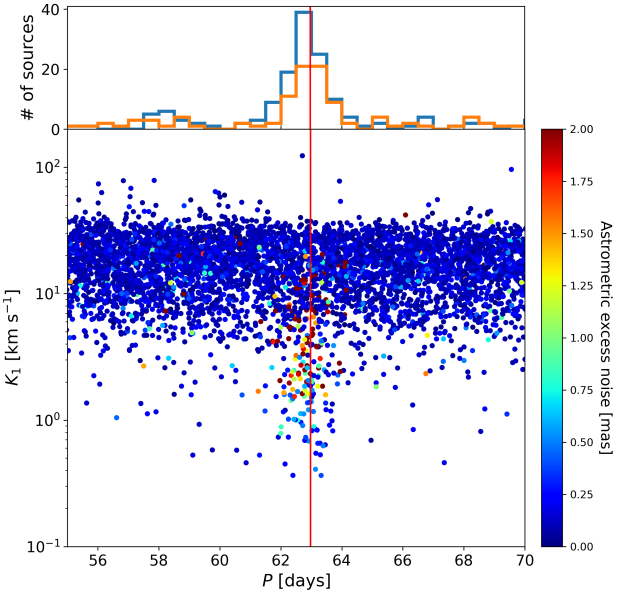

Fig. 5. The K_1 semi-amplitude versus period diagram of `SB1` solutions, colour-coded according to their `astrometric_excess_noise`. The diagram shows the presence of an overdensity of solutions at periods near the precession period (marked with a vertical line) with large astrometric excess noise. The histogram of the top shows the density of solutions with astrometric excess noise larger than 1 mas (blue line) and of those with `ipd_frac_multi_peak` > 20 (orange line).

3. Completeness

The resulting non-single star dataset is the result of a selection process in three successive steps:

1. The selection of the input list, discussed Sect. 2.2;
2. The sources for which the orbital motion can be preferentially detected by the processing;
3. The filtering done at post processing, indicated Sect. 2.3 .

In this section, we give some indications concerning the second step. One main reason for the expected non-uniformity of orbit detections is the number of observations and their temporal distribution. As this is governed by the scanning law of the *Gaia* satellite, see e.g. Fig. 7, this should appear clearly on a sky plot, and this is discussed Sect. 3.1.

However, even with a given set of observations, all orbits are not created equal. First, the period distribution of astrometric orbits shows a prominent lack of solutions around one year, which was expected for long due to the difficulty to decouple the orbital from the parallactic effect. There are other more subtle biases depending on the orbit itself which are discussed Sect. 3.2.

The distribution of solutions is finally discussed within the 100 pc horizon at Sect. 3.3 and the completeness is also studied for Hipparcos stars Sect. 4.2.2.

3.1. Sky distribution

Over the sky, the distribution of the various solution types shows the expected higher density along the galactic plane together with a larger excess at high ecliptic latitudes around $l \pm 100°$. The latter is due to a larger number of observations, and thus to a larger probability of detecting periodically variable motions.

This tells however little about whether the (in)completeness is uniform over the sky. Although we may have e.g. more eclips-

ing binaries among young stars, let us assume for a moment that F, the true (unknown) fraction of binaries, is uniform over the sky, and that our NSS samples are roughly complete up to some given magnitude $G_{\rm max}$.

Dividing up the sky in healpix (Górski et al. 2005) level 4 equal-area pixels, we note N_j the number of sources up to $G < G_{\rm max}$ in the full *Gaia* catalogue in a given healpix cell j, and n_j the corresponding number of NSS of a given type up to $G < G_{\rm max}$. With $f = {\rm med}(n_j/N_j)$ the empirical median of the ratio over the sky as estimate of F, we call 'sky density factor' $d_j = \frac{n_j}{f\,N_j}$. This factor gives the up or down factor of the average NSS fraction and should be a noisy value around 1 if F is approximately constant over the sky.

Fig. 6 shows the sky density factor for several solution types truncated up to a reasonable $G_{\rm max}$ value in healpix level 4 pixels. As this density factor may be attributed to the number of observations available, Fig. 7 presents with the same scale for comparison purposes the ratio of useful observations over the sky for photometry and astrometry.

For all type of binaries, the expected deficit of sources near the galactic center can be seen, due to both high density and poor coverage. The distribution for spectroscopic binaries ($G_{\rm RVS-max} = 12$, Fig. 6a) is also as expected with a smooth pattern of regions with higher numbers of Field of View transits. The non uniformity is less expected for eclipsing binaries ($G_{\rm max} = 18$, Fig. 6c) with a slight excess at the anticentre and an excess, larger than expected from the number of transits, around $l \pm 100°$ towards high ecliptic latitudes. For acceleration solutions ($G_{\rm max} = 15$, Fig. 6b) there is a deficit in the galactic plane and an excess at high ecliptic latitudes. This is worse for `Orbital` solutions ($G_{\rm max} = 15$, Fig. 6d), which may be due to the fact that orbital solutions require a number of observations larger than acceleration ones as the number of parameters to determine is larger. Again, the sky density factor is relative to the average over the sky, so that an excess in some regions may also, or rather, indicate a deficit in the rest of the sky. Part of the explanation of the above features of the astrometric solutions likely originates from the input source selection where sources suspected to be resolved doubles were excluded, which is more frequent in the galactic plane.

3.2. Astrometric orbit detection sensitivity as a function of orbital inclination

Gaia is observing sources with a cadence and scan angle ψ determined by its scanning law. Depending on whether a binary system is seen face-on (inclination $i = 0°$ or $i = 180°$) or edge-on ($i = 90°$), the detection probability of the astrometric orbit varies. An edge-on orbit that is oriented North-South and is being observed only with 1D astrometry along the East-West axis is undetectable. That extreme example does not occur for *Gaia*, but it illustrates that we can expect a continuous variation as a function of inclination angle, with edge-on orbits having lowest detection probability.

To obtain an empirical estimate of the expected dependency, we simulated 50000 circular orbits ($e = 0$, $\omega = 0$) with the following fixed parameters: distance 20 pc; period of 500 days; primary mass 1 $\mathcal{M}_\odot$; companion mass 1 $\mathcal{M}_{\rm Jup}$, and hence a semi-major axis of the host's orbit of $a_0 = 0.059$ mas. The ascending node Ω was uniformly distributed. We simulated inclinations such that $\cos i$ is uniformly distributed, as expected for isotropic orbit orientation in space.

To each orbit we assigned a realistic *Gaia* DR3 time sampling with associated scan angles, randomly retrieved from ~1 000 real sources distributed over the entire sky with the aim of averaging scan-law dependent effects. We then computed the RMS dispersion of the AL signal $w_{\rm k1}$ (Eq. (B.6)) caused by the astrometric orbit only, i.e. neglecting proper and parallactic motion. That dispersion shows a clear dependence on inclination angle, see Fig. 8, with the expected minimum for edge-on orbits. The vertical scatter is caused by the variation in the number of assigned *Gaia* observations and their scan-angle distribution for a particular time series realisation. The dependence on ascending node (Fig. 8, bottom) is much weaker but noticeable. Because we limited our simulation to circular orbits, there is no dependence on the argument of periastron.

In Appendix C we analytically derive the following expression (Eq. C.10) for the RMS of $w_{\rm k1}$ as a function of $\cos i$ which is valid for one-dimensional along-scan observations as used for DR3 (Lindegren et al. 2021) under the assumption of circular orbits and random scan angles:

$$\mathrm{RMS}(w_{\rm k1})(x) = \frac{a_0}{2}\,\sqrt{1+x^2} \quad \text{with} \quad x = \cos i. \tag{1}$$

This dependency is shown as 'Analytic model' in Fig. 8. A fit with a quadratic polynomial is also shown as 'Empirical model'. The analytic model reproduces the data very well, both in absolute amplitude and in shape, except for a small amplitude offset which probably reflects that the *Gaia* scan angles are not random and sometimes are restricted in range.

Because the amplitude of the orbit signal is the principal factor in deciding whether an orbit can be detected[5] there is no need to simulate the complete processing chain (Halbwachs et al. 2022; Holl et al. 2022b). Our simulations demonstrate that the signal of a face-on orbit is $\sqrt{2}$ larger than that of an edge-on orbit, which means that the former is more likely to be detected.

3.3. The Gaia catalogue of nearby stars

Together with *Gaia* EDR3 was published a clean catalogue of 331 312 sources within 100 pc of the Sun (Gaia Collaboration et al. 2021b, GCNS). This catalogue would represent a useful subset for the completeness analysis.

As the NSS parallaxes of `Orbital` or acceleration solutions may supersede the EDR3 ones, it is of interest to analyse first what would their impact be on the GCNS content. One finds 116 orbital sources that would now enter GCNS using the following query:

```
SELECT NSS.source_id, GS.phot_g_mean_mag, NSS.parallax,
NSS.parallax_error, GS.parallax as gs_parallax,
GS.parallax_error as gs_parallax_error
FROM user_dr3int6.nss_two_body_orbit NSS,
user_dr3int6.gaia_source GS
LEFT JOIN external.gaiaedr3_gcns_main_1 GCNS ON
NSS.source_id = GCNS.source_id
WHERE GCNS.source_id IS NULL
AND NSS.source_id = GS.source_id
AND NSS.parallax > 10
```

Using a similar query, 89 sources with an acceleration solution would enter GCNS, i.e. a total of 205 sources. These numbers would change by 13% only if we had taken a 1σ margin, so the random errors have a weak influence on this.

[5] This holds when neglecting complications with e.g. periods around one year due to crosstalk with parallax or scan-angle dependent effects (Holl et al. 2022a).

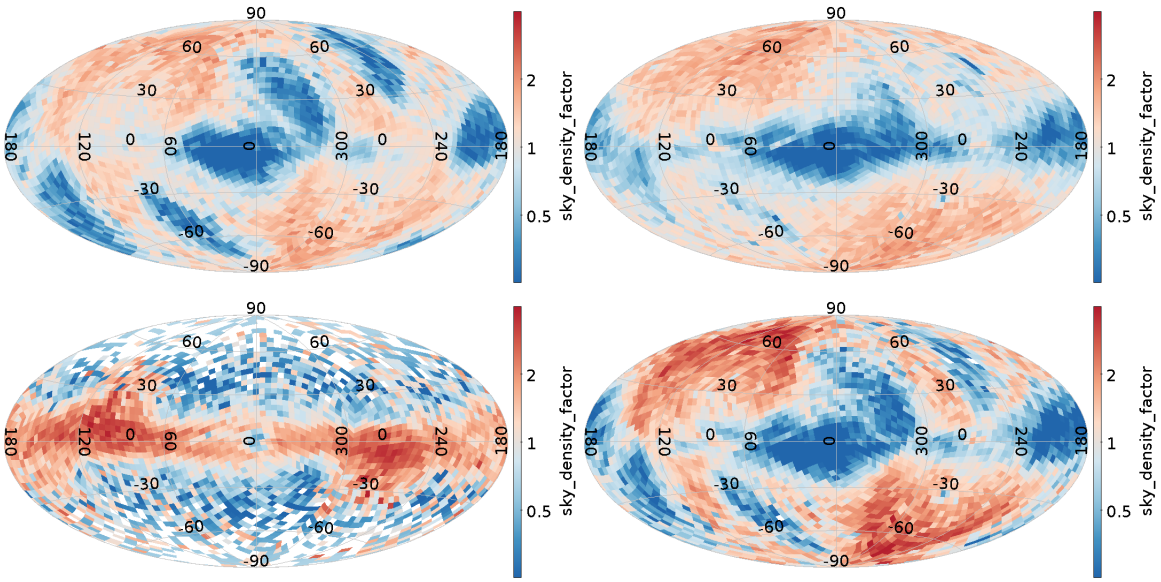

Fig. 6. Sky density factor (galactic coordinates, healpix level 4, log scale, see text) illustrating the excess or deficit factors of NSS sources compared to their sky average value. *Panel a*: `SB*`, *Panel b*: `Acceleration`, *Panel c*: `EclipsingBinary`, *Panel d*: `Orbital*`.

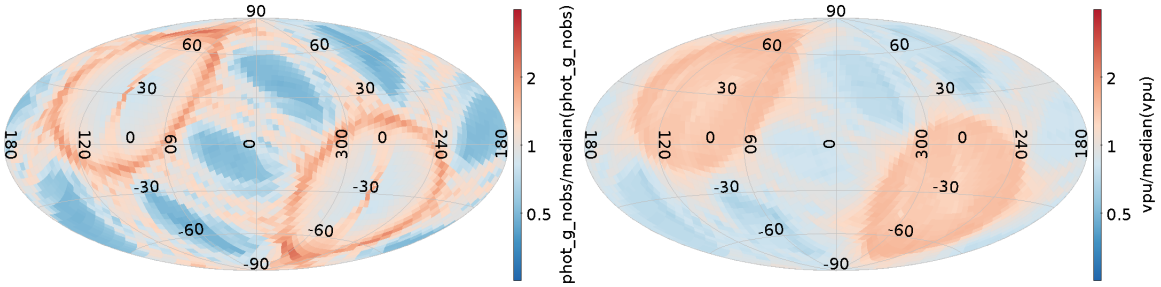

Fig. 7. Ratio of the number of photometric observations over their median values for $G < 18$ (*left*) and ratio of the number of visibility periods used in astrometry over their median values for $G < 15$ (*right*), same colour scale (from $\frac{1}{4}$ to 4) as Fig. 6.

Conversely, one may count sources which should no more belong to GCNS according to their new parallax:

```
SELECT NSS.source_id, GS.phot_g_mean_mag, NSS.parallax,
NSS.parallax_error, GS.parallax as gs_parallax,
GS.parallax_error as gs_parallax_error
FROM user_dr3int6.nss_two_body_orbit NSS,
user_dr3int6.gaia_source gs,
external.gaiaedr3_gcns_main_1 GCNS
WHERE NSS.source_id = GS.source_id AND
NSS.source_id = GCNS.source_id AND NSS.parallax < 10
```

amounting to 415 sources for orbital solution plus 413 sources for acceleration solutions, a total of 828 sources.

Although these numbers are not significant compared to the total size of the GCNS, they represent 9% of the orbital + acceleration solutions which may no more be in the GCNS (4723+4523 = 9246 astrometric NSS sources are in the GCNS) which is not negligible, while 2% may now enter. This means that any study of the NSS completeness within the GCNS should use the NSS parallax rather than the one from the main catalogue.

One may also note that the balance between the number of NSS that would be rejected from GCNS compared to the numbers that would enter illustrates one adverse effect of the random errors that is known for long (Eddington 1913; Trumpler & Weaver 1953). The parallaxes of NSS sources managed as single star in DR3 have a significant error, now much reduced in the NSS tables; this, added to the asymmetric distribution of the parallaxes made that binary sources preferentially entered GCNS that should not have belong to it. Noting also that the DR3 NSS catalogue contains only a small fraction of the actual unresolved astrometric binaries, then, if the GCNS is used to compute a binarity fraction, the above remark indicates that the GCNS has a small positive bias.

As a clarification of the GCNS content using the NSS parallax is outside the scope of this article, we keep the GCNS as reference in what follows. We show the fraction of NSS sources among $G < 19$ GCNS sources as a function of parallax, for all solution types, Fig. 9 right. In these figures and the following we add the `AstroSpectroSB1` counts both to orbital solution counts and SB counts, beside counting them independently and, for the comparison to be fair, we restricted the ratios to the typical magnitude ranges used respectively for astrometric, spectroscopic or eclipsing binaries.

What first appears is the conspicuous increase of the fraction of SB up to 100 pc. One reason for this may be the transition from the $G_{\rm RVS} < 12$ population of dwarfs to giants, as can be seen Fig. 4d, with the latter having a better intrinsic RV precision at a given apparent magnitude (Katz et al. 2022), and thus a larger binary detection probability; a difference in the binary fraction between dwarfs and giants cannot be excluded however. Second, contrarily to what could have been expected, the total of orbital and acceleration solutions, about 3%, appears roughly

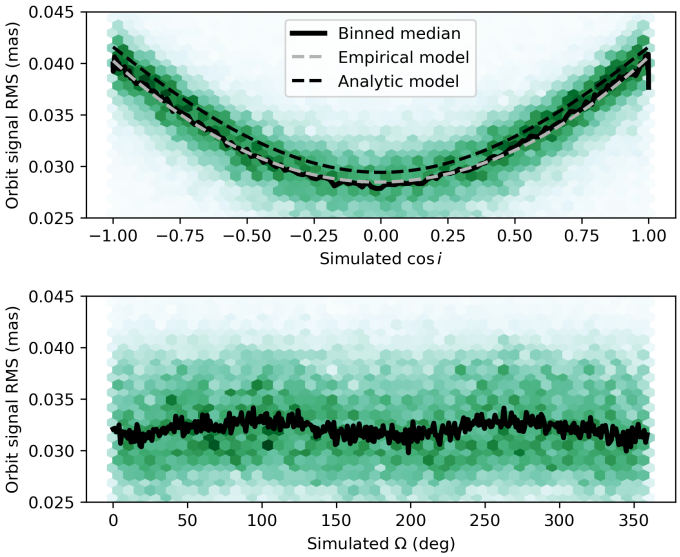

Fig. 8. Density histograms of simulated orbit signal dispersion as a function of $\cos i$ (*top*) and Ω (*bottom*). The black solid curve shows the running median value. In the top panel the empirical and analytic model is shown as dashed grey and black line, respectively. Edge-on orbits have $\cos i = 0$ and face-on configurations have $|\cos i| = 1$.

constant with distance in the GCNS, despite all the complex filtering that had been applied. For comparison, the fraction of NSS among DR3 sources, Fig. 9 left, shows logically the drop of astrometric solutions with distance beyond 100 pc while the spectroscopic binaries (SB+`nss_non_linear_spectro`) do not vary so sharply. We keep from this that even if the absolute value of the astrometric binary fraction is difficult to extrapolate after all the filtering done, the fact that it looks roughly uniform with distance in a first approximation in the GCNS sample could make this sample useful to study the properties of the astrometric binaries.

Consequently, the fraction of NSS among GCNS may give some useful insight, and Fig. 10 represents this ratio vs G apparent and absolute magnitude of the pair respectively[6].

4. Caveats

Many validations have been performed and described in the catalogue documentation (Pourbaix & et al. 2022), and accompanying papers, Halbwachs et al. (2022); Holl et al. (2022b); Gosset (2022); Siopis (2022), and the independent validation of all catalogues, Babusiaux et al. (2022). Elsewhere in this article we also check the distribution tails of some parameters which allowed us to discover undesired aspects and we indicate ways to circumvent them. We describe here two supplementary tests that draw attention to some properties of the catalogue, the first analysing the distribution of orbital parameters, the second comparing the results to binaries detected externally.

4.1. Distributions and biases of astrometric orbit parameters

Under the assumption that the orbits of binary systems are randomly oriented, we can infer the expected distributions in the geometric elements of the corresponding astrometric orbits, i.e. the inclination i, argument of periastron ω, and longitude of the ascending node Ω[7]. In an ideal experiment, we expect to recover uniform distributions in $\cos i$, Ω, and ω. Here we inspect the observed distributions of these parameters in DR3.

4.1.1. Observed distributions of geometric elements in DR3 solutions

Figure 11 shows the distributions of $\cos i$, Ω, and ω for the solution types `Orbital` and `AstroSpectroSB1`. To mitigate effects related to incomplete orbit coverage, we selected solutions with orbital periods shorter than 1 000 days, which roughly corresponds to the DR3 timespan.

For `Orbital` solutions there is a strong modulation in $\cos i$. Although the expected suppression of edge-on orbits is present, the observed distribution deviates significantly from the empirical model defined in Sect. 3.2. For progressively face-on configurations with increasing $|\cos i|$ there is an excess of solutions compared to the model. Beyond the modes $|\cos i| \gtrsim 0.85$ the number of detected almost-face-on orbits drops sharply and much below the expected level. We also observe a smooth modulation of the Ω distribution[8] with a single minimum at $\Omega = 90°$ and a bimodal modulation of the ω distribution with minima at $\omega = 90°$ and $270°$.

For `AstroSpectroSB1` solutions, resulting from the combined analysis of *Gaia* astrometry and RVs, the $\cos i$ distribution shows a good agreement with the empirical model for edge-on and intermediate configurations without region of excess detections. However, there is also a clear lack of face-on orbits compared to the empirical expectation. This is influenced by the decreasing orbital RV signature towards face-on orbits. Since `AstroSpectroSB1` solutions require independent detections in both astrometry and RV, the lack of face-on orbits can be expected. The modulation in Ω is similar to `Orbital` solutions but weaker[9] and there is no apparent modulation in the ω distribution.

In Fig. 12 we show the $\cos i$ distributions for systems within 200 pc, where the signal-to-noise is on average higher and the astrometric-orbit detection can be expected to be more complete. This is confirmed by the `Orbital` solutions that follow the empirical model nicely across most of the inclination range. This validates our model for the inclination-dependent detection efficiency of astrometric surveys (Sect. 3.2). The Ω and ω distributions for this subset of solutions are approximately uniform.

We have inspected but do not discuss other astrometric solution types here because those have fewer ($< 1\,000$) entries and are therefore less suitable for distribution analyses.

[6] The absolute magnitude `mg_gspphot` originates from the General Stellar Parametrizer from Photometry (GSP-Phot) which computed the astrophysical parameters of stars from the low-resolution BP/RP spectra and is available in the `astrophysical_parameters` table.

[7] These Campbell elements were computed from the Thiele-Innes coefficients (A, B, F, G), which are part of the archive table, using standard formulae (e.g. Halbwachs et al. 2022), software tools being available at `https://www.cosmos.esa.int/web/gaia/dr3-software-tools`

[8] The ascending node extracted from the Thiele-Innes coefficients of astrometric orbits is constrained to $\pm 180°$. By convention, the value between 0 and 180° is chosen.

[9] The Ω parameter is only constrained by the astrometry data. When deriving it from the `AstroSpectroSB1` Thiele-Innes coefficients we have neglected the additional RV information that would have allowed us to compute it unambiguously.

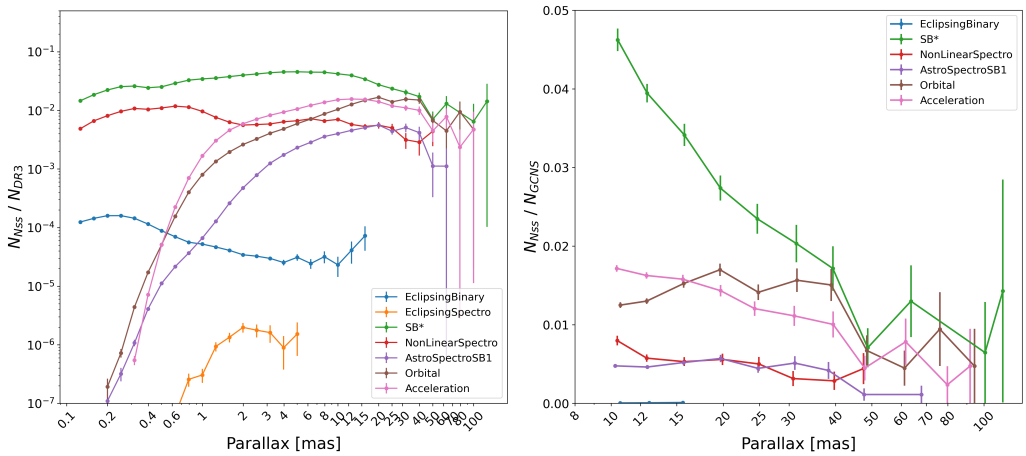

Fig. 9. Fraction of NSS solutions among EDR3 sources vs parallax (*left*) and fraction of NSS sources in GCNS (*right*). In both figures, we added `AstroSpectroSB1` counts to `Orbital` counts and to `SB*`=`SB1`+`SB2` counts beside counting them individually, and we restrict the ratios to $G_{\rm RVS} < 12$ sources only for `SB*` and `NonLinearSpectro`, to $G < 19$ for `Orbital` and `Acceleration` solutions and to $G < 20$ for eclipsing binaries.

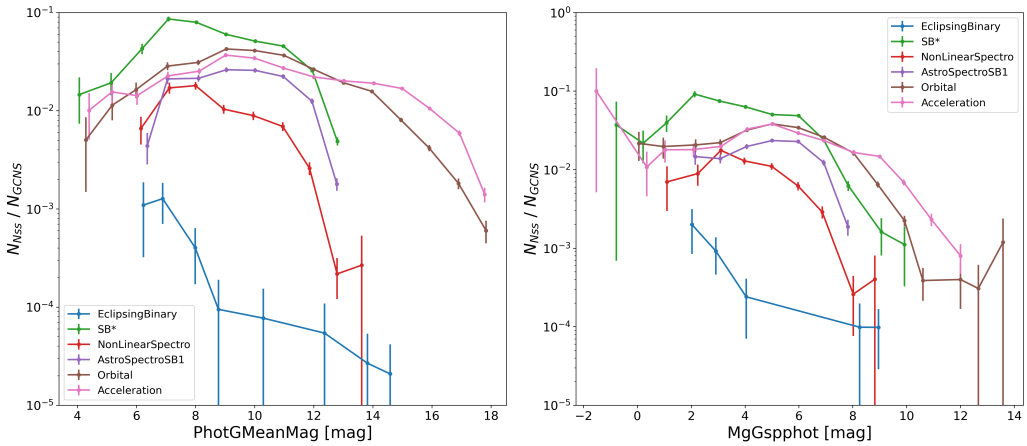

Fig. 10. Fraction of NSS solutions among GCNS sources vs G apparent magnitude (*left*) and vs G GSP-Phot absolute magnitude (*right*). The same constraints as mentioned in Fig. 9 have been applied.

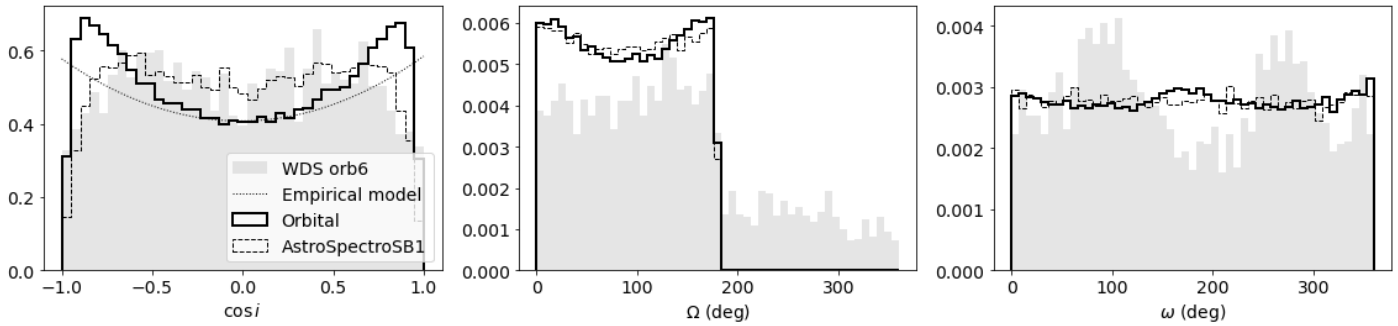

Fig. 11. Normalised distributions of $\cos i$ (*left*), Ω (*middle*), and ω (*right*) parameters. `Orbital` (solid lines, 122 989 entries) and `AstroSpectroSB1` (dashed lines, 29 770 entries) solutions with $P < 1\,000$ d are shown. The orb6 solutions from the literature (3 405 entries, without filter on period) are shown in grey. In the *left panel*, the dotted line shows the empirical model defined in Sect. 3.2, which was re-scaled on the 5 central histogram bins. In the right panel, we have suppressed the circular solutions with $\omega = 0$.

4.1.2. Origins of the geometric element biases

Concentrating on the `Orbital` solutions, we identify three main deviations from the expected uniform distributions in the low signal-to-noise regime, comprising most solutions and therefore dominating the overall distributions in Fig. 11: (a) a pronounced suppression of face-on orbits; (b) a smooth modulation of the Ω distribution with a single minimum; (c) a bimodal modulation of the ω distribution.

In Appendix D.1 we identify the origin of features (a) and (b) in the linear fit of the Thiele-Innes coefficients to noisy data and reproduce these biases qualitatively in simulations. The noise bias in the recovered inclination shifts solutions away from face-

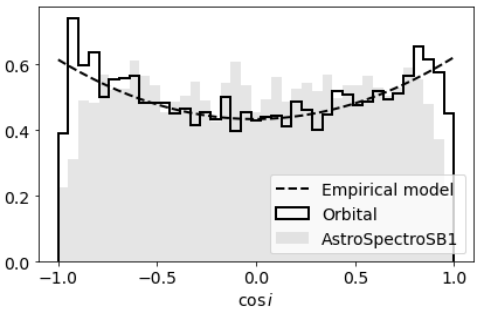

Fig. 12. Normalised distributions of $\cos i$ within 200 pc for `Orbital` (solid line, 9106 entries) and `AstroSpectroSB1` (grey-filled, 5735 entries) solutions with $P < 1\,000$ d and $\varpi > 5$ mas. The dashed line shows the empirical model defined in Sect. 3.2.

on configurations leading to the observed excess at intermediate inclinations[10]. A modulation akin to feature (c) can also be caused by noise biases, however, with a 90° phase shift. In Appendix D.2 we show that feature (c) is instead explained by the application of a semi-major axis significance threshold when selecting the solutions to be published.

4.1.3. Geometric elements from Monte-Carlo resampled Thiele-Innes coefficients

Instead of using the linearised formulae (e.g. Halbwachs et al. 2022) for converting A, B, F, G values and uncertainties to a_0, i, Ω, ω, one can use Monte-Carlo resampling which accounts more accurately for the parameter correlations (Appendix D.3). As an example of potential effects this may have, we computed an alternative estimate of the orbital inclination for individual solutions as the median of the resampled Monte-Carlo distribution. The difference between linearised and Monte-Carlo estimates on the inclination distribution is shown in Fig. 13, where we see that the apparent depletion of face-on orbits is more pronounced when applying the resampling. We note that the resampled distributions of a_0, i, Ω, ω are seldom Gaussian and the median value is not always a good representation. Whether it is advisable to use the linearised estimate or Monte-Carlo resampling depends on the particular problem and individual orbital solution.

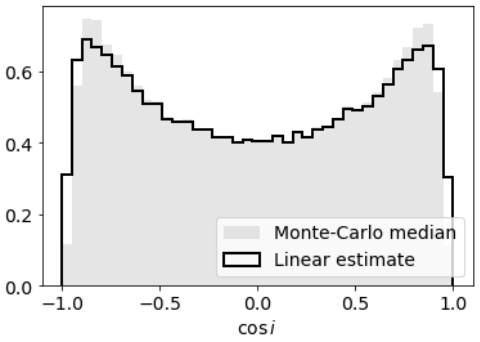

Fig. 13. Normalised distributions of $\cos i$ for non-circular `Orbital` solutions with $P < 1\,000$ d (121 207 entries). The linearised and Monte-Carlo estimates are shown as solid line and filled grey, respectively.

[10] Since the survey is not volume-limited, *Gaia*'s sensitivity variation in principle leads to an expected excess of face-on orbit detections. We believe that such effects are secondary in the context of DR3.

4.1.4. Comparison with known astrometric orbits

In Fig. 11 we also show the distributions of geometric elements compiled in the "Sixth Catalog of Orbits of Visual Binary Stars" (orb6, Hartkopf et al. 2001)[11]. The orb6 inclination distribution is bimodal with modes at $|\cos i| \simeq 0.5$, which could be interpreted as the same signature of lacking face-on orbits as for *Gaia* `Orbital` but setting in *earlier*. The comparison with the simulated inclination biases in Fig. D.1 then would lead to the interpretation that the average signal-to-noise is higher for the *Gaia* orbits than for the orb6 solutions. However, we caution that the orb6 dataset is of heterogeneous nature and such comparisons have to be done more carefully by accounting for differences in period range, significance, and other factors.
The orb6 Ω distribution does not seem to exhibit the minimum at $\Omega = 90°$ seen for *Gaia* `Orbital`. In contrast, the orb6 ω distribution shows clear modes at $\omega = 90°$ and 270°, i.e. shifted by 90° relative to *Gaia* `Orbital`. Our simulations in Fig. D.3 reproduce the peak location for orb6 orbits but not for `Orbital` solutions.

It is clear that the factor >40 increase in astrometric orbit solutions delivered by *Gaia* DR3 compared to orb6 will make a multitude of population-level studies possible and push forward in our understanding of stellar binary systems.

4.1.5. Recommendations

The observed features in the distributions of i, ω, and Ω are the result of variations in the survey's detection sensitivity, of selection effects, and of biases that are introduced in the astrometric non-single star processing. Their presence is not specific to *Gaia* and astrometric orbits in the literature show similar features. The geometric elements of DR3 orbits are encoded in the Thiele-Innes coefficients and different conversion methods can be applied, depending on the use-case and individual solution. Both the distribution features and the conversion aspects have to be considered in scientific analyses of *Gaia* DR3 orbital parameters and their distributions.

4.2. Proper motion anomaly of Hipparcos stars of the NSS sample

4.2.1. Comparison sample

In this Section we compare the properties of the Hipparcos stars based on the proper motion anomaly (hereafter PMa) approach (Kervella et al. 2022; see also Brandt 2021) and the NSS analysis. The PMa approach is described in details in Kervella et al. (2019a). The general principle is to look for a difference in proper motion (PM) between the long-term PM computed from the Hipparcos (epoch 1991.25; van Leeuwen 2007, see also ESA 1997) and *Gaia* DR3 (2016.0; Gaia Collaboration et al. 2021a) astrometric (α, δ) positions on the one hand and the individual short-term PM vector from the *Gaia* DR3 catalogue on the other hand. For a single star, the long-term PM is identical to the short-term PM measured by *Gaia*, as its space velocity is constant with time. For a binary star, the short-term PM includes in addition the tangential component of the orbital velocity of its photocentre. As the latter is changing with time over the orbital period of the system, a deviation appears between the short-term and long-term PMs of the star, due to the curvature of its sky trajectory. The proper motion anomaly (PMa), namely, the difference be-

[11] We retrieved `http://www.astro.gsu.edu/wds/orb6/orb6orbits.sql` on 2022-02-11 and did not remove orbits with two independent solutions or apply any other filters.

tween the short-term and long-term PM, is therefore an efficient and sensitive indicator to detect non-single stars.

In order to compare the NSS catalogue with the PMa approach, we cross-matched the NSS catalogue with the PMa catalogue[12] of Kervella et al. (2022), which covers 116 343 Hipparcos stars. This resulted in a list of 2 767 common targets with astrometric NSS `Acceleration7` or `Acceleration9` solutions and 5 416 stars with `Orbital`, `AstroSpectroSB1` or `OrbitalTargetedSearch*` orbital solutions. In addition, 4 385 Hipparcos targets are listed in the NSS tables with `EclipsingBinary` (photometric), `SB1` or `SB2` (radial velocity) solutions. Overall, 12 568 Hipparcos/PMa stars have an entry in the NSS catalogue, that is, 10.8% of the Hipparcos/PMa catalogue.

Table 2. Comparison of the PMa and NSS astrometric detection rate on the common Hipparcos star sample.

	Number	Fraction
Objects eligible to NSS & PMa	14 748	100.0 %
PMa S/N<3 and absent from NSS	2 254	15.3 %
PMa S/N>3 and absent from NSS	7 320	49.6 %
PMa S/N<3 and present in NSS	950	6.4 %
PMa S/N>3 and present in NSS	4 224	28.6 %
Total non-single stars (PMa or NSS)	12 494	100.0 %
Non-single stars detected from PMa	11 544	92.4 %
Non-single stars present in NSS	5 174	41.4 %

4.2.2. Completeness of the NSS sample for Hipparcos stars

The *Gaia* stars that are present in the NSS catalogue were selected based on criteria on parameters from their single-star solutions, tailored to identify the most probable binaries. For the astrometric solutions based on astrometry, this includes the presence of a `ruwe` higher than 1.4 in their single-star solution. As pointed out by Belokurov et al. (2020) and Stassun & Torres (2021), this criterion is efficient to identify the stars that host partially resolved companions. Furthermore, based on the PMa analysis, the binary fraction was found to remain high for `ruwe` values lower than 1.4 by Kervella et al. (2022) with, e.g., 30% of the stars with `ruwe` $\approx$ 1.2 exhibiting a PMa S/N > 3 (their Fig. 11). As a consequence, the degree of completeness of the star sample present in the NSS is likely relatively low, due to its selection threshold on the `ruwe` value. To estimate the completeness of the NSS for the Hipparcos stars, we first applied to the PMa catalogue the same selection criteria as the NSS input sources (Sect 2.2.1), except the condition `ruwe` > 1.4, resulting in a subsample of 92 240 stars (79.3%). Within this subsample, 28 111 stars are high probability astrometric binaries as their PMa S/N > 3. Restricting the count to the NSS stars that have an astrometric solution (`Acceleration7`, `Acceleration9`, `Orbital`, `AstroSpectroSB1` or `OrbitalTargetedSearch*`), we therefore obtain a completeness level of the NSS catalogue relative to the PMa catalogue of 8 183/28 111 = 29.1%.

However, this high-level estimate based on global target numbers does not directly reflect the actual efficiency of the NSS reduction to detect that a star is a binary or not, compared to the PMa technique. To estimate this efficiency, we consider the same initial sample, following the NSS selection criteria including `ruwe` > 1.4, and we derive the fraction of stars with an NSS solution within this common sample. The results are listed in Table 2. Overall, the astrometric solutions provided in the NSS catalogue represent 41% of the potential binaries present in the NSS reference sample, compared to 92% for the PMa catalogue.

In summary, due to the stringent selection of the solutions for the NSS, the catalogue comprises approximately 40% of the binaries from the Hipparcos-*Gaia* PMa catalogue that were potentially detectable from *Gaia* astrometry alone.

4.2.3. Statistics of proper motion anomaly of NSS targets

The PMa is an efficient tracer of the presence of a massive orbiting companion, but its sensitivity is limited by two aspects. Firstly, the time baseline between Hipparcos and *Gaia* (24.75 years), although long, significantly reduces the PMa signature of companions with orbital periods longer than approximately three times the Hipparcos-*Gaia* time, that is, 75 years. Secondly, the fact that the *Gaia* DR3 proper motions are the result of an averaging over a time window of 34 months strongly smears out the signature of companions with orbital periods shorter than approximately 4 years. In summary, the PMa technique is most sensitive for companions with orbital periods between $\approx$ 4 and 75 years. On the other hand, the capacity to determine orbital solutions directly from *Gaia* astrometry (or radial velocity) time series is significantly higher for binaries with periods shorter than the *Gaia* DR3 measurement window. The longer periods remain detectable, mostly up to about twice the measurement window. However, the astrometric displacement of long-period binaries is generally detected only as an acceleration, hence without a period determination.

Figure 14 shows the histograms of the number of NSS stars with different kinds of solutions, as a function of their PMa signal-to-noise ratio. The five histograms that are colour-coded in blue correspond to NSS solutions that include the *Gaia* DR3 astrometry either exclusively (`Acceleration7`, `Acceleration9`, `Orbital`) or in conjunction with spectroscopic radial velocities (`AstroSpectroSB1`) or previously known substellar orbital parameters (`OrbitalTargetedSearch*`). The eclipsing binary stars (`EclipsingBinary`; green colour) are characterized from the *Gaia* photometric data, and the spectroscopic binaries (`SB1`, `SB2`; yellow colour) rely on the spectroscopic radial velocities measured by the *Gaia* RVS (Cropper et al. 2018; Katz et al. 2019).

4.2.4. Orbital periods and sensitivity

Almost all the Hipparcos targets with an `Acceleration7` or `Acceleration9` solution show a significant PMa signal. This behavior is expected for two reasons: (1) The NSS astrometric solutions have been selected among the *Gaia* sources with a `ruwe` larger than 1.4. This favors partially resolved binary stars, that often have orbital periods within the sensitivity range of the PMa technique. (2) For longer orbital periods than the *Gaia* measurement window, the PMa and the acceleration are physically similar quantities, both related to the curvature of the sky trajectory of the star.

The NSS catalogue stars with `Orbital` or `AstroSpectroSB1` solutions generally have shorter orbital periods than the *Gaia* DR3 time window. Due to the time smearing of the *Gaia* EDR3 proper motions, this usually prevents the production of a clear signature in PMa. Nevertheless, approximately two thirds of the stars of these NSS classes exhibit a significant PMa signal with S/N > 3 (Fig. 14). As shown in Fig. 15, the longer *Gaia* EDR3 time window compared to the DR2 results in a decrease of the PMa S/N for the binaries whose orbital period

[12] Available through the CDS/VizieR service as catalogue `J/A+A/657/A7/tablea1`

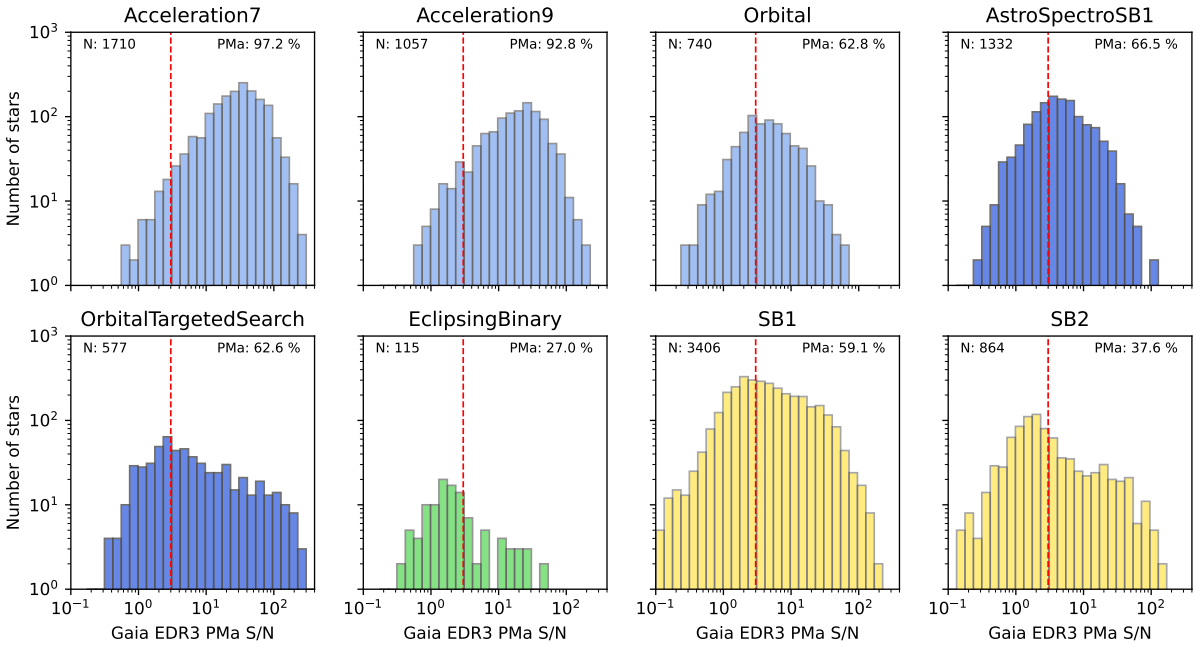

Fig. 14. Histogram of the number of NSS stars with different solution types that are present in the Hipparcos catalogue, as a function of the S/N of their *Gaia* DR3 proper motion anomaly from Kervella et al. (2022). The total number of targets N and the fraction of stars with a PMa S/N larger than 3 is displayed in each panel.

is shorter than $\approx$ 1 000 days. This is caused by the stronger time smearing of the astrometric signal by the integration window in the *Gaia* DR3 compared to that of the DR2, that is not compensated by the increase in measurement accuracy in the *Gaia* DR3. The systems with shorter orbital periods than the *Gaia* integration window exhibit a median PMa S/N $\approx$ 3. This indicates that despite the smearing, statistically the mean *Gaia* PM vector still contains a significant signature of the binarity. The vast majority of *Gaia* NSS targets with orbital periods longer than the *Gaia* time window (both for the DR2 and EDR3) exhibit a significant PMa S/N > 3.

4.2.5. Long-term Hipparcos-*Gaia* proper motion

We here compare the long-term proper motion deduced from the difference in position between the Hipparcos (1991.25) and *Gaia* DR3 (2016.0) epochs by Kervella et al. (2022) (hereafter $\mu_{\rm HG}$) with the short-term proper motion as determined in the NSS catalogue ($\mu_{\rm NSS}$). Figure 16 shows the observed differences $\Delta\mu = \mu_{\rm NSS} - \mu_{\rm HG}$ between these two quantities for the Hipparcos catalogue stars with either accelerations (`Acceleration7`, `Acceleration9`) or orbital (`Orbital`, `AstroSpectroSB1`) solutions in the NSS. There is a significantly larger divergence of the long-term proper motions between the stars with NSS accelerations only for which $\sigma(\Delta\mu) \approx 2.6$ mas a^{-1}, than for the stars with an orbital solution for which $\sigma(\Delta\mu) \approx 0.1$ mas a^{-1}. The relatively poor agreement for the NSS acceleration stars may be explained by the fact that the measurement of the curvature of the sky trajectory is significantly easier with the longer Hipparcos-*Gaia* temporal baseline. For the full NSS orbital solutions, the agreement between the Hipparcos-*Gaia* PM and the NSS PM is remarkably good, demonstrating that the orbital fit procedure does not introduce systematic biases on the estimation of the mean PM value.

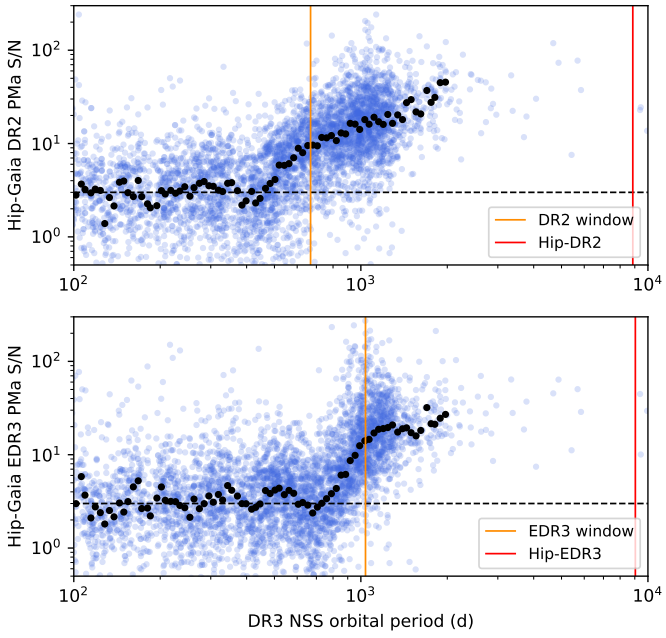

Fig. 15. Proper motion anomaly S/N as a function of the NSS catalogue orbital period for the DR2 PMa (*top panel*); from Kervella et al. (2019a)) and the EDR3 PMa (*bottom panel*); from Kervella et al. (2022)). The horizontal dashed line indicates the PMa S/N=3 significance limit.

5. Catalogue of masses

As the `nss_two_body_orbit` table gives access to the orbital parameters only, it was found desirable to provide an estimate of the masses, of the flux ratio, or to lower and upper limits of these, when this was possible. We describe in this Section the construction and content of the table `binary_masses` which has been made available in the *Gaia* Archive.

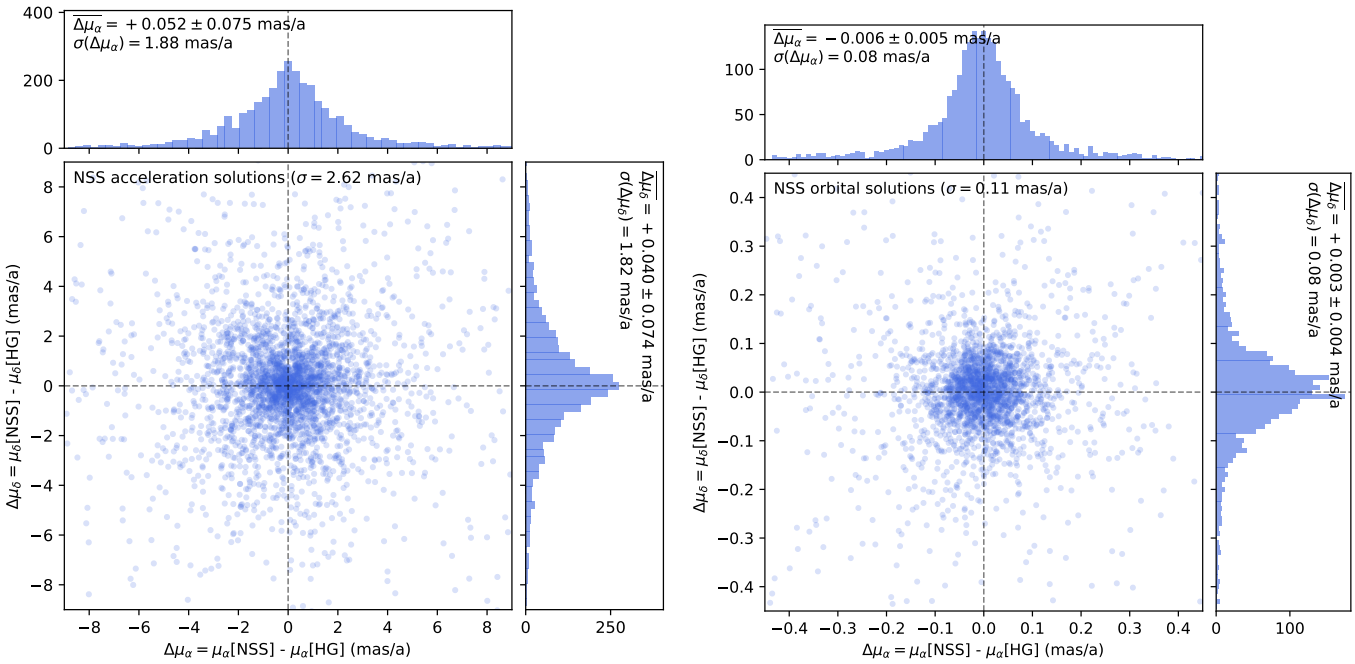

Fig. 16. Comparison of the long-term proper motions determined from the Hipparcos and *Gaia* DR3 positions $\mu_{\rm HG}$ with the *Gaia* DR3 proper motions $\mu_{\rm NSS}$ for NSS stars with acceleration solutions (*left panel*) and orbital solutions (*right panel*). Note the different scales.

5.1. Computation of the masses

The astrometric binaries give access to an astrometric mass function which depends on the flux ratio (F_2/F_1) of the components:

$$(\mathcal{M}_1 + \mathcal{M}_2)\left(\frac{\mathcal{M}_2}{\mathcal{M}_1 + \mathcal{M}_2} - \frac{F_2/F_1}{1 + F_2/F_1}\right)^3 = \frac{(a_0/\varpi)^3}{(P/365.25)^2} \quad . \tag{2}$$

While the spectroscopic binaries provide a spectroscopic mass function which also depends on the inclination:

$$f(\mathcal{M}) = \frac{\mathcal{M}_2^3 \sin^3 i}{(\mathcal{M}_1 + \mathcal{M}_2)^2} = 1.0385 \times 10^{-7} K_1^3 (1 - e^2)^{3/2} P \ , \tag{3}$$

with P the period in days and K_1 the semi-amplitude of the primary in km s^{-1}. For `AstroSpectroSB1`, we have access to the Thiele Innes coefficients instead of K_1 which leads to the equivalent formula:

$$\frac{\mathcal{M}_2^3 \sin^3 i}{(\mathcal{M}_1 + \mathcal{M}_2)^2} = \frac{(C^2 + H^2)^{3/2}}{(P/365.25)^2}. \tag{4}$$

The inclination can be provided by an astrometric solution or an eclipsing one. Without the inclination, Eq. 3 only leads to a minimum mass function information. When a `SB2` solution is provided, we have access to the mass ratio $\mathcal{M}_2/\mathcal{M}_1 = K_1/K_2$. When a system has a `SB2` solution and either an astrometric solution or an eclipsing one, the primary mass can be derived directly from the binary orbital parameters.

Two estimates of $\mathcal{M}_1$ are provided in the *Gaia* DR3 by the `FLAME` module (Creevey et al. 2022): `mass_flame`, based on GSP-Phot parameters and available in the `astrophysical_parameters` table and `mass_flame_spec`, based on GSP-Spec parameters and available in the `astrophysical_parameters_supp` table. However the `FLAME` masses have three main limitations for our NSS sample: they are based on the parallax from the main catalogue while we now have a more accurate estimate for all astrometric solutions; they also assume a null flux ratio, which we know is not adapted for a significant fraction of the NSS solutions, in particular the SB2 ones; they are not available for stars with masses smaller than 0.5 $\mathcal{M}_\odot$. We therefore implemented a specific code to derive the mass of the primary that allows to play with the luminosity ratio and is described in detail in Appendix E. These masses are only derived for stars on the main-sequence as estimations for evolved stars are degenerate (e.g. Creevey et al. 2022). They are called hereafter 'IsocLum'. For white dwarfs, we simply assumed a fixed mass of 0.65±0.16 $\mathcal{M}_\odot$ (Giammichele et al. 2012).

The uncertainties on the masses and flux ratios obtained are derived using a Monte Carlo simulation of 1 000 points. We take into account the covariance matrix of the orbital parameters. For a_0 as well as for the `AstroSpectroSB1` spectroscopic part $a_1 = \sqrt{C^2 + H^2}/\sin i$, we use a Gaussian distribution with a local linearisation error estimation as Monte Carlo techniques are not adapted to the Thiele Innes coefficients (see Babusiaux et al. 2022). Only sources with a `significance` > 5 are present in NSS solutions so that a Gaussian distribution of the semi-major axis errors is a reasonable assumption. The uncertainties for the SB2 and eclipsing solutions have been re-scaled according to their goodness-of-fit. For the IsocLum masses we use the full mass distribution function as we have it available. We then compute the 16th and 84th quantiles (corresponding to $\pm 1\sigma$) of the derived parameter distributions to estimate the lower/upper values respectively. The direct values are provided whenever applicable for `m1`, `m2`, `fluxratio`.

When combining two NSS solutions, we only use those with periods and eccentricities compatible within 5σ, assuming an uncertainty of 0.1 on the eccentricity for sources with a fixed eccentricity. A weighted mean of the periods and eccentricities of both solutions is then used in Eqs. 2 and 3. For the combination of astrometric and spectroscopic solutions, the primary mass is tested for different flux ratios by steps of 0.01, then for each of

these, the secondary mass is derived from Eq. 3 and the flux ratio from Eq. 2; only solutions which are consistent with the tested flux ratio are kept and when no solution is consistent, the closest one is used.

For `Orbital` solutions, only upper and lower values can be derived as the flux ratio is not known. Different flux ratios are tested by steps of 0.01. The lower (resp. upper) secondary mass value is computed from the mass distribution obtained with the lower flux ratio (resp. upper). The solution with `fluxratio` = 0 is always kept, as soon as the primary star magnitude is compatible with the isochrones. For the other flux ratios tested, the secondary mass derived is accepted if consistent with a secondary star on the main sequence. In practice, the Monte Carlo masses of the secondary lead to a range of possible absolute magnitudes from the isochrones, which, for the flux ratio tested, are converted into an absolute magnitude of the system which is accepted when it is at less than 3 sigma from the absolute magnitude of the system measured by Gaia. In some cases, this leaves no flux ratio kept. These can be either pre-main sequence stars, in which case our masses are invalid, or triple systems with a primary which needs a flux ratio but a secondary mass not consistent with it. To handle this second option, the minimum flux ratio compatible with a primary on the main sequence is used to derive the primary mass but the secondary mass is derived with $F_2/F_1 = 0$. These cases can be isolated with a '`fluxratio_upper is NULL`' query. No limit is tested on the maximum flux ratio for white dwarfs. For SB1 solutions, the lowest valid flux ratio is used to derive the primary mass and the lower secondary mass value is derived on the distribution assuming $\sin i = 1$. For eclipsing binaries, the flux ratio is fixed by `g_luminosity_ratio`.

The catalogue of masses we derive is available in the *Gaia* Archive table `binary_masses`. A summary of its content is presented in Table 3. We selected only sources with a signal-to-noise ratio higher than 5 on the astrometric semi-major axis and on the spectroscopic primary semi-amplitude as well as a signal-to-noise ratio higher than 2 for the eclipsing binary and astrometric $\sin i$ and the spectroscopic secondary semi-amplitude. For `AstroSpectroSB1` solutions, both the signal-to-noise for the spectroscopic part, computed as the one of $\sqrt{C^2 + H^2}$, and of a_1 are checked to be higher than 5. If not, the `AstroSpectroSB1` is treated as an `Orbital` solution only. `OrbitalAlternative` solutions with $\log_{10}(\texttt{parallax/parallax\_error}) < 3.7 - 1.1\log_{10}(\texttt{period})$ have been excluded. 76 sources are duplicated, having both an astrometric solution and either an eclipsing binary (6) or a `SB2` solution (70) one, with the astrometric solution period being larger than the other one by more than 10 sigma. For sources with both an `SB1` and an `Orbital` solution, only the `Orbital` solution has been kept.

A particularly interesting subset of this table are the astrometric solutions with `fluxratio_upper` = 0. There is only one star (*Gaia* DR3 4288765058313593856) for which the secondary mass is sufficiently small ($0.57\,\mathcal{M}_\odot$) compared to the primary ($1.26\,\mathcal{M}_\odot$) so that `fluxratio_upper` = 0 is compatible with the secondary star being on the main sequence. The others are systems for which the secondary mass solutions for flux ratio > 0 did not have the mass compatible with any of the flux ratio tested. The secondary mass distribution of these is presented in Fig. 17. There are 12 stars with a secondary mass smaller than the minimum mass handled by the isochrones of $0.1\,\mathcal{M}_\odot$ and a low mass for the primary too. Three other stars with low mass secondaries could be either triple or pre-main-sequence stars for which the primary mass is not correct. The most predominant peak is the one of the white dwarfs at $\mathcal{M}_2 = 0.61\,\mathcal{M}_\odot$ which has a standard deviation of $0.07\,\mathcal{M}_\odot$. Note that some white dwarf companions should actually have a flux ratio > 0, such as *Gaia* DR3 6416572288572864512 which is an `AstroSpectroSB1` with a significant flux ratio; the primary mass has been estimated as the one of a metal-poor star due to its location on the left of the main sequence; if it had been solved as an astrometric solution only it would have had `fluxratio_upper` = 0 and a secondary mass under-estimated. A long tail of high mass secondaries is also present. They can be compact objects but also triple stars for which the single primary star hypothesis was not valid (See Sect. 7.1) or primary stars who started to evolve or metal-poor giants for which the primary mass is not correct.

Table 3. Content of the Catalogue of masses.

Combination Method	Number	$\mathcal{M}_1$	$\mathcal{M}_2$	F_2/F_1
Orbital+SB2	23	✓	✓	✓
EclipsingSpectro(SB2)	3	✓	✓	
Eclipsing+SB2	53	✓	✓	
AstroSpectroSB1+M1	17578		✓	✓
Orbital+SB1+M1	1513		✓	✓
EclipsingSpectro+M1	71		✓	
Eclipsing+SB1+M1	155		✓	
SB2+M1	3856		✓	
Orbital+M1	111792		lower/upper	
SB1+M1	60271		lower	

Notes. The full table is available in the *Gaia* table `binary_masses`.

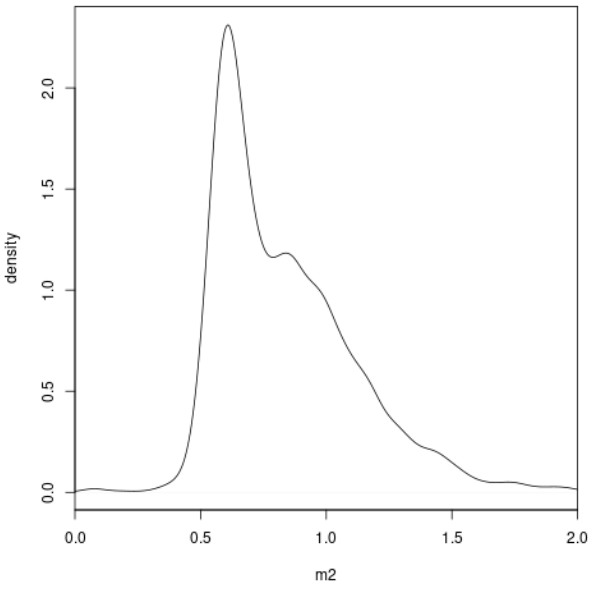

Fig. 17. Distribution of the secondary mass of astrometric solutions with `fluxratio_upper` = 0 in Table 3.

5.2. Masses using external data

In this section we illustrate how other mass estimates can be obtained thanks to various kinds of combinations with external data.

5.2.1. External SB2

Combining astrometric orbits with spectroscopic ones from large surveys is not recent, and it was e.g. done with Hipparcos (Arenou et al. 2000). Once the inclination known from the astrometric orbit, the semi-amplitudes from the spectroscopic orbit allows to determine simultaneously the masses and luminosities of the two components. Recently, APOGEE DR17 data has been used to detect 8 105 SB2 or higher order systems (Kounkel et al. 2021). Once the needed number of epochs will be available, individual masses and magnitude differences will be obtained for the sources having an NSS `Orbital*` solution. Here, we just take the example of *Gaia* DR3 702393458327135360, with $K_1 = 19.53 \pm 0.95$ km s^{-1} and $K_2 = 21 \pm 1.1$ km s^{-1}. The masses are found to be $\mathcal{M}_1 = 1.14 \pm 0.38\,\mathcal{M}_\odot$ and $\mathcal{M}_2 = 1.06 \pm 0.35\,\mathcal{M}_\odot$ with a 0.567 ± 0.071 flux ratio.

5.2.2. Occultations

Occultations represent a neglected way to constrain the sum of masses of binaries, thanks to the measurement of their separation at a given epoch.

We illustrate this with *Gaia* DR3 3162827836766605440 (HIP 36189) which is a $V \approx 6.5^m$ K giant that has been discovered as double thanks to an occultation by (704) Interamnia on 23 March 2003. Its acceleration had been detected in Kervella et al. (2019a), Brandt (2021), and Kervella et al. (2022). Satō et al. (2014) indicate a $\rho = 12 \pm 3$ mas separation while a more precise indication is given by Herald et al. (2020), $\rho = 13.0 \pm 0.7$ mas with position angle $\theta = 231.9 \pm 4.0°$. Satō et al. (2014) evaluate the magnitude difference between components to about 1.5, to which we attribute a 0.2 mag uncertainty, accounting in particular for the observation in a band different from the G band.

This source has received an `Orbital` solution with a 2.6 yr period. From the combined information, the masses of the components are found to be $\mathcal{M}_1 = 3.9 \pm 2.2\,\mathcal{M}_\odot$ and $\mathcal{M}_2 = 3.5 \pm 1.6\,\mathcal{M}_\odot$.

5.2.3. One SB1 Cepheid

Although it is known that many Cepheids are in binary systems (e.g. Kervella et al. 2019b), not many orbits are present in the non-single star Catalogue. On the spectroscopic orbit side, the *Gaia* DR3 data processing did not include yet the simultaneous handling of orbit and Cepheid pulsations, so that is the latter only that were detected. Consequently, these solutions were filtered out from the catalogue to avoid any confusion. On the astrometric orbit side, only one deserves attention which received an `Orbital` solution.

Gaia DR3 4703611143398494 72 = RX Cam is known to be a G2Ib+A0V spectroscopic binary from Imbert (1996). The *Gaia* solution has a period 999 ± 104 d and an eccentricity 0.514 ± 0.049, consistent at 1σ with respectively 1113.8 ± 0.5 d and 0.459 ± 0.007 from Groenewegen (2013). The inclination is $i = 113\overset{\circ}{.}5 \pm 1\overset{\circ}{.}7$. We may safely assume that there is no flux contribution (in the G band) from the companion, as confirmed by the difference between the semi-major axis of the primary and that of the photocentre $a_1 - a_0 = 0.04 \pm 0.12$ au. Using the semi-amplitude $K_1 = 14.27 \pm 0.11$ km s^{-1} from Groenewegen (2013) and the estimation of the primary mass from Kervella et al. (2019b), $\mathcal{M}_1 = 5.40 \pm 0.81\,\mathcal{M}_\odot$, we obtain $\mathcal{M}_2 = 2.87 \pm 0.34\,\mathcal{M}_\odot$.

6. Special binaries in the HRD

In this section, we select several illustrative cases where the NSS catalogue can provide a useful insight into populations of the Hertzsprung-Russell diagram (HRD). For further reference we present in Fig. 18 the period-eccentricity diagram for the NSS solutions with orbits.

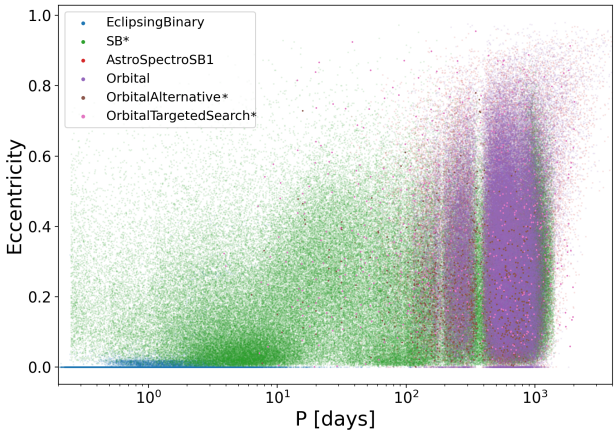

Fig. 18. Eccentricity vs period for most solutions with orbits.

6.1. Spectroscopic binaries along the main sequence

This section presents and briefly comments the eccentricity-period (hereafter e - P) diagrams of SB1s along the main sequence, defined as $-7.5 + 10\,(G_{\mathrm{BP},0} - G_{\mathrm{RP},0}) < M_{G,0}$ (Fig. 19), with the photometry being de-reddened in the same way as for the mass derivation (see Appendix E). Stars along the main sequence are divided according to $(G_{\mathrm{BP},0} - G_{\mathrm{RP},0})$ bins, as indicated in Fig. 19.

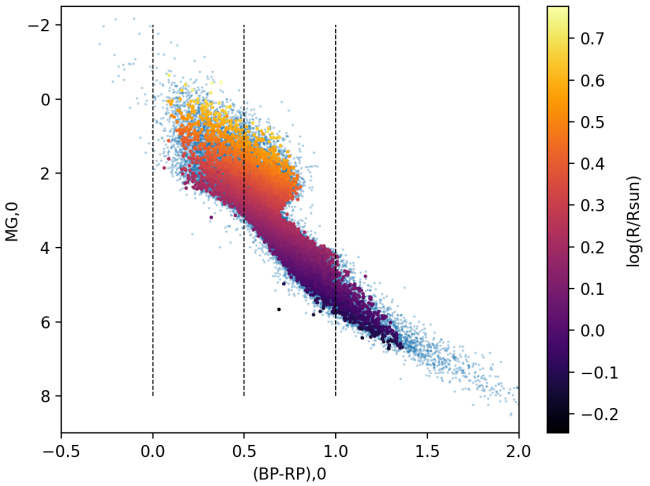

Fig. 19. Location in the dereddened HRD of the $(G_{BP,0} - G_{RP,0})$ bins used in Fig. 20. Small blue dots correspond to the SB1 not selected by our selection criteria. The radius is the `FLAME` estimate.

The e - P diagrams along the main sequence are displayed in Fig. 20. Because of the aliasing problems faced by the SB1

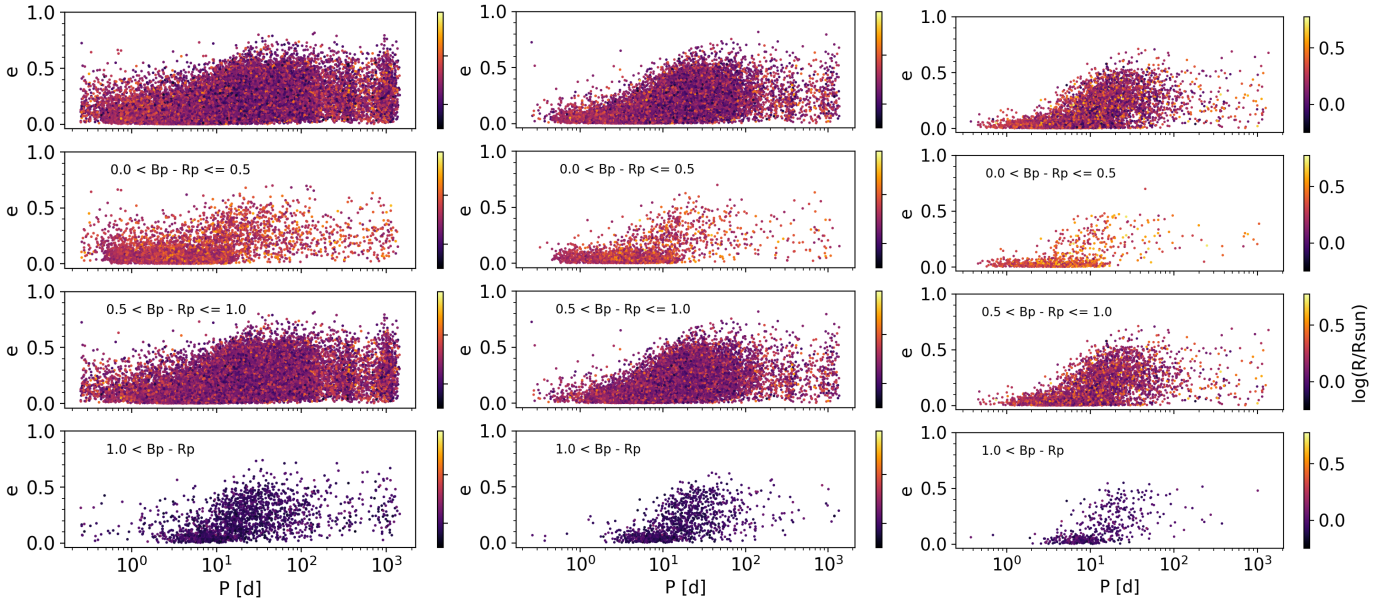

Fig. 20. The e - P diagram for SB1s along the main sequence, filtered according to significance factors larger than 10, 20 or 40 (from *left* to *right*), and for different ($G_{\rm BP,0} - G_{\rm RP,0}$) spans (*top* to *bottom*). Note how the long-period tail gets more populated when the significance is allowed to be smaller (*left panels*), since long-period orbits have smaller K_1 on average, and hence smaller significances K_1/σ_{K_1}. But at the same time the populated region becomes almost rectangular (*top left panel*), which appears quite unusual. There is a drop in the number of systems at $P = 0.5$ y due to insufficient sampling at this specific period. The color codes for the `FLAME` radius estimate.

processing (see Sect. 2.3), these diagrams are shown for different filtering based on the significance of the RV semi-amplitude, namely K_1/σ_{K_1} larger than 10, 20 or 40 (from left to right). This filtering removes both high-eccentricity short-period orbits and long-period orbits. The former filtering is on purpose to remove possibly spurious solutions, while the disappearance of the long-period solutions is a side effect due to the fact that long periods have on average smaller K_1 and thus smaller significances as well. Nevertheless, this filtering has the consequence of revealing the shape expected for any e - P diagram, namely short-period orbits being almost exclusively circular below a given 'transition' period (see e.g., Mazeh 2008, for a detailed discussion).

The e - P diagrams along the main sequence, when ordered according to bins of increasing $G_{\rm BP,0} - G_{\rm RP,0}$ and properly filtered on a significance larger than 40 (right panels of Fig. 20), reveal that this transition period does not vary strongly between the various $G_{\rm BP,0} - G_{\rm RP,0}$ bins, contrarily to the situation prevailing along the giant branch, as discussed below (Sect. 6.2). Mazeh (2008) has reviewed the processes shaping e - P diagrams, with the conclusion that the constancy of the transition period along the main sequence would naturally result if the circularisation occurred during the pre-main-sequence phase, when the stars were large, following a suggestion by Zahn & Bouchet (1989) for F, G and K stars from 0.25 to 1.25 $\mathcal{M}_\odot$. Their transition period does stay constant along the main sequence at about 8 d. The transition period observed on Fig. 20 seems a bit shorter though. x Mazeh (2008) also argues that short-period binaries (i.e., below the transition period) with non-circular orbits could result from a third distant companion pumping eccentricity into the binary orbit. However, at the time being, due to the confusion caused by possible period aliasing among short-period SB1 systems, this possibility cannot be tested with confidence.

6.2. Binaries along the RGB/AGB

The goal of this section is to show that the transition period between circular and non-circular orbits is increasing with radius and luminosity along the red giant branch (RGB) and asymptotic giant branch (AGB). To select stars on these branches, it is more efficient to use the 2MASS colour - magnitude diagram ($J - K$, $M_{\rm K}$) rather than the usual Gaia colour - magnitude diagram. We used the 2MASS cross-match with EDR3 available within the data archive[13] and used the following criteria to select giants:

$$J - K > 0 \text{ and } M_K < 0, \tag{5}$$

as illustrated below.

6.2.1. Period - radius diagram

The existence of a circularisation threshold period in the e - P diagram was demonstrated by Pourbaix et al. (2004) in their Fig. 4 (see also Zahn & Bouchet 1989; Verbunt & Phinney 1995; Mazeh 2008; Jorissen et al. 2009; Escorza et al. 2019). Its analytic form in a period - radius diagram may be easily obtained from the simple expression of the Roche radius R_R around the star of mass $\mathcal{M}_1$ with a companion of mass $\mathcal{M}_2$ (Paczyński 1971):

$$R_{R,1} = a \left(0.38 + 0.2 \log \frac{\mathcal{M}_1}{\mathcal{M}_2}\right). \tag{6}$$

Substituting Kepler's third law, and assuming that the period threshold (expressed in days) corresponds to the situation where

[13] `https://gea.esac.esa.int/archive/documentation/GEDR3/Gaia_archive/chap_datamodel/sec_dm_crossmatches/ssec_dm_tmass_psc_xsc_best_neighbour.html`

the star radius is equal to the Roche radius, one finds after some algebra:

$$\begin{aligned}\log(P_d^{\rm thresh}/365.25) &= (3/2)\ \log(R_1\ /\ 216\ {\rm R}_\odot) \\ &\quad -(1/2)\ \log(\mathcal{M}_1+\mathcal{M}_2) \\ &\quad -(3/2)\ \log\left(0.38+0.2\ \log\frac{\mathcal{M}_1}{\mathcal{M}_2}\right) \quad (7)\\ &\equiv (3/2)\ \log(R_1\ /\ 216\ {\rm R}_\odot) \quad (8)\\ &\quad -(3/2)\ c_1,\end{aligned}$$

where c_1 only depends on the masses. These thresholds are represented on Fig. 21 as dashed lines (corresponding to different choices for the pair $\mathcal{M}_1, \mathcal{M}_2$). That figure presents all SB1 solutions falling along the RGB/AGB as defined above based on the $(J-K,\ M_{\rm K})$ colour - magnitude diagram. Figure 21 reveals however that there are many SB1 solutions involving giant stars that do not fulfill the condition $P \geq P^{\rm thresh}$ expressed by Eqs. 7 and 8, especially when the significance K_1/σ_{K_1} is smaller than 40.

6.2.2. e - P, P - $f(\mathcal{M})$ diagrams

Figure 22 presents the e - P diagram for the same set of SB1 solutions (left panel) as shown on Fig. 21a, as compared to astrometric binaries along the RGB/AGB (right panel). The difference between the period range covered by `SB1` and astrometric solutions is striking. Since most astrometric orbits have periods longer than about 200 d, they clearly satisfy the criterion expressed by the dashed line on Fig. 21 and do not overfill their Roche lobe, contrarily to the short-period `SB1` solutions.

Figure 23a is similar to Fig. 22 but replacing eccentricities by mass functions, and revealing again two populations of `SB1` solutions, the short-period ones being characterized by very small mass functions $f(\mathcal{M})$. The origin of this population of short-period SB1 solutions among RGB/AGB stars clearly needs clarification. In the following, we show that they are associated with poorly defined solutions. It appears indeed that almost all unphysical `SB1` solutions may be eliminated by using the same purely observational criterion as used in Sect. 6.1, and based on the value of the significance of the `SB1` solution (available in Table `nss_two_body_orbit` from the *Gaia* archive), i.e. K_1/σ_{K_1}, K_1 being the semi-amplitude of the first component.

Almost no outlier remains in the $P-R$ (Fig. 21c) and P - $f(\mathcal{M})$ (Fig. 23c) diagrams when that significance exceeds 40, a few outliers remain when it exceeds 20 but many more solutions are kept, as may be seen from Table 4. That table shows that the gradual disappearance of unphysical `SB1` solutions as the significance increases corresponds to a real filtering out of unphysical solutions since the fraction of remaining unphysical solutions truly diminishes as the significance increases (passing from 6.8% in the absence of any filtering to 0.3% when the significance threshold is set at 40; see Table 4). The drawback of a filtering on significance is however that it tends to filter out as well solutions with long orbital periods as those have on average smaller K_1 values (this was very clear as well from Fig. 20). Alternatively, if one does not want to loose the long-period orbits as a result of filtering on significance, filtering is also possible by using the physical condition $P \geq P^{\rm thresh}$ – Eq. 7 – with appropriate mass values; however Fig. 21 reveals that for systems with periods above 10 d, the boundary between physical and unphysical systems does not depend sensitively upon the choice of $\mathcal{M}_1, \mathcal{M}_2$.

Table 4. Sizes of the `SB1` sample involving RGB/AGB primaries for different filtering on the significance threshold. The numbers of rejected and kept sources are given as a function of the significance K_1/σ_{K_1}. The column labelled 'unphys.' lists the number of sources which would have a Roche filling factor larger than unity (or $P < P^{\rm thresh}$ in Eq. (7) thus falling below the cyan dashed line on Fig. 21). The column labelled 'fraction' gives the ratio 'unphys.'/'accepted' (expressed in %).

significance	rejected	accepted	unphys.	(%)
all	0	44706	3056	(6.8%)
> 20	27404	17302	214	(1.2%)
> 40	37850	6856	21	(0.3%)

Now that the sample of RGB/AGB stars has been adequately cleaned of its unphysical orbits, it is possible to investigate the properties of the e - P diagram for giant stars. Figure 24 presents those for bins of increasing radii (as taken from the corresponding `radius_flame` field), as indicated on the figure labels. As expected from the dashed lines in Fig. 21, the minimum period increases with increasing radii. In the following discussion, we adopt $\mathcal{M}_1 = 1.3\,\mathcal{M}_\odot$ and $\mathcal{M}_2 = 1.0\,\mathcal{M}_\odot$ (corresponding to the red dashed line on Fig. 21, and $c_1 = -0.274$ in Eq. 8), as these values match well the observed trend. The above value for c_1 combined with the upper bound of the radius range adopted in each panel of Fig. 24 defines the lower bound on the orbital period $P_{\rm min}$ for $e = 0$. It appears that the upper envelope of the data cloud observed in each panel of Fig. 24 is well fitted by the empirical relation $P = P_{\rm min}(1-e)^3$, represented by the solid black lines in Fig. 24, as already found by Pourbaix et al. (2004) in their analysis of the *Ninth Catalogue of Spectroscopic Binary Orbits* (their Fig. 5). Despite the fact that this curve matches rather well the uppermost data points in almost all panels, it must be stressed that there seems to be no physical justification for this specific analytical form. A closer look at each of these panels reveals however an interesting sub-structure. At the shortest periods, each panel is dominated by a large amount of (nearly) circular orbits caused by circularisation operating in those systems where the giant stars with their convective envelope are close to filling their Roche lobe. As shown above, $P_{\rm min}$ in each panel actually refers to systems where the giants with the shortest radius in the considered range fill their Roche lobe (see e.g. Verbunt & Phinney 1995; Mazeh 2008, for details).

6.2.3. A search for genuine SB1 among giants

The identification of SB1 among highly evolved giants and long-period variables (LPVs) is made difficult by the envelope pulsation (Alvarez et al. 2001; Hinkle et al. 2002; Jorissen 2004; Jorissen et al. 2019). Hence other methods have been used (Jorissen & Frankowski 2008; Sahai et al. 2008; Decin et al. 2020; Ortiz & Guerrero 2021) to identify true binaries. *Gaia*, with its survey combining radial velocity and photometry data, offers however exquisite prospects to disentangle pulsational from orbital RV variations. In that respect, the bottom panel of Fig. 24 offers an interesting benchmark sample of giant stars with $R > 80\,{\rm R}_\odot$ with a SB1-like signature in their RVs. There are 40 such giants if the significance threshold is set at 40.[14] No `Orbital` nei-

[14] Interested readers may set the significance threshold at 20 instead to get more `SB1`-like solutions (namely about 100), especially with long periods for the reasons explained in the text, or use instead the physical filtering $P \geq P^{\rm thresh}$.

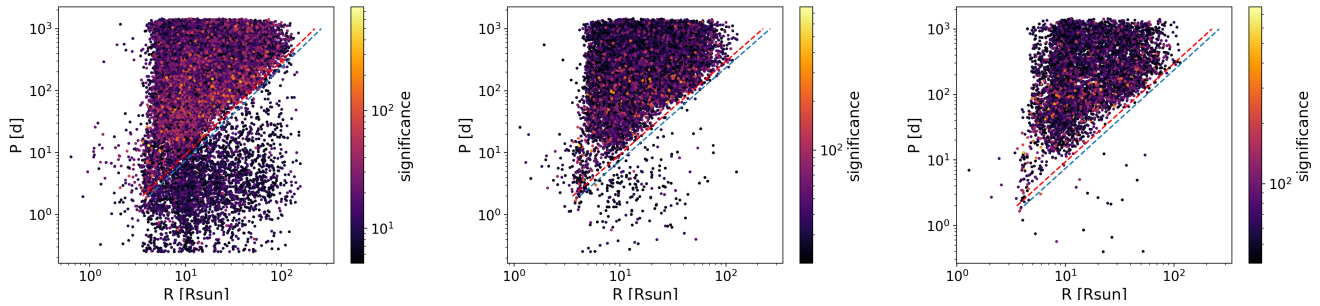

Fig. 21. The period - radius diagram for all SB1 solutions falling along the RGB/AGB, according to the criterion (5), and with a radius available from `radius_flame`. The dashed lines correspond to the threshold periods expressed by Eq. 7 for $\mathcal{M}_1 = 1.3\,\mathcal{M}_\odot$ and $\mathcal{M}_2 = 1.0\,\mathcal{M}_\odot$ (red dashed line) and $\mathcal{M}_1 = 1.3\,\mathcal{M}_\odot$ and $\mathcal{M}_2 = 0.2\,\mathcal{M}_\odot$ (cyan dashed line). *Left (a)*: unfiltered, 44 706 SB1 solutions (among which 3 056 unphysical, i.e., below the cyan dashed line); *middle (b)*: filtered by significance $K_1/\sigma_{K_1} > 20$, 27 404 solutions are rejected and 17 302 are kept (among which 214 unphysical); *right (c)*: filtered by significance > 40, 37 850 solutions are rejected and 6 856 are kept (among which 21 unphysical).

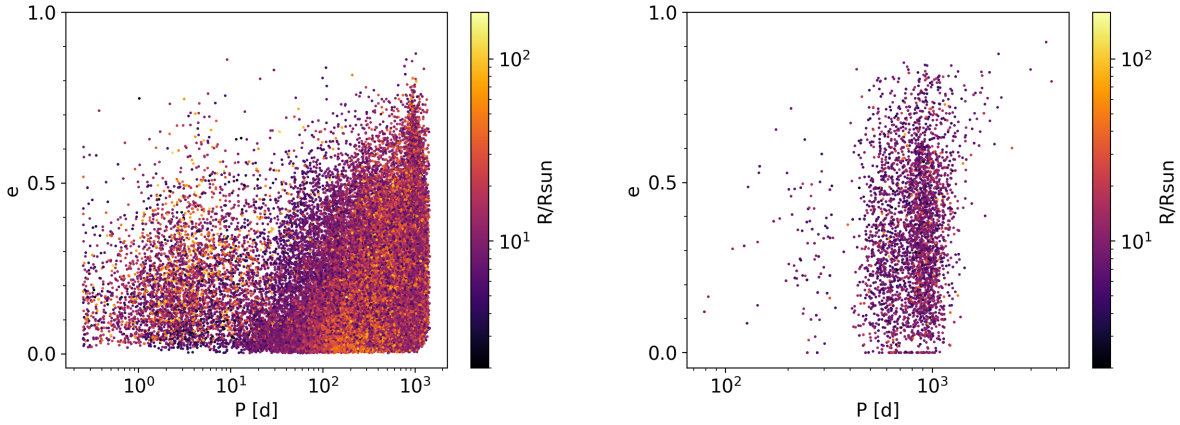

Fig. 22. The *e* - *P* diagrams for all SB1 (*left panel*: unfiltered; adequately filtered *e* - *P* diagrams for SB1 with an RGB/AGB primary is presented in Fig. 24) and astrometric (*right panel*) solutions falling along the RGB/AGB, according to the criterion (5), and with a radius available from `radius_flame`. Note the restricted period scale of the astrometric binaries as compared to the SB1, and the lack of binaries with periods close to 1 yr among astrometric binaries.

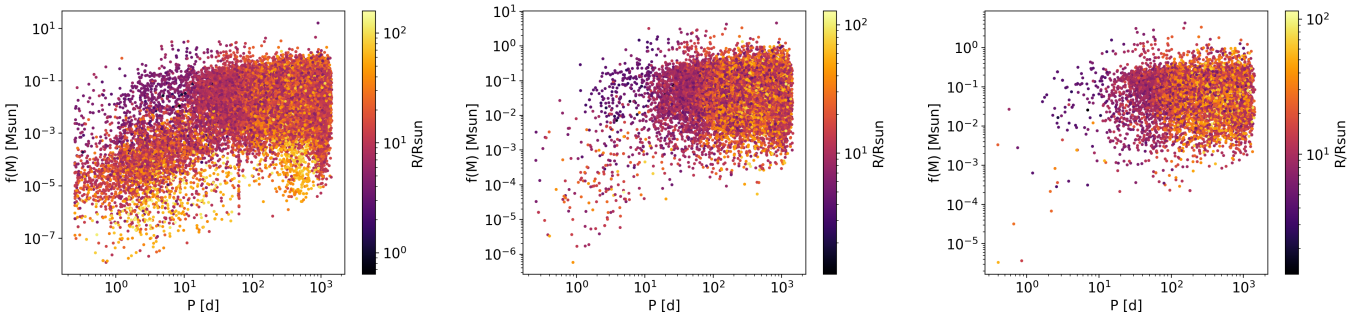

Fig. 23. *P* - $f(\mathcal{M})$ diagrams for SB1 along the RGB/AGB. *Left (a)*: unfiltered. The yellow tail extending down to $f(\mathcal{M}) \sim 10^{-5}\,\mathcal{M}_\odot$ at periods in the range 300 – 800 d corresponds to pseudo-orbits associated to long-period pulsators (see Sect. 6.2.3). *Middle (b)*: filtered by significance > 20 and > 40 (*right (c)*).

ther `AstroSpectroSB1` solutions are present in *Gaia* DR3 among those giants with large radii (compare with Fig. 22). Table 5 lists their main properties, while their location in the HRD is shown as the yellow crosses in Fig. 25.

As mentioned above, since there is the risk that some of these SB1 solutions may be caused by envelope pulsation mistaken as SB1s, a proxy for the amplitude of the photometric variation in the *G* band has been listed as well, namely `phot_g_mean_mag_error` from the `gaia_source` table. A crossmatch has been performed as well with table `vari_long_period_variable` and the photometric period, whenever available, has been listed in the column $P_{\rm lpv}$. It appears that only one LPV is present in this list (a carbon star also known as V688 Cas), as confirmed by its largest ΔG value in Table 5. Since $P_{\rm lpv} = P_{\rm nss}$ for this star, the RV variations are not due to orbital motion but to envelope pulsations. Many other

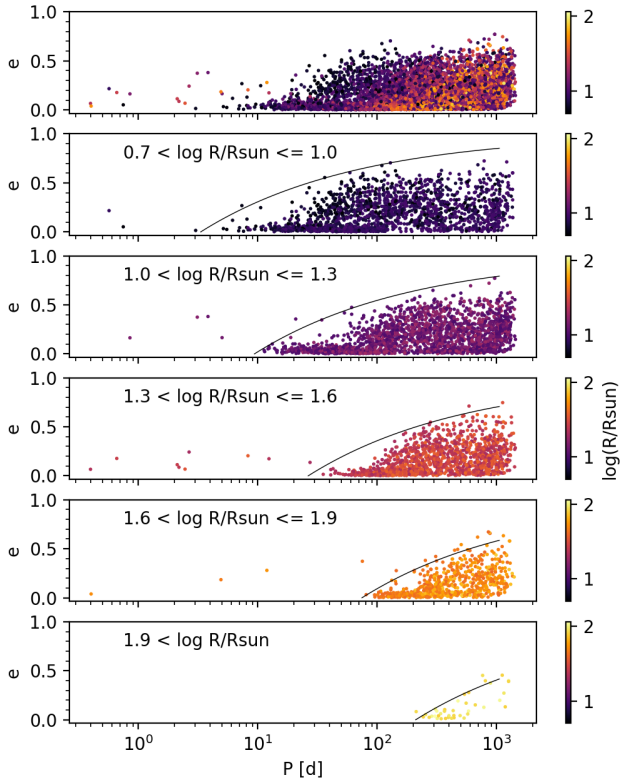

Fig. 24. The e - P diagram for SB1 systems along the giant branch, filtered according to significance factors larger than 40, for various radius spans. The top panel is the full sample. The solid black lines correspond to the loci such that $P(1-e)^3$ is constant (see text). The sample sizes are, from top to bottom, 1960, 2358, 1643, 737, and 40. The location in the HRD of the SB1 systems with $0.7 < \log(R/\mathrm{R}_\odot) \leq 1.0$ (*second panel from top*), $1.3 < \log(R/\mathrm{R}_\odot) \leq 1.6$ (*fourth panel from top*) and $1.9 < \log(R/\mathrm{R}_\odot)$ (*bottom panel*) is shown in Fig. 25.

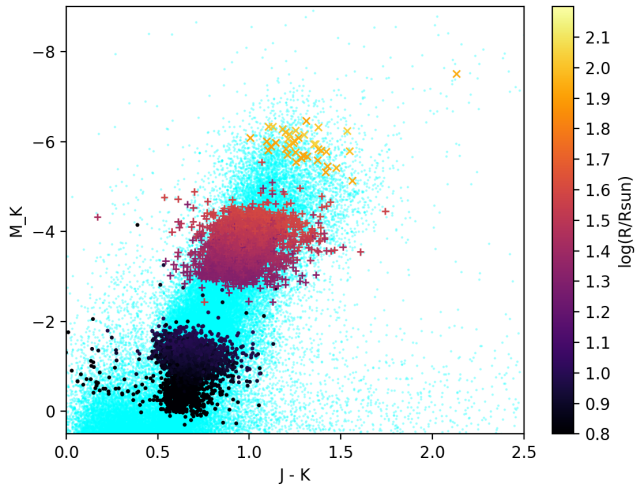

Fig. 25. Location in the HRD of three among the samples displayed in Fig. 24, namely $0.7 < \log(R/\mathrm{R}_\odot) \leq 1.0$ (dots), $1.3 < \log(R/\mathrm{R}_\odot) \leq 1.6$ (plusses) and $1.9 < \log(R/\mathrm{R}_\odot)$ (crosses). Small cyan dots correspond to the SB1 not selected by our selection criteria. See Table 5 for a full discussion of the properties of the yellow crosses.

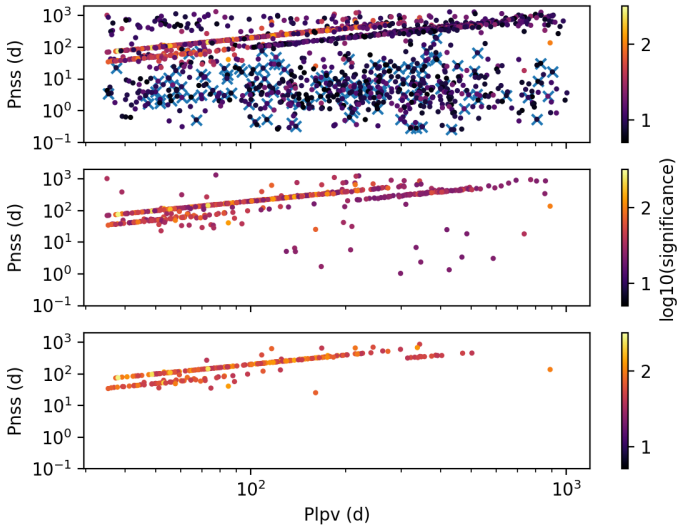

Fig. 26. Orbital period from the `nss_two_body_orbit` table versus photometric period from the `vari_long_period_variable` table. The *top, middle* and *bottom panels* correspond to different filtering based on the SB1 significance factor (respectively, larger than 5 – default in the NSS table –, larger than 20, and larger than 40). The two sequences observed in all panels correspond to $P_{\rm lpv}/P_{\rm nss} = 0.5$ (ellipsoidal variables; upper sequence), $P_{\rm lpv}/P_{\rm nss} = 1$ (LPVs or rotational modulation in a synchronised system; lower sequence). In the *top panel*, the crosses denote NSS solutions for which the Roche-lobe filling factor is above unity, and are thus unphysical. The filtering with significance larger than 40 makes them disappear almost entirely.

such cases will be discussed below (Table 6). There are only 4 other stars appearing in the `vari_long_period_variable` table in common with Table 5, and these four have the unexpected property that $P_{\rm lpv} = 0.5\ P_{\rm nss}$, with a moderate ΔG value (on the order of 0.001 – 0.003 mag). We argue below in relation with Table 6 that these are ellipsoidal variables, thus true binaries where the giant primary is close to filling its Roche lobe. Based on the fact that these ellipsoidal variables identified in table `vari_long_period_variable` have small eccentricities ($e < 0.1$), we suspect that Table 5 contains many more such ellipsoidal variables, namely those with $e < 0.1$ and $\Delta G > 0.001$ mag, flagged as 'Ell. var.?' in the last column of Table 5.

The longest period found in Table 5 is 1261 d, a value well in line with the *Gaia* DR3 time span, but short with respect to the periods expected among evolved giants (consider for instance the 17 yr period found by Jorissen et al. 2019 for the carbon Mira V Hya). Such long periods are not detectable at the current stage of the *Gaia* mission neither as SB1 nor as astrometric binaries. Nevertheless, one may look for acceleration solutions (there is only one solution from table `nss_acceleration_astro` matching the giant criteria defining Table 5; about acceleration solutions, see Sect. 4.2.3 and Wielen et al. 1999; Makarov & Kaplan 2005; Frankowski et al. 2007; Kervella et al. 2019a, 2022; Brandt 2021) or for solutions with a trend in the RVs (121 solutions for giants found in `nss_non_linear_spectro`, not listed here).

Table 5. Source id and basic parameters for SB1 and acceleration solutions with significance larger than 40 for giants with $R > 80\,R_\odot$ (bottom panel of Fig. 24). The radius R is from FLAME. The column labeled ΔG gives a proxy of the variability in the G band (see text). The column labeled $P_{\rm lpv}$ lists the period obtained by the photometric analysis (table vari_long_period_variable), whereas $P_{\rm nss}$ corresponds to the period of the SB1 orbit.

source_id	R ($R_\odot$)	significance	ΔG (mag)	G (mag)	e	$P_{\rm nss}$ (d)	$P_{\rm lpv}$ (d)	Alt. id	Rem.
				SB1					
1825471125022885760	111	62	0.0006	11.74	0.19	475			
1963830094814564992	98	71	0.0025	9.48	0.06	340	183		Ell. var.
1972501599433801856	104	82	0.0026	11.21	0.04	286	143		Ell. var.
1993611806061037824	91	45	0.0011	11.66	0.05	255			Ell. var.?
1996190371286907904	81	51	0.0005	11.65	0.10	368			
2022016864326072832	81	53	0.0002	12.25	0.13	1182			
203396083342181248	79	55	0.0004	11.48	0.28	851			
2072346498024572672	83	49	0.0006	11.67	0.40	805			
2153213619706962304	85	97	0.0008	8.92	0.02	395		BD+56 2152[a]	
2179330422489474304	100	63	0.0007	11.27	0.40	1261			
2189793031540178560	109	46	0.0010	11.33	0.09	582			
2190661233409369728	81	179	0.0008	9.75	0.26	538			
2198983058969830272	91	148	0.0019	10.03	0.06	573			Ell. var.?
2203704946009240576	85	78	0.0007	11.05	0.15	663			
3023454391367052928	79	52	0.0023	11.52	0.02	513			Ell. var.?
3385138711262550144	107	48	0.0012	10.34	0.20	1063			
3441375569926160768	82	72	0.0004	8.58	0.45	1115		BD+26 935[b]	
4309778580925549312	86	78	0.0024	11.75	0.08	212	106		Ell. var.
4538064682637397504	81	55	0.0005	10.47	0.02	440			
4657870428934536960[c]	87	58	0.0107	11.71	0.09	366	375	V688 Cas[d]	Mira
468328667095902720	82	109	0.0008	11.31	0.01	374			
4479122750503280512	100	64	0.0009	10.89	0.11	307			
519141188227099776	89	46	0.0004	11.04	0.02	420			
5340777165298298880	83	53	0.0014	11.57	0.02	273			Ell. var.?
5354875859285271936	89	50	0.0003	9.56	0.45	764			
5355550645876247808	95	49	0.0014	12.44	0.04	399			Ell. var.?
5405499126983935872	83	40	0.0018	13.07	0.03	243	122		Ell. var.
5406434021101010176	102	40	0.0010	10.28	0.01	319			
5604143357268838400	80	53	0.0007	9.97	0.04	327			
5697523299266655104	81	108	0.0007	10.69	0.28	585			
5697806664034217216	98	65	0.0009	10.59	0.37	889			
5796104824632537600	86	104	0.0018	10.12	0.17	556			
5806597567164955776	88	55	0.0018	10.94	0.09	433			Ell. var.?
5835609040544745344	108	40	0.0007	11.46	0.09	315			
5847195453486047616	105	56	0.0009	9.74	0.13	782			
5854104780242997504	92	49	0.0003	12.22	0.04	495			
5878621900997292800	92	114	0.0004	12.20	0.02	534			
5888442292197648000	115	40	0.0018	12.08	0.04	305			Ell. var.?
6012575363926683648	84	44	0.0014	12.43	0.04	439			Ell. var.?
6056302632126821760	84	43	0.0005	12.05	0.39	1261			
6057537697261452288	86	86	0.0004	11.02	0.01	343			
992206959423861888	94	43	0.0022	9.72	0.27	1152			
				Acceleration solution					
6665511449204071424	92	28	0.0013	4.19	-	-	-	HD 190421	

[a] Limb-darkened diameter of 0.393 mas from Cruzalèbes et al. (2019), or 96 $R_\odot$ with the *Gaia* DR3 parallax of $\varpi = 0.44$ mas [b] Limb-darkened diameter of 0.672 mas from Cruzalèbes et al. (2019), or 106 $R_\odot$ with the *Gaia* DR3 parallax of $\varpi = 0.68$ mas [c] Since $P_{\rm nss} = P_{\rm lpv}$, the RV variations are due to atmospheric pulsations rather than to orbital motion [d] also CGCS 396 in the General Catalog of Cool Galactic Carbon Stars, flagged as Mira variable.

6.2.4. Combining photometry and spectroscopy to diagnose RV variations in giants: pulsation, ellipsoidal variables, and rotational modulation

Initially with the aim to further investigate how many LPVs may be mistaken as SB1, we searched for targets in com-

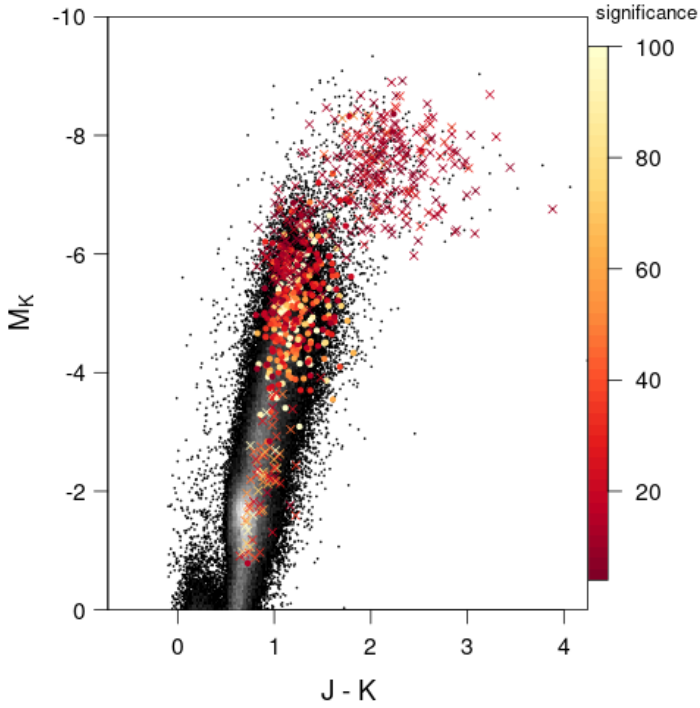

Fig. 27. Location in the infrared colour - magnitude diagram of the stars with $0.45 \leq P_{\rm lpv}/P_{\rm nss} \leq 0.55$ (ellipsoidal variables) from Table 6 (dots). Stars with $0.95 \leq P_{\rm lpv}/P_{\rm nss} \leq 1.05$ are represented by crosses. They appear in two different locations, among LPVs with low orbital significance on one hand, and among less luminous giants with much larger orbital significance perhaps suggesting starspot modulation or short-period pulsators. The dots ($P_{\rm lpv}/P_{\rm nss} \sim 0.5$) fall in between these two groups, as they are located just below the tip of the RGB.

mon between `SB1` from the NSS `nss_two_body_orbit` table and LPVs as provided by the variability study in the `vari_long_period_variable` table. But this cross-match has revealed some surprises. The query

```
SELECT * from gaiadr3.nss_two_body_orbit TBO,
gaiadr3.vari_long_period_variable LPV where
LPV.source_id = TBO.source_id and LPV.frequency is
not null
```

yields 1869 entries, as shown on Fig. 26. The three panels differ in terms of the level of filtering applied on the `SB1` significance parameter, as defined above: > 5 (default, top panel), > 20 (middle panel), and > 40 (bottom panel). Striking are the two straight sequences observed in all three panels. The upper sequence corresponds to $P_{\rm lpv}/P_{\rm nss} = 0.5$ (as expected for ellipsoidal variables), whereas the lower sequence corresponds to $P_{\rm lpv}/P_{\rm nss} = 1$ (as expected for pulsating stars or rotational modulation in a synchronised system). The lower sequence is further made of two distinct clumps, one at short periods ($P_{\rm lpv} \lesssim 100$ d; starspot modulation on a spin-orbit synchronised star?) and the other at long periods ($200 \lesssim P_{\rm lpv} \lesssim 1\,000$ d; LPVs). They will be discussed in turn in what follows.

Ellipsoidal variables

Besides the obvious property of their light-to-RV period ratio equal to 0.5, the ellipsoidal-variable sequence is further confirmed from its following properties: (i) small eccentricities ($e \lesssim 0.1$), (ii) large filling factors ($R_1/R_{R,1} \gtrsim 0.65$ from Eq. 6, adopting radii from `FLAME` and the same typical masses as above – $\mathcal{M}_1 = 1.3\ \mathcal{M}_\odot$, $\mathcal{M}_2 = 1.0\ \mathcal{M}_\odot$) whenever available, and (iii) small G amplitudes ($0.01 \leq \Delta G \leq 0.1$ mag; see Table 6). The ellipsoidal nature of these stars has been confirmed from the comparison between the light and RV curves. As expected, the maximum light indeed occurs at the quadratures, when the RV is maximum or minimum. In Fig. 24, at any given radius range, these ellipsoidal variables are located in the nearly circular tail of each panel. The full list of ellipsoidal variables is not provided here as the reader may easily obtain it from the ADQL query mentioned at the beginning of this section and filtering on $P_{\rm lpv}/P_{\rm nss}$ around 0.5 (370 stars in the inclusive range 0.45 – 0.55, most of them having significances in excess of 20). The first part of Table 6 nevertheless lists a few examples, randomly selected. Figure 27 shows the position in the 2MASS infrared colour-magnitude diagram ($M_K, J-K$) of the 370 stars with $0.45 \leq P_{\rm lpv}/P_{\rm nss} \leq 0.55$ (dots). These ellipsoidal variables are located from the tip of the RGB[15] to 3 magnitudes below. We note that some among these stars might be young, pre-main sequence stars. *Gaia* DR3 2162167694508896128 = V1540 Cyg listed in Table 6 is one such case (on Fig. 27, it is located at $M_K = -6.2$ and $J-K = 1.41$).

Long-period variables

The transition between dots and crosses in Fig. 27 corresponds to the transition across the RGB tip. Above the RGB tip, most stars from the `vari_long_period_variable` table belong to the sequence $P_{\rm lpv}/P_{\rm nss}$ around unity. They correspond to LPVs with a RV variation caused by the envelope pulsation. Although displayed in Fig. 27, the full source list is not given here as they are easily obtained in a way similar to that discussed above for ellipsoidal variables. Table 6 nevertheless lists a few examples, randomly selected.

These LPVs are easily identified by their velocity semi-amplitudes smaller than 10 km s^{-1} (in that sense, they differ markedly from the ellipsoidal variables which generally have much larger K_1 values) and periods in excess of 180 d, as expected for Mira pulsations (Alvarez et al. 2001; Hinkle et al. 2002). Hence, given these relatively small values of K_1, the significance of the SB1-like solution (namely K_1/σ_{K_1}) may in several cases be smaller than 20, but the identity of the NSS and LPV periods is *per se* an indication of the reliability of the RV model. We note that the filling factor has no meaning in this stellar category since there is no true orbit associated. Mira variables are recognized as well by their large amplitude in G (> 0.1 mag). The pseudo-eccentricities found by Hinkle et al. (2002) for Miras and semi-regular variables were clustered around 0.35, with a few cases below 0.1 as well. Here the pseudo eccentricities range all the way from 0.09 to 0.48 (Table 6). Furthermore, it has been checked that the maximum RV is reached at phase 0.8 while maximum light is reached at phase 1.0, a phase lag expected for Mira pulsators. Furthermore, since for these stars K_1 is relatively small and P is long, the pseudo mass functions are consequently smaller than $10^{-3}\ \mathcal{M}_\odot$, with some values as small as $10^{-5}\ \mathcal{M}_\odot$, in agreement with the findings of Hinkle et al. (2002) (their Table 2) for Mira and semi-regular variables. LPVs with low values of $f(\mathcal{M})$ are most clearly seen on Fig. 23a as the yellow tail extending down to $f(\mathcal{M}) \sim 10^{-5}\ \mathcal{M}_\odot$ for periods between 300 d and 1 000 d. On that same figure, a lot more stars with large radii ($R > 100\,R_\odot$) are found at shorter periods, but those are spurious 'SB1-like' solutions since their periods do not even match the LPV one, and when available, their filling factors are above unity, which is non-physical. Their mass functions are quite small either (down to $10^{-8}\ \mathcal{M}_\odot$). Therefore these targets

[15] $M_{\rm K,RGB-tip} = -6.49$ as derived from Lebzelter et al. (2019) who find $K_{\rm RGB-tip} = 12$ for the LMC and considering its distance modulus 18.49± 0.09 mag (de Grijs et al. 2017).

Table 6. A few illustrative examples of ellipsoidal variables ($P_{\rm lpv}/P_{\rm nss}$ = 0.5) mistaken as LPVs in the `vari_long_period_variable` table, LPVs with a pseudo `SB1` orbit ($P_{\rm lpv}/P_{\rm nss}$ = 1, ΔG > 0.1 mag, $P_{\rm lpv}$ > 180 d) in the `nss_two_body_orbit` table and short-period ($P_{\rm lpv}$ < 100 d) 'LPVs' with $P_{\rm lpv}/P_{\rm nss}$ = 1. Radii are the `FLAME` DR3 estimates (see text for how the filling factors R/R_R were estimated). The column labelled ΔG lists the field `mad_mag_g_fov` (median absolute deviation) from table `vari_summary`.

Gaia DR3 id	$P_{\rm lpv}$ (d)	$P_{\rm nss}$ (d)	$P_{\rm lpv}/P_{\rm nss}$	signif.	K_1 (km/s)	e	ΔG (mag)	$f(\mathcal{M})$ ($\mathcal{M}_\odot$)	R/R_R	R ($R_\odot$)	Alt. id.
Ellipsoidal variables											
2162167694508896128[a]	143 ± 16	289 ± 0.2	0.49	249	34.6	0.02	0.02	1.25			V1540 Cyg
5871624883899265280	48 ± 3	95.1 ± 0.1	0.50	101	22.0	0.03	0.06	0.105	0.92	43	
4490881713827188 48	178 ± 50	356.7 ± 1.5	0.50	73	12.8	0.01	0.09	0.078			
528840770565380352	54 ± 4	108.6 ± 0.1	0.50	89	31.7	0.01	0.06	0.358	0.88	45	
1837292073273265920	58 ± 3	116.1 ± 0.1	0.50	86	34.1	0.04	0.06	0.477			
4305358093199399168	42 ± 2	84.8 ± 0.1	0.50	89	27.3	0.03	0.05	0.178	0.74	32	
6653811713476525440	63 ± 4	125.4 ± 0.6	0.50	19	11.4	0.16	0.09	0.019	0.67	37	
5933194270923372288	10 ± 17	219.4 ± 0.4	0.50	63	21.8	0.05	0.05	0.234			
5998937575770407936	69 ± 9	137.1 ± 0.2	0.50	50	21.7	0.05	0.07	0.144	0.75	45	
...											
Large-amplitude (ΔG > 0.1 mag) LPVs (Mira or SRa,b) with a pseudo SB1 orbit											
3029929312263388416	330 ± 39	329 ± 3	1.002	27	5.6	0.27	0.27	0.0057			
5861476288517412096	351 ± 29	350 ± 4	1.003	22	7.4	0.14	0.25	0.0144			
4498570706006456320	196 ± 11	196 ± 2	1.003	9	3.5	0.36	0.21	0.0008			
6635121600650977280	310 ± 42	309 ± 2	1.003	18	2.9	0.29	0.13	0.0007	-	75	
185224454669173120	491 ± 114	490 ± 9	1.003	9	2.6	0.34	0.29	0.0009			
5522324157261027968	321 ± 37	320 ± 3	1.003	23	5.3	0.29	0.26	0.0046			
5428546471231540608	455 ± 60	454 ± 6	1.003	7	2.8	0.33	0.24	0.0009			
463720476424410624	353 ± 24	352 ± 3	1.004	34	7.5	0.17	0.26	0.0152			
6358622017131465728	181 ± 7	180 ± 2	1.004	10	6.4	0.17	0.54	0.0048	-	138	
2180493018598279296	178 ± 25	177 ± 2	1.004	11	2.3	0.09	0.12	0.0002			
5318375436185802368	262 ± 32	260 ± 2	1.005	12	2.6	0.33	0.18	0.0004	-	97	
5522970154700635392	412 ± 37	410 ± 8	1.005	14	5.6	0.04	0.49	0.0076	-	84	
1989628623330891904	419 ± 18	[25 ± 0.02][b]	[16.7][b]	21	6.6	0.39	0.60	0.0006			
...											
Genuine binaries among LPVs ($P_{\rm lpv}/P_{\rm nss} \neq 0.5$ or 1; see text)											
5341773936978279296	220 ± 61	1252 ± 113	0.18	21	7.7	0.25	0.05	0.053	0.28	73	
5597415372601747456	168 ± 54	656 ± 6	0.26	43	11.1	0.36	0.03	0.076	0.33	56	
5414646307794529792	196 ± 42	753 ± 17	0.26	34	6.2	0.4	0.04	0.015			
5875470387113872768	214 ± 28	746 ± 16	0.29	29	15.3	0.35	0.09	0.229			
5347893273248921984	279 ± 75	913 ± 40	0.31	29	13.3	0.07	0.03	0.220			
5404683839108805248	215 ± 28	662 ± 1	0.32	89	11.5	0.33	0.11	0.088			
5796098502440628864	244 ± 28	701 ± 4	0.35	59	6.5	0.08	0.08	0.020			
1642955252784454144	374 ± 93	503 ± 6	0.74	33	6.0	0.28	0.04	0.010			
3047170762697743 36	310 ± 102	158 ± 1	1.96	22	12.0	0.01	0.10	0.028	0.39	26	
6661657003818388480	197 ± 92	42 ± 0.1	4.66	32	26.3	0.11	0.04	0.078	0.25	7	
187075684355571200	161 ± 64	26 ± 0.01	6.29	73	22.9	0.08	0.05	0.031			
5473442554645523712	209 ± 57	32 ± 0.02	6.62	30	36.4	0.06	0.04	0.157			
Short-period ($P_{\rm lpv}$ < 100 d) light and RV variations with $P_{\rm lpv}/P_{\rm nss}$ = 1: starspot modulation or short-period pulsators ?											
5498026500770376576	46 ± 1	45.7 ± 0.12	1.003	10	4.9	0.41	0.14	0.0005			
4498425604828703104	50 ± 4	49.57 ± 0.05	1.003	39	32.5	0.03	0.08	0.18	0.24	7	
3047643956417931264	64 ± 1	63.4 ± 0.1	1.003	13[c]	8.3	0.21	0.24	0.0036	1.44[c]	52	
5637220068643463424	57 ± 4	57.17 ± 0.03	1.004	66	33.6	0.04	0.06	0.2240	0.27	9	
5883587875302126592	78 ± 4	78.1 ± 0.1	1.004	16	12.2	0.42	0.08	0.0128			
5701792904776417152	43 ± 4	43.38 ± 0.01	1.005	85	25.2	0.02	0.06	0.0718			
1869696952997313664	53 ± 3	52.56 ± 0.05	1.005	31	22.5	0.13	0.08	0.0610	0.26	8	
5235000057883364864	43 ± 1	42.5 ± 0.03	1.005	30	35.6	0.10	0.06	0.1969	0.40	11	
...											

Notes. [(a)] This is likely a young star, of 'Orion-variable' type (V1540 Cyg). [(b)] This star has been added to the Mira category despite its $P_{\rm lpv}/P_{\rm nss}$ ratio vastly different from 1, to illustrate some kind of aliasing problems (see text) [(c)] Doubtful case: significance is only 13 and filling factor is 1.4.

cannot be genuine binaries.

Genuine binaries

Genuine binaries among Miras are expected to have orbital periods much larger than currently detectable by *Gaia* DR3 (as is the case for instance for the carbon Mira V Hya quoted above). Intriguingly, several genuine SB1 have nevertheless been found among stars with $P_{\rm lpv} > 150$ d, a property generally associated to LPVs. In the fourth part of Table 6 are listed 14 SB1s selected among the 1189 `SB1` solutions in common with the `vari_long_period_variable` table. These SB1s have a significance larger than 20, the 1σ confidence range of $P_{\rm lpv}/P_{\rm nss}$ falling outside the ranges 0.45 – 0.55 and 0.9 – 1.1 (to avoid SB1-like variations caused by pulsations), $P_{\rm nss} > 20$ d and $P_{\rm lpv} > 150$ d. Their RV curves where checked visually and showed no peculiarity that would make the solution dubious. This visual inspection nevertheless revealed that some kind of aliasing problems remain with the NSS SB1 periods. The star *Gaia* DR3 1989628623330891904 was originally considered as a possible genuine binary among LPVs, since $P_{\rm lpv} = 419$ d as compared to $P_{\rm nss} = 25$ d. However, the visual inspection of the RV curve revealed that the LPV period of 419 d is clearly present in the RV curve, although it was not selected by the period-selection algorithm, which gave no warning about a possible problem with that solution (significance = 2, period confidence = 1.000, ruwe = 1.09) except for the goodness-of-fit of 2.5. Therefore, that star has been added to the 'Large-amplitude LPVs' section.

Rotational modulation on a spin-orbit synchronised star

The final category of interest in Table 6 contains targets with short periods (i.e., $P \lesssim 100$ d) on the $P_{\rm lpv}/P_{\rm nss} = 1$ sequence. They are listed in the fourth part of Table 6 and identified in the HRD of Fig. 27 as the crosses at the bottom of the giant branch. Contrarily to the situation prevailing for ellipsoidal variables and long-period variables discussed above, the phase lag between velocity and light curves now appears to be anything between 0 and π. For this reason, their light variation could be due to starspot modulation on a spin-orbit synchronised primary star (e.g., Mazeh 2008). Less likely, they could be small-amplitude pulsating stars.

6.3. Identifying EL CVn systems in Gaia data

EL CVn systems are short-period eclipsing binaries (EBs) consisting of an A/F-type main-sequence (MS) primary and a low-mass pre-helium white-dwarf (pre-He-WD) secondary. These systems are a result of mass transfer from the evolved pre-He-WD progenitor to the currently observed primary star (e.g. van Kerkwijk et al. 2010; Maxted et al. 2011; Rappaport et al. 2015). EL CVn systems are at a rare stage of binary evolution in which the young pre-He-WD is bloated, with a radius of up to $\sim 0.5\,R_\odot$, and hotter than the more luminous A/F-type primary. As a result, such systems, harboring a low-mass white-dwarf (WD) precursor, are detectable even in ground-based photometric surveys. EL CVn's with smaller and cooler He-WD secondaries can be detected in space photometry (Faigler et al. 2015) . Consequently, 10, 18 and 36 such systems were discovered in the *Kepler* (van Kerkwijk et al. 2010; Carter et al. 2011; Breton et al. 2012; Rappaport et al. 2015; Faigler et al. 2015), WASP (Maxted et al. 2011, 2014), and PTF (van Roestel et al. 2018) photometric surveys, respectively.

The detection of these systems in photometric surveys is based on identifying an eclipsing-binary folded light curve with a 'boxy' deeper eclipse (steep ingress and egress and a flat bottom) and a shallower eclipse with a limb-darkening curved bottom. In an EL CVn, the deeper 'boxy' eclipse is actually the secondary eclipse (total eclipse of the pre-He-WD secondary by the MS primary), while the shallower eclipse is the primary eclipse (pre-He-WD transit of the primary star). This is because the pre-He-WD secondary is hotter than the primary. Such photometric detections usually require confirmation through follow-up spectroscopic radial-velocity (RV) observations, that enable identifying the light-curve primary and secondary eclipses from the RV-curve phase.

The *Gaia* data, however, enable direct detection of EL CVn systems by combining the *Gaia* photometry and RV data. Figure 28 shows the folded *Gaia* G, $G_{\rm BP}$, and $G_{\rm RP}$ photometry and RV data, for a known EL CVn-type system (HD 23692, Maxted et al. 2014), together with the Transiting Exoplanet Survey Satellite (TESS; Ricker et al. 2015) binned data. Detrending of the TESS data was done using cosine detrending following Faigler et al. (2015). The *Gaia* EB-model period and deeper-eclipse epoch were used as the folding period and phase zero, respectively. The RV plot enables identifying the phase-zero eclipse as the *secondary* eclipse, and the 0.5-phase eclipse as the *primary* eclipse. The figure shows that for this system, indeed the secondary eclipse is 'boxy' shaped and deeper than the primary one, the main signatures of an EL CVn system. In addition, we see that the $G_{\rm BP}$ secondary eclipse is much deeper than the $G_{\rm RP}$ one, an additional indication for the high temperature of the secondary.

6.3.1. Sorting through the *Gaia* data

To build the initial sample, from which we can identify EL CVn systems, we selected from the *Gaia* DR3 data systems with:

1. An eclipsing-binary solution from *Gaia* photometry, and
2. A spectroscopic-binary (SB) solution (`SB1`, `SB1C`, `SB2` or `SB2C`) derived from the *Gaia* RV data, and
3. An orbital-frequency difference between the EB and SB solutions smaller than $\frac{1}{100}$ d^{-1}, and
4. An orbital period shorter than 2 d.

The maximum orbital-frequency difference was selected as significantly larger than the inverse of data time span ($\sim 1\,000$ d), a rough estimate for the orbital-frequency uncertainty lower limit. Limiting the orbital-frequency difference to $\frac{1}{500}$ d^{-1} yielded the same sample. An orbital-period limit of 2 days was chosen since most discovered EL CVn systems are below it (See Fig. 5 of van Roestel et al. 2018). These criteria resulted in an initial sample of 1174 systems.

Next, we calculated the phase difference between the SB-model primary eclipse and the EB-model deeper eclipse, for all stars in our sample. For a common binary, for example one consisting of two MS stars, we expect this phase difference to be zero. However, for an EL CVn, in which the secondary is hotter hence the secondary eclipse is deeper, we expect the phase difference to be ~ 0.5, assuming a small eccentricity. Figure 29 shows the phase-difference histogram of our initial sample, with a main peak at phase zero, and a much smaller peak at phase 0.5, as expected.

Based on this, we selected an initial list of EL CVn candidates with:

1. Eclipses phase difference in the 0.4 – 0.6 range, and
2. Eccentricity smaller than 0.3, and

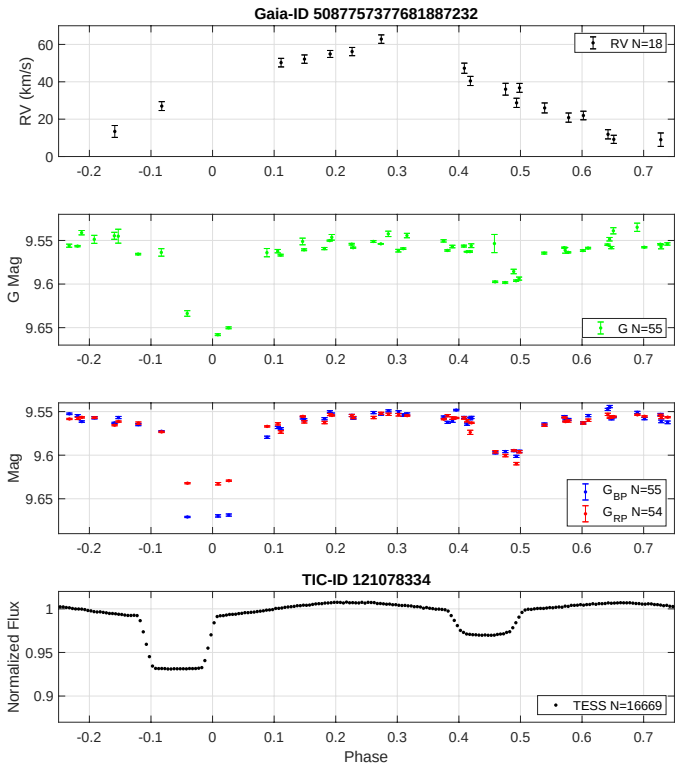

Fig. 28. Folded *Gaia G*, G_{BP}, and G_{RP} photometry and RV data of HD 23692, together with TESS binned data. Top panel shows the *Gaia* RV data. Second panel presents the *Gaia G* data. Third panel shows the *Gaia* G_{BP} and G_{RP} data, with medians shifted to the *Gaia G* median, for clarity. Bottom panel presents the TESS data binned to 200 phase bins. All plots were folded using the *Gaia* EB-model period and deeper-eclipse epoch as the folding period and phase zero, respectively. Note that the primary eclipse is at phase *0.5*, while the secondary eclipse is at phase *zero*. Observed TESS-eclipse phase drift is due to more than 1300-day of delay from the last *Gaia* point to the first TESS point. For clarity, the three bottom panels use the same y-axis scale.

3. EB-model eclipse-depth difference with a signal-to-noise ratio (SNR) larger than 5.

The eclipse-depth difference SNR was required since our method relies on reliably identifying a secondary eclipse that is significantly deeper than the primary one. These criteria yielded 16 systems.

Finally, we visually inspected the *Gaia* photometry and RV data and models of the 16 systems in our initial list, and identified 5 systems as the most promising EL CVn candidates.

6.3.2. Five EL CVn-type candidates

After identifying the 5 EL CVn candidates we realized that all have a *Gaia* `SB1` model, and one of them is actually a known EL CVn-type system (*Gaia* DR3 5087757377681887232 (G5087); TIC-ID 121078334; HD 23692; Maxted et al. 2014), which is shown in Fig. 28. This system serves as an initial validation for our discovery method and the rest of the candidates. Figure 30 shows the *Gaia* and TESS data (except for *Gaia* DR3 2048990809445098112 (G2048), for which we could not find TESS photometry) of the four new candidates using the Fig. 28 presentation. A selected set of *Gaia* parameters of the 5 candidates are listed in Table 7.

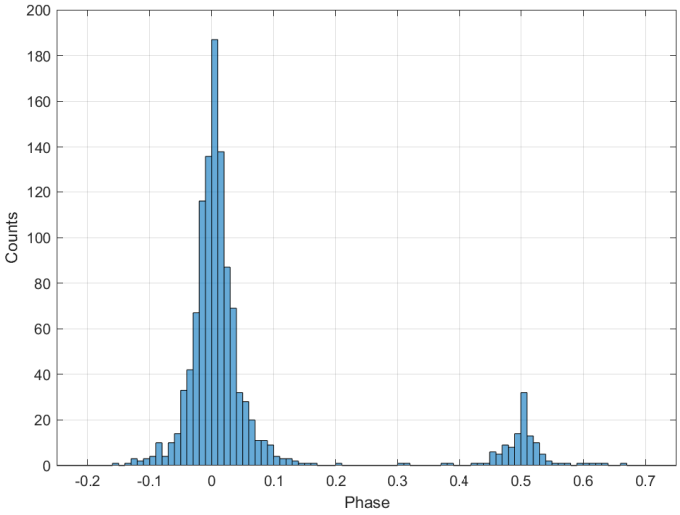

Fig. 29. Histogram of phase difference between SB-model primary eclipse and EB-model deeper eclipse, for 1174 stars in our sample.

In principle, one can use the rich *Gaia* photometry, RV, and derived properties, together with the TESS data, to fit an astrophysical model and estimate the pre-He-WD mass, radius, effective temperature and other properties. Such an analysis was performed by e.g. Maxted et al. (2014), Faigler et al. (2015) and van Roestel et al. (2018) for multiple EL CVn systems they identified. However, this analysis is beyond the scope of this 'teaser' paper.

6.4. Ultracool dwarf binaries

Multiplicity studies of ultracool dwarfs (UCDs, which comprise both very low-mass stars and brown dwarfs) at separations $\lesssim$1 au have for long been hampered by the relative faintness of those objects and the associated observational limitations. The separation and mass (or magnitude)-ratio distribution of known UCD binaries therefore carries a significant observational bias, which is also affecting the estimated UCD binary fraction of 10-30% (e.g. Burgasser et al. 2007). Surveys of small samples indicate that the occurrence of compact UCD binaries is significant (Blake et al. 2010; Bardalez Gagliuffi et al. 2014; Sahlmann et al. 2014b) and that many of those systems have photocentre orbit amplitudes in the range of mas. It has therefore been predicted that *Gaia* astrometry will eventually characterize hundreds of UCD binary orbits (Sahlmann et al. 2014a) and significantly improve our knowledge on the occurrence and properties of compact UCD binaries.

Here we have a first look at the UCD orbits in *Gaia* DR3. Figure 31 shows the *Gaia* colour-magnitude diagram of all sources with `nss_solution_type = OrbitalTargetedSearch*`. Large grey circles indicate the known UCD sources from the *Gaia* Ultra-cool Dwarf Sample (GUCD, Smart et al. 2019), where we used the `gaiaedr3.dr2_neighbourhood` table to match a `source_id` from *Gaia* DR2 to *Gaia* DR3.

The only non-single star solutions for GUCD sources are found in the `nss_two_body_orbit` table with solution type `OrbitalTargetedSearch*`. No GUCD could be matched with an `Orbital` solution or an acceleration solution. This is mainly because a large fraction (~75%) of GUCDs are fainter than the $G < 19$ cut-off for processing with the nominal NSS pipelines (Halbwachs et al. 2022). As described in Holl et al. (2022b), the

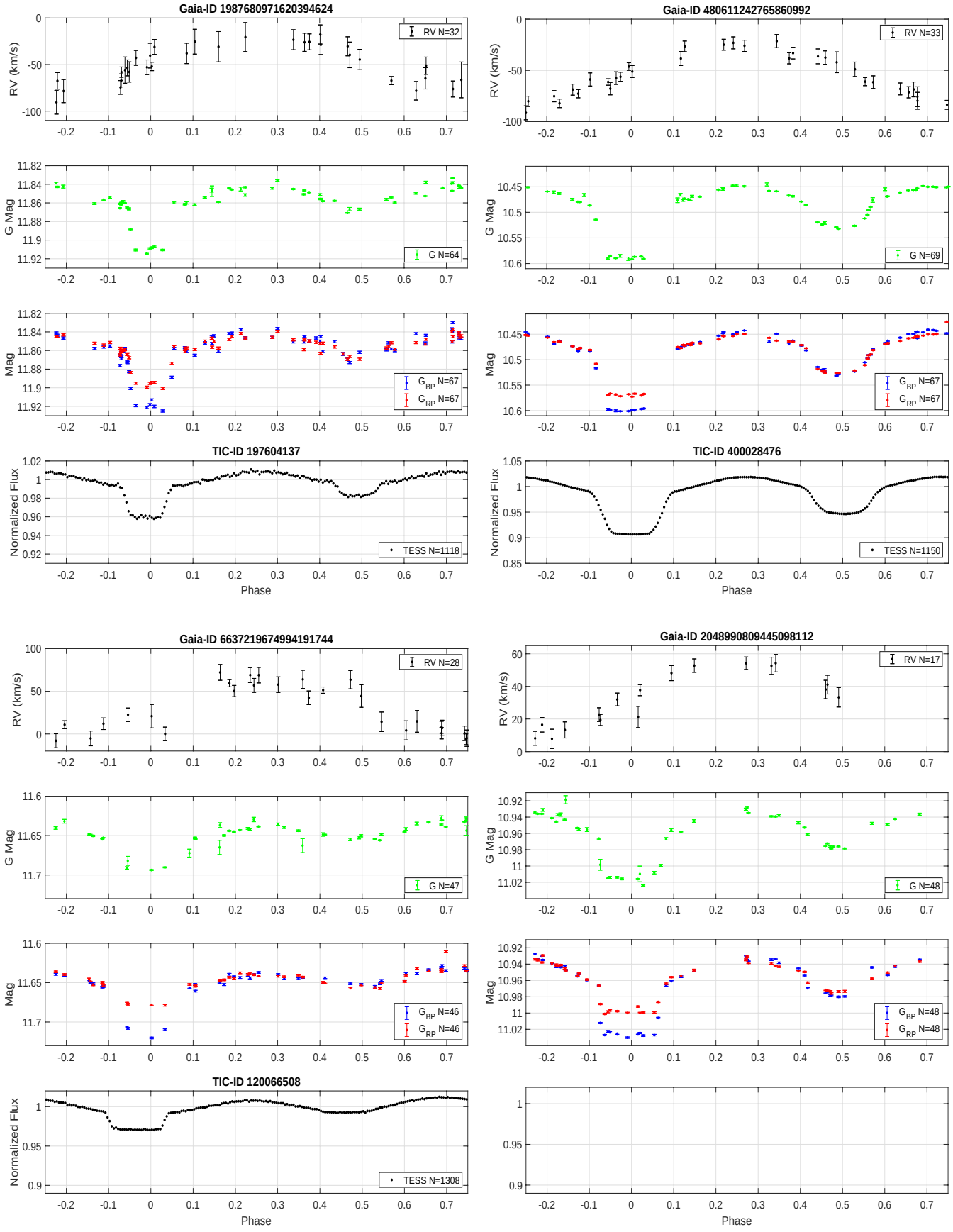

Fig. 30. *Gaia* and TESS data of four new EL CVn candidates using Fig. 28 presentation. We could not find TESS photometry for *Gaia* DR3 2048990809445098112, so its TESS panel was left empty.

Table 7. Parameters of 5 EL CVn candidate systems.

Gaia ID	5087757377681887232	1987680971620394624	480611242765860992	6637219674994191744	2048990809445098112
TIC ID	121078334	197604137	400028476	120066508	378080617
Other ID	HD 23692	TYC 3615-2289-1	TYC 4106-576-1	TYC 8757-1969-1	TYC 3135-13-1
GSP-Phot $T_{\rm eff}$ (K)	7360	7504	7470	NA	7148
GSP-Phot log g (dex)	$3.98^{0.05}_{0.03}$	$4.01^{0.01}_{0.03}$	$4.08^{0.005}_{0.004}$	NA	$3.77^{0.03}_{0.01}$
Parallax (mas)	3.447 ± 0.063	1.169 ± 0.012	2.647 ± 0.013	1.197 ± 0.020	1.251 ± 0.013
Radius `FLAME` ($R_\odot$)	$1.975^{0.053}_{0.050}$	$2.132^{0.047}_{0.047}$	$1.803^{0.037}_{0.038}$	NA	$3.006^{0.067}_{0.067}$
$G/G_{\rm BP}/G_{\rm RP}$ (mag)	9.56 / 9.70 / 9.29	11.86 / 12.05 / 11.52	10.47 / 10.65 / 10.16	11.64 / 11.86 / 11.28	10.95 / 11.13 / 10.64
RV/$G/G_{\rm BP}/G_{\rm RP}$ points	18 / 55 / 55 / 54	32 / 64 / 67 / 67	33 / 69 / 67 / 67	28 / 47 / 46 / 46	17 / 48 / 48 / 48
EB period (day)	0.92859504 ± 0.00001141	1.16189659 ± 0.00002522	0.64410724 ± 0.00000429	1.27337301 ± 0.00005718	1.36819733 ± 0.00005130
EB T_0 (BJD)	2457389.055 ± 0.004	2457389.680 ± 0.013	2457388.877 ± 0.003	2457389.784 ± 0.019	2457388.853 ± 0.010
SB1 K_1 (km s^{-1})	24.28 ± 0.94	30.42 ± 3.57	28.72 ± 1.47	32.28 ± 1.77	22.28 ± 1.67

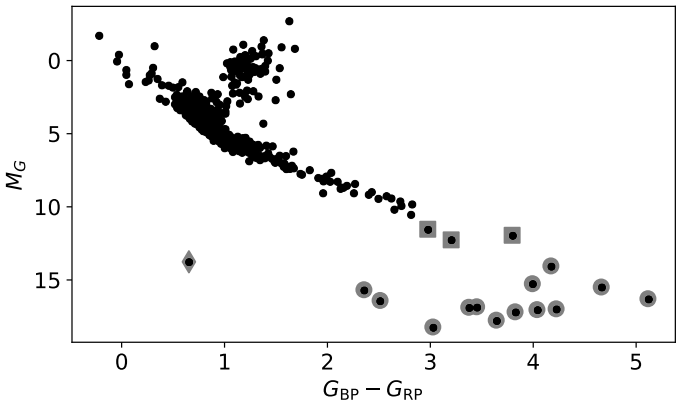

Fig. 31. Colour-magnitude diagram of 533 sources with `OrbitalTargetedSearch*` solutions (black circles). The larger grey circles indicate sources that are listed in the *Gaia* Ultra-cool Dwarf Sample (Smart et al. 2019), the grey squares indicate red sources discussed in the text, and the diamond indicates the white dwarf discussed in Sect. 8.8.

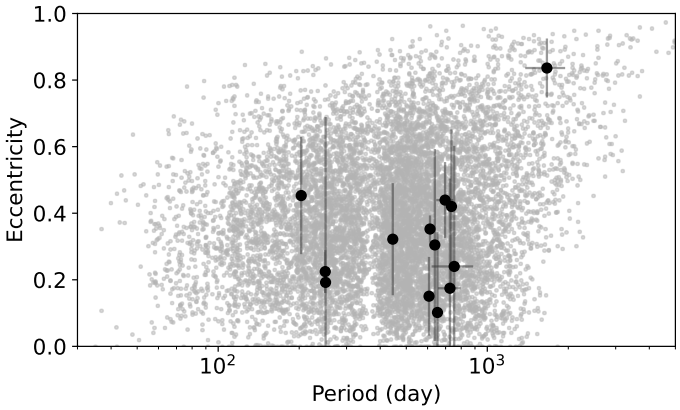

Fig. 32. Orbital eccentricity as a function of period for the UCD systems listed in Table 8 (black symbols). The parameters of `Orbital` solutions within 200 pc are shown in grey.

full GUCD sample was however included in the targeted search for orbital signals.

Thirteen sources with DR3 orbits are part of the GUCD catalogue, and only 5 of those are brighter than $G = 19$. Table 8 lists the GUCD sources with DR3 orbital solutions.

There are three binaries with previously published astrometric orbit solutions. These are J0805+4812 (Sahlmann et al. 2020), J0823-4912 (Sahlmann et al. 2013, 2015), and J1610-0040 (Dahn et al. 2008; Koren et al. 2016). Generally, the DR3 orbit parameters agree with these published solutions.

The J0320-0446 binary has a published RV orbit and both the *Gaia* period and eccentricity agree well. The *Gaia* solution indicates an almost edge-on configuration, in agreement with the expectations from the RV modelling by Blake et al. (2008). The Thiele-Innes coefficients for this low-eccentricity solution are highly correlated, which leads to correlated and skewed distributions when resampling the geometric parameters. This has to be accounted for when using the *Gaia* solution parameters for estimating the companion mass in particular.

Two sources in this list have only been identified as spectral binaries, i.e. typically L+T-dwarf systems in which the companion's spectrum is discernible in the combined-light near-infrared spectrum. In principle, the *Gaia* orbital solutions will make it possible to constrain the masses of the binary components. Since the orbital parameters refer to the system's photocentre, however, the applicable constraints depend on the brightness- and mass-ratio of the system which usually are not determined by *Gaia*. Therefore, external information and assumptions have to be incorporated. As an example, we explore the orbit of J2026-2943, which has previously been identified as a spectral binary with components of spectral types L1+T6 (Bardalez Gagliuffi et al. 2014; Gelino & Burgasser 2010). If we assume a field-age mass of $0.080 \pm 0.005\,\mathcal{M}_\odot$ for the L1 primary and that the light contribution of the T6 companion is negligible in the G band, then the *Gaia* orbit solution implies a companion mass of $0.041^{+0.016}_{-0.009}\,\mathcal{M}_\odot$, where we accounted for all parameter covariances using Monte-Carlo resampling. This mass estimate is compatible with expectations for a T6 brown dwarf and adds a valuable entry in the list of low-mass systems with dynamically-determined masses (Dupuy et al. 2019; Sahlmann et al. 2020). Examples of combining astrometric orbit solutions with RVs, spectral-binary indicators, and spatially-resolved observations to investigate the physics of UCDs can be found in the literature (e.g. Garcia et al. 2017; Sahlmann et al. 2021, 2020; Brandt et al. 2020).

For the remaining 7 sources we have not found previously-identified multiplicity indicators in the literature. These are therefore potentially new UCD binary discoveries made in *Gaia* DR3. These could be confirmed by independent observations of their spectroscopic properties or with RV monitoring. Because of its long period and proximity, the J0031-3840 system has an estimated relative semi-major axis of ~60 mas and could possibly be spatially resolved with specialised instruments, which can give access to model-independent mass determinations.

As expected, the UCD binaries discussed above are compact systems with estimated relative separations $\lesssim$1.5 au because a large fraction of their orbits is covered by the DR3 data. Their

Table 8. Identifiers and basic properties of 13 UCD binaries in DR3. The 'Name' column corresponds to the SHORTNAME in the GUCD catalogue. The uncertainties of a_0 were computed using linear error propagation. The three additional sources at the bottom of the table are the reddest `OrbitalTargetedSearch` sources at the bottom of the main sequence that are not in the GUCD catalogue.

Gaia DR3	Name	`nss_solution_type`	Period (d)	a_0 (mas)	Notes
4997505546262260096	J0031-3840	OrbitalTargetedSearch	1665.4 ± 281.5	23.96 ± 3.47	New binary candidate
2576389458819793920	J0106+0557	OrbitalTargetedSearch	726.2 ± 71.0	4.48 ± 0.60	New binary candidate
5182151481717042944	J0320-0446	OrbitalTargetedSearch	250.6 ± 1.7	7.75 ± 2.76	Known RV binary[d]
3269943938874146688	J0344+0111	OrbitalTargetedSearch	652.9 ± 23.4	7.55 ± 0.42	Known spectral binary[e]
144711230753602048	J0435+2115	OrbitalTargetedSearch	607.4 ± 25.2	5.48 ± 0.34	New binary candidate
3361210791323909504	J0659+1717	OrbitalTargetedSearch	753.6 ± 132.8	7.90 ± 1.55	New binary candidate
933054951834436352	J0805+4812	OrbitalTargetedSearchValidated	735.9 ± 23.0	14.18 ± 2.06	Known astrometric binary[a]
5514929155583865216	J0823-4912	OrbitalTargetedSearchValidated	250.0 ± 1.2	4.99 ± 0.21	Known astrometric binary[b]
1610979010812148224	J1429+5730	OrbitalTargetedSearch	445.4 ± 8.5	4.64 ± 0.46	New binary candidate
4406489184157821952	J1610-0040	OrbitalTargetedSearch	612.5 ± 7.7	9.41 ± 0.25	Known astrometric binary[c]
6797628972554531840	J2026-2943	OrbitalTargetedSearch	638.3 ± 14.5	5.69 ± 1.05	Known spectral binary[f]
1754495583527340416	J2036+1051	OrbitalTargetedSearch	696.7 ± 50.4	4.57 ± 0.53	New binary candidate
6616442994033876480	J2200-3038A	OrbitalTargetedSearch	203.5 ± 1.9	3.84 ± 0.68	New binary candidate[g]
4963614887043956096	J0219-3925	OrbitalTargetedSearch	538.0 ± 3.0	1.41 ± 0.05	New binary candidate[h]
43574131143039104	LHS1610	OrbitalTargetedSearch	10.6 ± 0.0	1.39 ± 0.04	Known RV binary[i]
5600272625752039296	L 601-78 A	OrbitalTargetedSearch	14.3 ± 0.0	1.87 ± 0.07	New binary candidate

Notes. References: [(a)] Sahlmann et al. (2020) [(b)] Sahlmann et al. (2013) [(c)] Dahn et al. (2008) [(d)] Blake et al. (2008) [(e)] Bardalez Gagliuffi et al. (2014) [(f)] Bardalez Gagliuffi et al. (2014); Gelino & Burgasser (2010) [(g)] This would be a new inner binary as component A in a known 1″-wide binary (Burgasser & McElwain 2006; Smart et al. 2019) [(h)] This would be a new inner binary in a known 4″-wide binary (Artigau et al. 2015) [(i)] Winters et al. (2018)

period-eccentricity distribution is essentially unaffected by the complications in terms of mass determination discussed above and can be used to investigate UCD formation mechanisms or dynamical histories (e.g. Dupuy & Liu 2011). Figure 32 shows these parameters in comparison with the `Orbital` solutions. The high eccentricity of the long-period solution for J0031-3840 may be affected by the incomplete orbit-coverage with *Gaia* data, which tends to push eccentricity up as also shown by the `Orbital` solutions.

Comparison with Dupuy & Liu (2017, Fig. 18, which includes a few sources in common) shows that these generally intermediate eccentricities are in agreement. Importantly, *Gaia* is filling in the period-range of $\sim$ 0.5 − 5 years which so far is sparsely populated because of the resolution-limit of direct-imaging instruments. This will help to build statistically-robust samples of UCD binaries that can be used for comparison to stellar binaries.

Finally, we inspected the orbits of the three reddest objects that are not in the GUCD catalogue, which are highlighted with squares in Fig. 31:

J0219-3925 This is 2MASS J02192210-3925225, which was characterized as a young late-M dwarf with a wide (4″) substellar companion by Artigau et al. (2015). The *Gaia* astrometric orbit corresponds to an inner companion to the M-dwarf, which (if dark) could have a mass as low as $11.2 \pm 0.9\,\mathcal{M}_{\rm Jup}$ for the primary mass of $113 \pm 12\,\mathcal{M}_{\rm Jup}$ (Artigau et al. 2015). Another possible explanation is a more massive companion, whose light contribution dilutes the photocentre orbit. Auxiliary data or observations have to be considered to better characterise the inner companion.

LHS1610 This mid-M dwarf was identified as an RV binary by Winters et al. (2018) and the *Gaia* astrometry independently confirms the eccentric 10.6 day orbit. The Gaia solution indicates a close-to edge-on configuration and a companion-mass estimate of $0.052^{+0.004}_{-0.004}\,\mathcal{M}_\odot$ when assuming a primary mass of $0.17 \pm 0.02\,\mathcal{M}_\odot$, i.e. it establishes the substellar nature of the companion.

L 601-78 A This is the primary component of the wide binary L 601-78. It was identified as a lens candidate for mass determination using astrometric microlensing by *Gaia* (Klüter et al. 2020).

7. Compact-object companions

In what follows we point out a few channels of identifying binary candidates in our tables that might harbour compact-object companions. The discussion is meant to suggest further study that is needed in order to confirm the nature of these binaries. We first underline the method used for astrometric orbits, then discuss white dwarf secondaries, then larger masses, including those found using SB1 orbits.

7.1. Astrometric binaries with compact-object companions using the triage algorithm

To identify unresolved astrometric binaries that are likely to host a compact object as their faint binary companion, we use the triage classification of Shahaf et al. (2019). The algorithm divides the astrometric binaries into three classes:

- class-I binaries, where the companion is most likely a single MS star (but can also be a close binary or a compact object),
- class-II binaries, where the companion cannot be a single MS star; therefore, it is most likely a close MS binary (but can also be a compact object), and
- class-III binaries, where the companion cannot be a single MS star or a close MS binary; therefore, these systems most likely host a compact object as secondary.

The distinction between the three classes depends on the value of the newly defined astrometric mass ratio function (AMRF), $\mathcal{A}$, given by

$$\mathcal{A} \equiv \frac{a_0}{\varpi}\left(\frac{\mathcal{M}_1}{\mathcal{M}_\odot}\right)^{-1/3}\left(\frac{P}{\rm yr}\right)^{-2/3}, \quad (9)$$

where a_0 is the derived angular semi-major axis of the photocentric orbit, ϖ is the parallax, $\mathcal{M}_1$ is the mass of the primary star, and P is the orbital period of the binary.

AMRF, $\mathcal{A}$, can be written as a function of the mass ratio $q = \mathcal{M}_2/\mathcal{M}_1$ and the luminosity ratio of the two components of the astrometric binary $\mathcal{S} = F_2/F_1$ as

$$\mathcal{A} = \frac{q}{(1+q)^{2/3}}\left(1 - \frac{\mathcal{S}(1+q)}{q(1+\mathcal{S})}\right), \quad (10)$$

(see details in Shahaf et al. 2019). The luminosity ratio modelling is based on the Pecaut & Mamajek (2013) main-sequence colour and effective temperature tables, assuming no extinction. As emphasized by Shahaf et al. (2019), there are two limiting AMRF values: the maximal value for a single MS companion (class I sources), and the maximal value assuming a close binary of two identical MS stars as the secondary companion (class II sources).

Figure 33 presents the derived AMRF values for the *Gaia* unresolved astrometric binaries presented in this work, with primaries in the range of 0.2−2.0 $\mathcal{M}_\odot$ and significance larger than 20, using the primary mass values reported in Table 3. Systems with AMRF values that exceed the maximal possible value for triple stars by more than 4σ, where the uncertainty σ was calculated by propagating the uncertainties of the quantities in Eq. (9). They are presented in Fig. 33 as bold black points and are likely to host a compact-object companion. Since the light contribution of the companions of these systems is negligible, namely $\mathcal{S}\simeq 0$, we can derive the mass ratio and then the mass of the secondary of these systems. Their mass values are presented in the right panel of the figure.

We compare the obtained masses with the conservative lower-limit estimate of the companion mass (Sect. 5.1), in the left panel of Fig. 34. Additionally, because for faint companions the photocentre coincides with the position of the primary star, we expect the semi-major axes derived from the astrometry and the RV spectroscopy to be similar, as demonstrated in the right panel of Fig. 34 for the `AstroSpectroSB1` cases.

Figure 36 presents a mass histogram of the secondaries of the astrometric binaries assumed to have a compact companion, up to 2.1 $\mathcal{M}_\odot$. It seems as if most of the companions are white dwarfs, with a clear narrow peak at $\sim 0.6\,\mathcal{M}_\odot$, as is the case for field white dwarfs. Obviously, the secondary mass population is heavily biased by the way it was derived, so any astrophysical interpretation should be done carefully. Anyway, the circularisation at large periods is striking, Fig. 37.

The histogram of secondary masses, Fig. 36 has been limited to 2 $\mathcal{M}_\odot$. There are however 4 sources with a larger mass (identified as `AMRFClassIII` in the table), but we have indications that they may be artefacts.

7.2. A closer look at the astrometric binaries with white-dwarf companions

White dwarfs are often present in binary systems. The co-eval context with their companion star makes such systems important benchmarks for understanding stellar evolution. WDs in wide systems can be detected relatively easily through searches for common proper motion objects (e.g. El-Badry & Rix 2018). However, in closer systems the WD can be very difficult to detect due to the overwhelming brightness of the companion, particularly for early spectral types. In that case, the WD may be hidden until revealed by astrometric motion, spectroscopic variability or a photometric excess. A classic example is the discovery of Sirius B (Bessel 1844), which is both an astrometric and spectroscopic binary (e.g. Barstow et al. 2005; Bond et al. 2017). Sirius represents a class of binary systems, the Sirius-type binaries, consisting of a primary star of spectral type earlier than late-K and a WD. Examples of such systems have often been identified by flux excesses at wavelengths shorter than those spanned by the primary, in the UV, EUV or X-ray (see e.g. Barstow et al. 1994). A fraction have subsequently been resolved by space-based observations (e.g. Barstow et al. 2001).

The number of Sirius-type binaries known lies in the 10s of objects, with selection effects playing a strong role in identification of an individual system. For example, unless resolved, the flux of any cool white dwarf will always be buried in the light of the primary companion. Whether or not a system can be resolved depends on the separation and distance of the components. Binary systems comprising 2 WDs (double degenerates) or a WD with an M dwarf companion are easier to find as they will sit closer to the main WD cooling tracks in the H-R diagram. Even so, the nature of any double degenerates might not be apparent if the stars have similar or featureless spectra. The SPY survey sought to identify double degenerates from radial velocity variations finding 39 double degenerate systems and 46 WDs with cool companions from a sample of 643 stars (Napiwotzki et al. 2020).

The *Gaia* stellar catalogue is an enormous resource that will potentially increase the number of known binary systems with WD components by at least an order of magnitude. In *Gaia* DR2 and *Gaia* EDR3 the number of known WDs expanded by such a factor (Gentile Fusillo et al. 2019, 2021). While many WD+M systems can by identified by their location in the HRD, double degenerates will typically overlap strongly with the isolated WD cooling tracks and Sirius-like systems largely overlap with the main sequence. The release of eclipse, astrometry and spectroscopy data related to the identification of NSS in *Gaia* DR3 is an important step forward. In principle, these new resources can be used to search for the presence of WDs in a variety of binary systems.

7.2.1. Selection of candidate binary systems with WD components

The wavelength coverage of the *Gaia* Radial Velocity Spectrometer is not optimised for the study of WDs, which typically have broad absorption lines in their photospheres, when any are present. Therefore, we would expect only the primary stars in Sirius-like binaries will be detected as radial velocity variables. Hence, they will most likely be found in the sample of `SB1` systems. If the secondary is a WD, it will not contribute significantly to the brightness of the system in the *Gaia* bands. However, if hot enough, there may be a measurable excess at shorter wavelengths. In addition, the secondary mass will lie between $\approx 0.4 - 1.4\,\mathcal{M}_\odot$, where the Chandrasekhar limit defines the upper bound.

Binaries with WD components might also be detected astrometrically or as eclipsing binaries. Therefore, we have assembled an initial list of potential candidate binary systems with WD components from the non-single stars, selected for all these possibilities, using the following `nss_solution_type` keywords: `AstroSpectroSB1`, `SB1C`, `SB1`, `Orbital`, `OrbitalAlternative`, `Eclipsing*`, `OrbitalTargetedSearch`. Effectively, this is all non-single star systems except for SB2 binaries. We did not apply any quality selection criteria except to reject any objects with G greater than 20. This selection yielded a total of 355 524 non-single stars for further analysis. The AMRF sample, based on `AstroSpectroSB1` and `Orbital` solutions alone, is a subset of

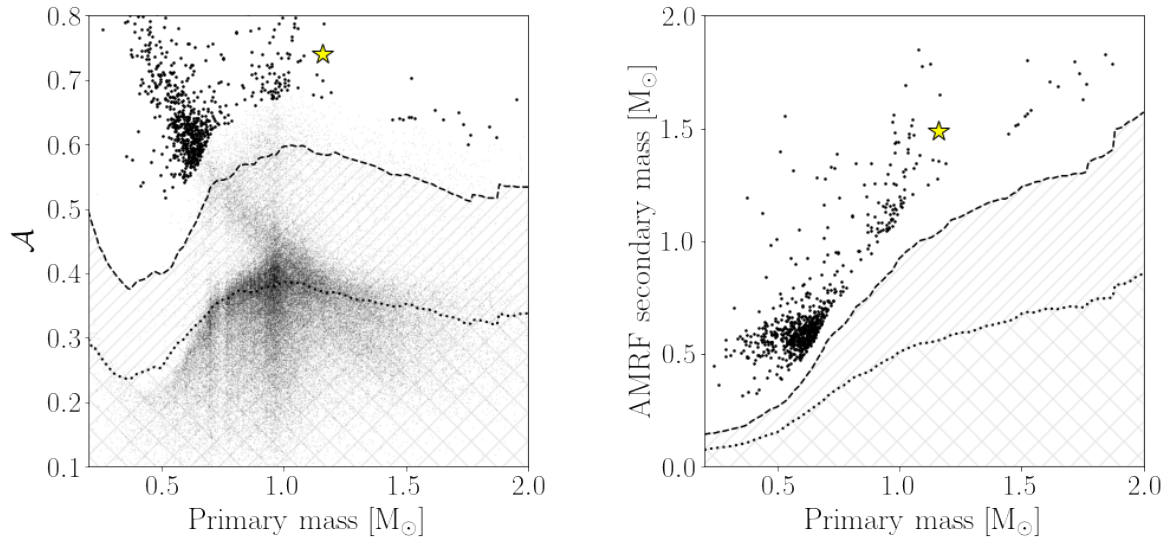

Fig. 33. Triage of the *Gaia* astrometric binaries, with classes I to III from bottom to top delineated by dotted and dashed lines respectively. *Left*: AMRF vs. mass of the primary for the astrometric solutions of this paper. The systems with a probable compact-object companion (class III) are presented as bold black points (see text). For reference, the rest of the sample is plotted as thin black points. *Right*: Masses of the compact companions, derived from the AMRF, as a function of their primary mass. The rest of the systems do not appear in this panel. Yellow star is the neutron star candidate *Gaia* DR3 5136025521527939072 discussed in Sect. 7.3.

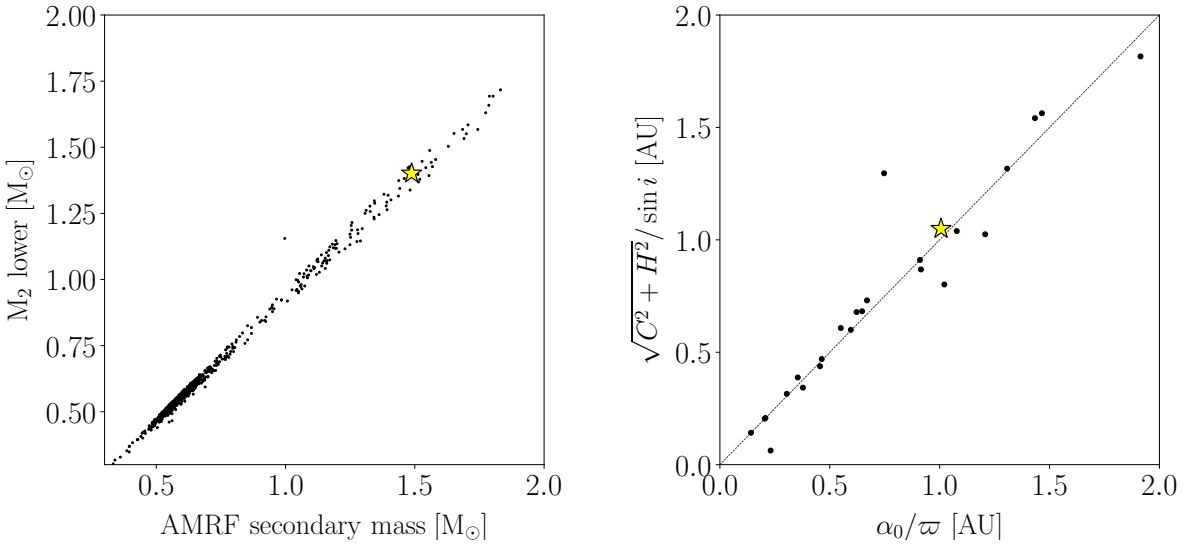

Fig. 34. *Left*: Comparison between the minimum companion mass, derived in Sect. 5.1, and the AMRF-derived masses for the compact-object candidates. The sources where the AMRF mass is smaller than the minimum mass are `AstroSpectroSB1` with actually a non-negligeable flux ratio. *Right*: Comparison between semi-major axes derived for the `AstroSpectroSB1` systems using the astrometric parameters (horizontal axis) and the spectroscopic parameters (vertical axis). Yellow star is the *Gaia* DR3 5136025521527939072.

these candidates for which we have good estimates of the component masses.

In the search for WD companions, we use the AMRF data to restrict the mass range of compact objects to lie below the 1.4 $\mathcal{M}_\odot$ Chandrasekhar limit. Applying this criterion yields 676 objects which are shown in green in Fig. 38 and compared to the locus of the GCNS (grey data points). The secondary mass alone cannot be used to definitively determine that these are WD components, as F, G, K and the earliest M main sequence stars also occupy this mass range. However, several factors indicate that these objects are highly likely to be Sirius-type binaries. Any unresolved main sequence binaries should appear to be over luminous. Evolution on the main sequence and the range of possible luminosity combinations may prevent a clear separation of binaries and isolated stars, but unresolved main sequence binaries should appear as SB2 systems in the non-single star *Gaia* catalogue. Finally, as noted above, the mass distribution for the secondaries in these unresolved astrometric binaries has a strong

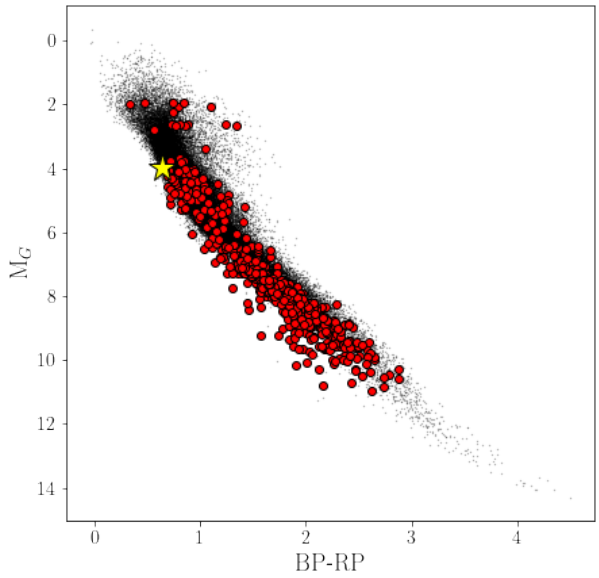

Fig. 35. Class-III CMD. Black points - Orbital and AstroSpectro, for reference. Red points are AMRF class-III. The yellow star is *Gaia* DR3 5136025521527939072.

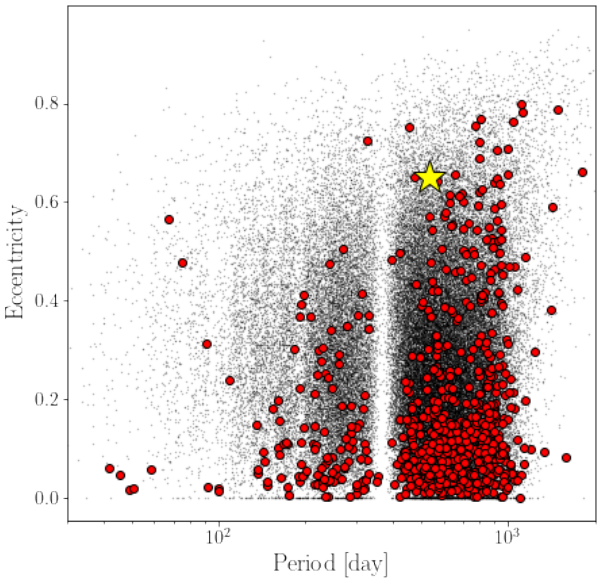

Fig. 37. *e* - *P* diagram. Black points - `Orbital` and `AstroSpectro`, for reference. Red points are AMRF class-III. Yellow star is the *Gaia* DR3 5136025521527939072.

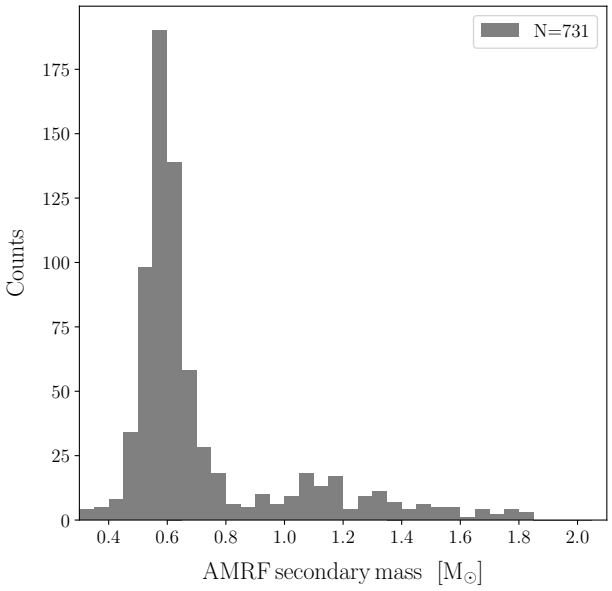

Fig. 36. A histogram of the companion masses for compact object candidates, up to a mass of 2.1 $\mathcal{M}_\odot$.

peak at 0.55-0.6 $\mathcal{M}_\odot$, corresponding to the known peak of the mass distribution of field WDs (Fig. 36). This is in contrast to the smooth mass distribution expected for main sequence stars.

While the vast majority of selected objects lie on the main sequence, as shown in Fig. 38, there are 39 objects that match WD colours and magnitudes, indicating a WD primary, shown in Fig. 39. The majority of these objects lie above the main concentration of the isolated white dwarfs. Therefore, these systems are highly likely to be double degenerates, where the brightness of two unresolved combines to yield an apparent excess in luminosity.

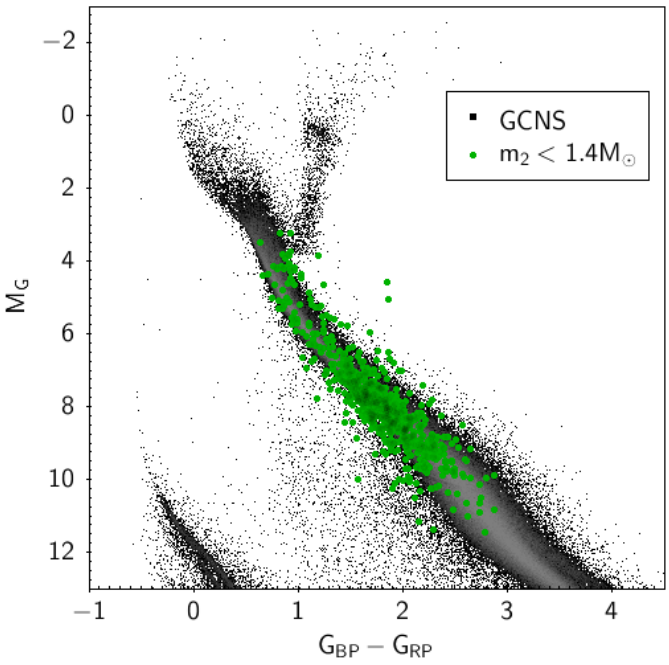

Fig. 38. H-R diagram of the candidate non-single stars with WD components with a secondary mass solution below the Chandrasekhar limit ($< 1.4\,\mathcal{M}_\odot$, green data points). These are compared with the locus of stars in the GCNS (grey data points).

As discussed above, when we know the secondary mass and the binary is not revealed as an SB2 system, we can be very

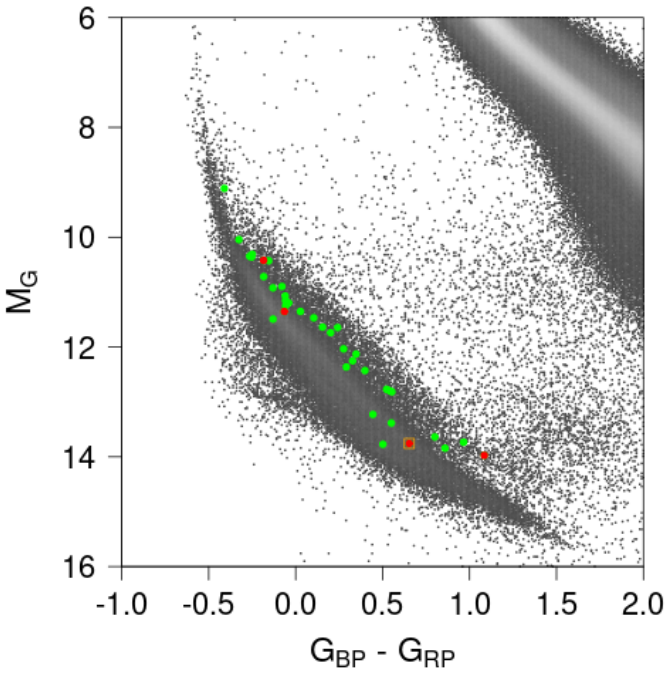

Fig. 39. WD with orbital solutions (green points, corrected from extinction) overplotted on the *Gaia* DR3 low extinction HRD. Most of the points lie above the hydrogren sequence. The red dots and WD 0141-675 (orange square) are discussed Sect. 8.8.

confident that the secondary is a WD and, therefore, the binary a Sirius-type system. However, it is likely that there are many more Sirius-type systems in the non-SB2 sample. An unresolved binary system can be revealed by a flux excess in a waveband where the contribution from the primary star is expected to be weak. A number of Sirius-type binary discoveries have been made by detecting the WD in the EUV or UV wavebands. The GALEX mission surveyed most of the sky in two broad FUV and NUV bands. Cross-correlating the GALEX data base with the *Gaia* DR3 non-SB2 binaries will potentially reveal the Sirius-type systems with a hot WD component. This is illustrated by applying this to the astrometric binaries in the sample. Fig. 40 and Fig. 41 show the G vs $G_{BP}-G_{RP}$ H-R diagram for the cross-match of the GALEX GR6+7 AIS catalogue with this sample for NUV and FUV bands respectively. The small grey data points are the GCNS stars in each figure while the coloured symbols are the NUV (Fig. 40) and FUV detections (Fig. 41), colour-coded by the absolute NUV or FUV magnitude, as indicated in the side bar. These magnitude ranges can be compared to the typical values for white dwarfs in the optical colour/absolute magnitude diagram, as indicated in Fig. 39. The absolute NUV magnitude correlates well with the $G_{BP}-G_{RP}$ colour, an indicator of the temperature of the primary star. However, a few systems show a strong NUV excess for the systems with cooler main sequence primaries, indicated by red to yellow colours compared to green to blue in that region of the diagram. Hence, the integrated NUV flux is not generally a good indicator of the presence of the white dwarf. In contrast, there is little, if any, correlation between the absolute FUV magnitude and $G_{BP}-G_{RP}$ colour, indicating that the FUV is a better discriminator than the NUV, the measured magnitudes potentially providing an estimate of the WD temperature. However, this can only be applied to the relatively few stars that are sufficiently hot to have a measurable FUV flux. We note that the FUV magnitude is a not a completely unique indicator of the presence of a WD, as coronally active main sequence stars can also generate an enhancement in the total FUV flux through the strong C IV (154.8nm & 155.0nm) and He II (164nm) emission lines.

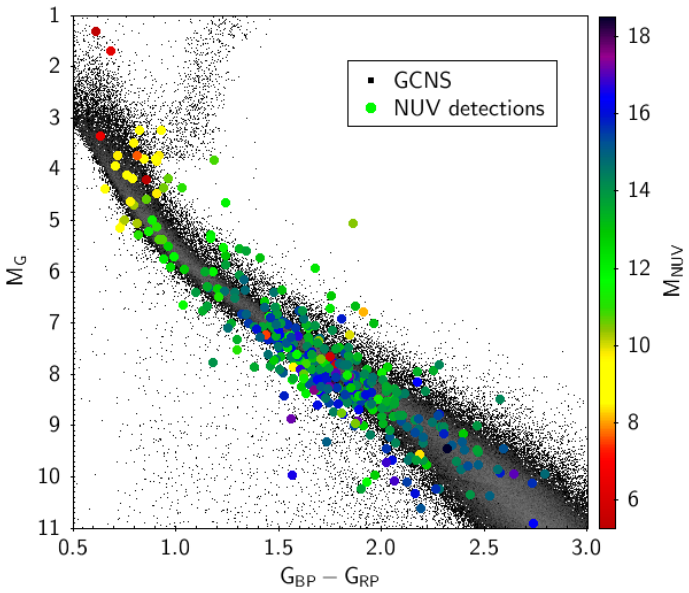

Fig. 40. G vs $G_{BP}-G_{RP}$ H-R diagram showing the cross-match between the GALEX GR6+7 AIS catalogue with the GCNS (small symbols) and the candidate list of binaries with WD components with computed secondary star masses below the Chandrasekhar limit ($< 1.4\,\mathcal{M}_\odot$). The symbols are colour coded with the absolute NUV magnitude as indicated by the side-bar.

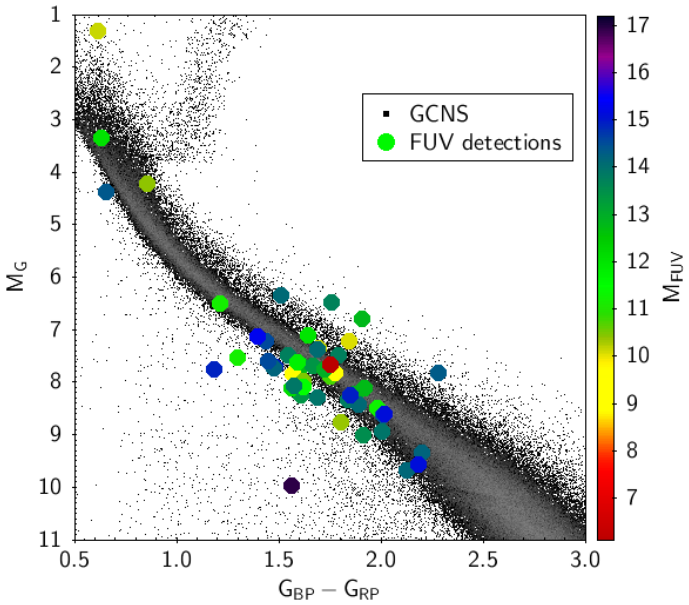

Fig. 41. G vs $G_{BP}-G_{RP}$ H-R diagram showing the cross-match between the GALEX GR6+7 AIS catalogue with the GCNS (small symbols) and the candidate list of binaries with WD components with computed secondary star masses below the Chandrasekhar limit ($< 1.4\,\mathcal{M}_\odot$). The symbols are colour coded with the absolute FUV magnitude as indicated by the side-bar.

We also cross-matched the full *Gaia* DR3 non-SB2 binaries with the GALEX GR6+7 AIS catalogue. The results are shown in Fig. 42, with 29 000 stars of the list of 355 000 objects having a GALEX FUV counterpart. The FUV detections in the WD

region of the H-R diagram provide an indication of the range of FUV absolute magnitudes, between $\approx 8-20$, that correspond to WDs. Many of the FUV counterparts in Fig. 42 have similar magnitudes, but without further information it is not possible to categorically identify these as WDs and rule out alternative explanations for the FUV flux.

A more detailed modelling of the predicted primary and WD fluxes across the expected range of temperatures should be able to refine the discriminatory power of this approach to selecting Sirius-type systems, but that is beyond the scope of this *Gaia* DR3 companion paper.

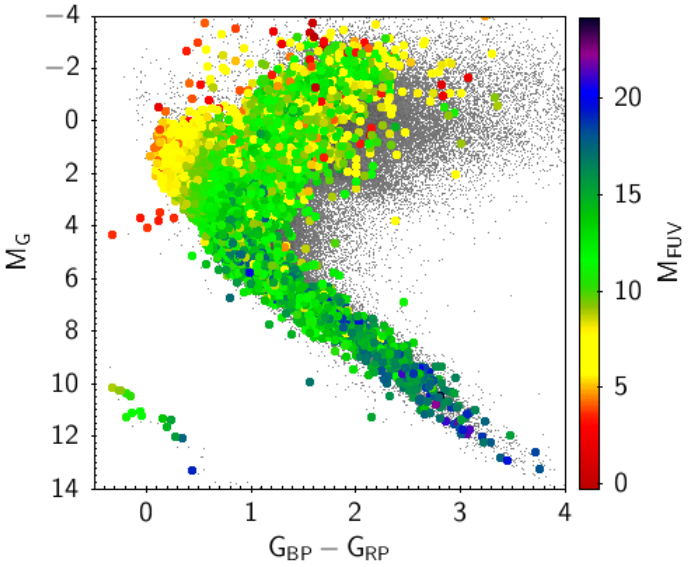

Fig. 42. G vs $G_{BP}-G_{RP}$ H-R diagram showing the cross-match between the GALEX GR6+7 AIS catalogue with the full list of non-SB2 binaries selected here (large symbols). The symbols are colour coded with the absolute FUV magnitude as indicated by the side-bar. The small grey data points are the full list of non-SB2 binaries.

7.3. A binary with a dormant neutron star with an AstroSpectroSB1 orbit?

Only a few tens of dynamically confirmed Galactic stellar black holes (BH) and neutron stars (NS) are known to reside in binary systems. They are discovered either by their X-ray emission, fueled by mass transfer from their non-compact stellar companions (e.g., Fabian et al. 1989; Remillard & McClintock 2006; Orosz et al. 2007; Ziolkowski 2014), or, in the case of active pulsars, by their radio pulsed emission.

Obviously, most BH in binaries were not detected yet, because their optical counterparts are well within their Roche lobes, so mass is not transferred and X-rays are not generated, making these systems dormant (see discussion on the frequency of such systems and the prospect of their detection with *Gaia* astrometry by Breivik et al. 2017; Mashian & Loeb 2017; Shao & Li 2019; Wiktorowicz et al. 2019). Similar arguments apply to dormant NS — the pulsation phase lasts for 10–100 million years only, when the pulsar is young (Faucher-Giguère & Kaspi 2006; Bransgrove et al. 2018) — and to binaries with white-dwarf (WD) companions (see discussion above). Such dormant binaries can be found by the orbital motion of the primary, detected either by astrometry or RVs. In all three classes of dormant companions, the challenge is to identify the binaries, estimate the mass of the unseen companion, and rule out a faint MS companion.

One of the systems identified by the triage algorithm as having a compact companion, *Gaia* DR3 5136025521527939072, is in fact an AstroSpectroSB1 binary, with a primary mass of 1.2 $\mathcal{M}_\odot$ and secondary mass of 1.5 $\mathcal{M}_\odot$, consistent with a binary having a dormant neutron star with a period of 536 days. Its location is marked in the pertinent figures of the triage analysis above.

The astrometric orbit and the phase-folded radial velocity of this source are shown in Figure 43[16]. In order to validate the orbit, we have required observing time on the Sophie spectrograph, mounted at the 1.93-meter telescope of the Observatoire de Haute-Provence (France). The Sophie pipeline (Bouchy et al. 2009) together with a G2 mask was used and we obtained a RV= 40.603 ± 0.023 km s^{-1} with a FWHM = 9.274 km s^{-1} on BJD 2459541.389492. The consistency of this RV obtained about 4.5 years after the end of the Gaia data segment used for *Gaia* DR3 confirms the quality of the predicted orbit.

7.4. Compact objects in SB1 solutions

While the search for compact object companions above had been done using the astrometric orbits, we complete the search using the SB1 solution.

The search of SB1 sources with large mass functions have been proposed since several decades as a way to identify candidates having a black hole or neutron star companion (Trimble & Thorne 1969; Guseinov & Zel'dovich 1966). Among the SB1 sources 94 have significance larger than 20 and $f(\mathcal{M}) > 1.4\,\mathcal{M}_\odot$, and 20 among them $f(\mathcal{M}) > 3\,\mathcal{M}_\odot$. The SB1 solution of *Gaia* DR3 2006840790676091776 shall be dismissed due to contamination by a nearby bright source. The inspection of RVS spectra of *Gaia* DR3 5259215388421037696 shows that the source is probably an SB2 and the radial velocities, computed with an incorrect template, are most probably not correct, so the SB1 solution of this star shall be discharged. *Gaia* DR3 878555832642451968 has a RV measurement in the LAMOST (Luo et al. 2015) survey (–100.86 km s^{-1} at BJD 2458068.5) which does not agree with the SB1 solution. A reanalysis of the RVS epoch RV shows that an alternative solution with a period of 8.438 days is also possible and in better agreement with LAMOST data. So the SB1 solution in the *Gaia* archive should be considered as dubious. In Fig. 44 we show the position of the sources with $f(\mathcal{M}) > 1.4\,\mathcal{M}_\odot$ in the color-magnitude diagram. The relevant data of the sources with $f(\mathcal{M}) > 3\,\mathcal{M}_\odot$ are reported in Table 9.

From Fig. 44, we can see that, with few exceptions, all the selected sources are not main sequence stars. It is thus challenging to determine the real nature of these systems because, if the primary is a giant star, it can easily outshine a companion on the main sequence. In some cases the secondary, even being on the main sequence, can be more massive than the primary, via mass transfer as in Algol-type systems (see El-Badry et al. 2022, for recent examples of black hole candidates dismissed as main sequence companions of stripped stars). We recall that such systems are much more common objects than dormant black holes. Another possible explanation for such large mass function values is that the unseen companion is itself a binary composed by

[16] The astrometric orbit figure was obtained on the basis of the pystrometry package (https://github.com/Johannes-Sahlmann/pystrometry, Sahlmann 2019). Other examples and a description are given in Holl et al. (2022b).

Table 9. SB1 solutions with $f(\mathcal{M}) > 3\,\mathcal{M}_\odot$. The radii R are from GSP-Phot or FLAME when available.

Gaia DR3	$f(\mathcal{M})$ ($\mathcal{M}_\odot$)	Period (days)	$a_1 \sin i$ ($R_\odot$)	R ($R_\odot$)	M_G	$G_{BP} - G_{RP}$
4661290764764683776[a]	13.67	204.930±0.862	349.49	60.52	-6.707	0.474
5863544023161862144[b]	7.80	10.605±0.001	40.25		-1.531	1.783
4429923114185936664[c]	4.77	216.531±1.463	255.33	20.16	-1.592	0.862
2062927467245898 24[d]	4.53	347.002±0.364	343.50	42.25	-2.741	2.067
5857059996952633984[e]	4.25	155.085±0.228	196.63	7.42[h]	-0.893	0.684
2174777963318889344	3.83	82.723±0.158	124.88	34.82	-1.970	2.021
2031113506311851904[f]	3.78	35.908±0.030	71.29		-0.145	1.736
1996704839648530816	3.75	7.54574±0.00077	25.13	7.29	-1.414	0.520
251157906379754496	3.62	296.676±2.176	287.10		-0.928	1.714
3331748140308820352	3.56	225.268±1.189	237.61		0.485	1.836
1828150428697001472	3.54	333.688±0.205	308.23		-3.716	1.583
3112097229257687680[g]	3.33	260.978±0.608	256.40	23.98[h]	-1.711	1.422
5963629779180627968	3.19	11.369±0.002	31.30	11.86[h]	0.922	2.078
5123074786424419 84[f]	3.14	145.578±0.074	170.44		-1.885	1.886
527155253604491392	3.13	149.155±0.318	173.06	12.15[h]	0.371	1.856
5869320651099982464[f]	3.09	63.924±0.011	97.95		-1.615	1.214
2929565719083290240	3.09	32.473±0.014	62.31	7.84[h]	0.484	1.237

Notes. [a] LHA 120-S 80: B8Ie (Rousseau et al. 1978) star in the LMC with emission lines. A distance of 49.59 kpc from Pietrzyński et al. (2019) was used to compute absolute magnitude M_G. [b] V878 Cen: eclipsing binary star classified as Hot semi-detached system (Avvakumova et al. 2013) with the same period, confirmed by *Gaia* photometry. [c] HIP 15429: B5Ib star (Navarro et al. 2012); belongs to PMa sample of Kervella et al. (2022). [d] EM* GGA 311: Emission-line Star (González & González 1956). [e] Classified as Algol type eclipsing binary from *Gaia* photometry with period of 1.17143 days. [f] *Gaia* light curve show ellipsoidal behavior. [g] EM* RJHA 92: Emission-line Star (Robertson & Jordan 1989). [h] Radius from FLAME.

two main sequence stars. The understanding of the nature of the other systems would need a deeper analysis using external data and follow-up observations, but such an analysis is beyond the scope of this paper. We can, however, comment on some of these objects. For *Gaia* DR3 5863544023161862144, the presence of eclipses allows to classify it as an Algol system and to exclude the compact object companion hypothesis. The *Gaia* photometry of the source *Gaia* DR3 5857059996952633984 shows a light curve with eclipses of Algol type, however with a period of 1.17143 days, typical of Algol systems, in contrast with the period from the SB1 solution. By analysing the epoch radial velocities and the epoch photometry, we can exclude an aliasing, in both the SB1 solution and the photometry. A possible solution is that this source is a triple system where the RV data are from the outer component, and the eclipses involve the two inner components.

A particularly interesting source is *Gaia* DR3 4429923114185936664 (HIP 15429), a B5Ib star (Navarro et al. 2012) with $f(\mathcal{M}) = 4.77\ \mathcal{M}_\odot$. In order to validate the orbit, this source was observed with the HERMES spectrograph mounted on the 1.2-meter Mercator telescope[17] (Raskin et al. 2011) at the Roque de los Muchachos Observatory on La Palma Island. A RV of -47.2 ± 3.5 km s^{-1} at BJD 2459650.358 was obtained, compatible with the Gaia SB1 solution. The HERMES spectrum also confirms the spectral classification of Navarro et al. (2012). Using the 3D extinction map of Lallement et al. (2019), we estimate a dereddened absolute magnitude and color, $M_{G,0} = -3.168$ and $G_{BP,0} - G_{RP,0} = 0.073$, respectively. Comparing these values with the PARSEC evolutionary tracks (Bressan et al. 2012) for solar metallicity, we can interpret this source as being a $4.9 \pm 0.3\,\mathcal{M}_\odot$ star, which just left the main sequence. The resulting minimum mass for the companion would be $10.4\,\mathcal{M}_\odot$. Under the hypothesis that this is a triple system, the secondary would then be a binary where at least one component should have a mass equal to or larger than $5.2\,\mathcal{M}_\odot$. But if all the stars in the system are coeval, this most massive star in the inner binary should be evolved too, and thus brighter than the primary, refuting the triple-star hypothesis. Refuting the hypothesis that this is an Algol system is more difficult because even a $12\,\mathcal{M}_\odot$ companion on the main sequence would be fainter than the B5Ib primary. However, we note that the absorption lines in the HERMES spectrum do not show any clear double profile despite the fact that the spectrum was obtained at the phase with maximum radial-velocity difference between the two components. Moreover there are only few known Algol systems with such a long period, ≈ 216d, and consisting of early-type stars (μ Sgr being such an example). Another possibility is that this source may have a dormant black hole companion. More observations and modeling will be needed to decide between the different hypotheses. We finally note that the astrometric ruwe parameter of this star is 2.10, which suggests that in the next release it will be possible to obtain an astrometric orbit.

We now move our attention to SB1 sources which can be classified as belonging to the main sequence, for which an estimate of the mass of the primary is provided by IsocLum. Restricting the search for compact object companions to main sequence primaries allows to reduce the number of false detections where the secondary is a normal main sequence star outshined by an evolved primary. We then selected from the table presented in Sect. 5.1 the SB1 sources for which m2_lower > m1_upper and significance > 20. This results in 68 sources; among them 15 have m2_lower > $3\,\mathcal{M}_\odot$ and 25 $1.4\,\mathcal{M}_\odot$ < m2_lower ≤ $3\,\mathcal{M}_\odot$. Their position in the magnitude-colour diagram is shown in Fig. 45.

It should be noted that spectroscopic radial velocity of stars cooler than 3875 K were not processed by the NSS pipeline. This introduces a selection on the mass of the primary, so that

[17] http://www.mercator.iac.es/

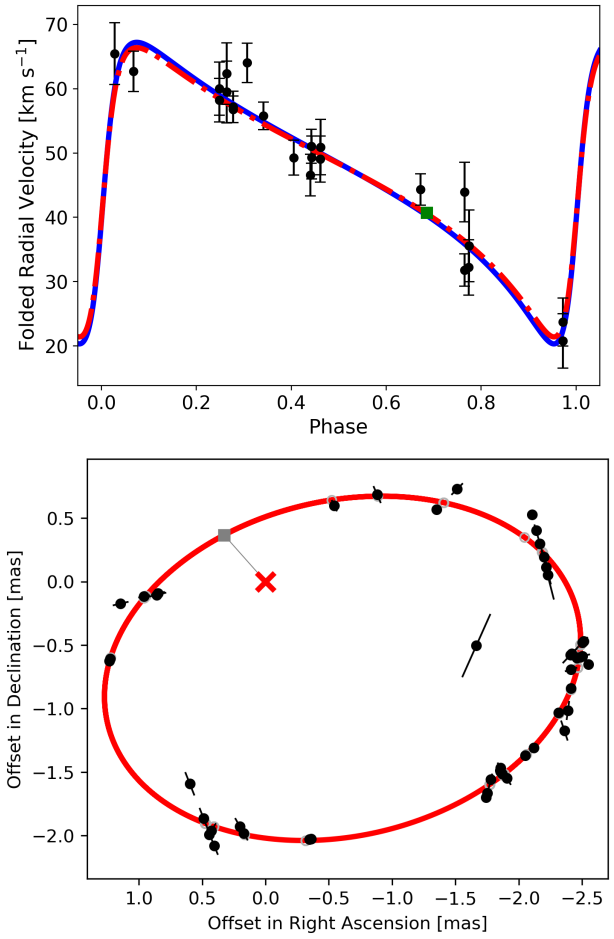

Fig. 43. *Top panel*: Phase-folded radial velocity data of *Gaia* DR3 5136025521527939072, together with the orbits using separately the astrometric (red dot-dashed line) and spectroscopic (blue solid line) orbital elements; the OHP/Sophie external measurements (green squared point) was not part of the fit. *Bottom panel*: Along-scan residuals of the mean epoch astrometric measurements (black symbols) relative to the model positions (grey circles) and the astrometric orbit (red solid line) of the same source. The red cross marks the focus of the orbit and the grey square is the periastron location.

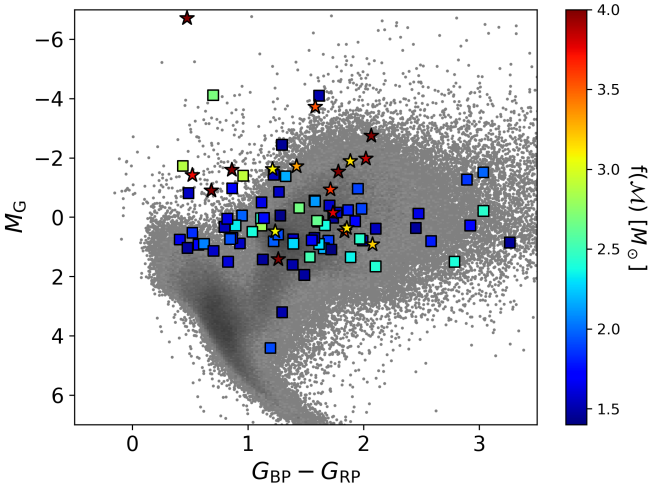

Fig. 44. HRD of SB1 solutions with $f(\mathcal{M}) > 1.4\,\mathcal{M}_\odot$ and `significance` > 20. Squared symbols are for sources with $1.4\,\mathcal{M}_\odot < f(\mathcal{M}) \leq 3\,\mathcal{M}_\odot$, star symbols for sources with $f(\mathcal{M}) > 3\,\mathcal{M}_\odot$. The background grey scale shows the density distribution of all SB1 solutions.

almost no SB1 is present in the catalogue with a primary mass below $0.6\,\mathcal{M}_\odot$. So, it is not possible with this selection to obtain candidates with companions belonging to the main population of white dwarfs.

Particularly interesting are sources with `m2_lower` > $3\,\mathcal{M}_\odot$, which could have a dormant black hole companion. We checked each of the candidates and we found that, among sources with `m2_lower` > $3\,\mathcal{M}_\odot$ the sources *Gaia* DR3 5482724739203311136 and *Gaia* DR3 6000420920026118656 are known eclipsing binaries (Otero 2008; Avvakumova et al. 2013), classified as Algol type, while *Gaia* DR3 1850548988047789696 is an Algol type eclipsing binary detected by *Gaia*.

We then checked the *Gaia* and TESS (Ricker et al. 2015) photometry for the other 11 sources, and all show a modulation of the flux, in phase with the radial velocity, similar to the one expected from an ellipsoidal star[18], confirming the binary nature. This ellipsoidal behaviour, however, suggests that these stars are rather evolved, but the small amplitude of the modulation (a few percents) tells us that the primaries do not fill their Roche lobe. Using the relation between the mass ratio and the effective radius of the Roche lobe provided by Eggleton (1983), we get that the mass required for the primary to fill the Roche lobe, given the radii estimated with the IsocLum code, would be always below $0.1\,\mathcal{M}_\odot$, which is too low for an evolved star and for the observed effective temperature. A more detailed modelling of the light curve of these objects is out of the scope of this article.

The already known 17 X-ray binaries with BH companions (Corral-Santana et al. 2016) have periods of 0.3 - 5 days. We do expect the similar *dormant* binaries to have longer periods, and therefore the range we find here is consistent with the expected periods. Our sources shall nevertheless be considered as candidates only, because they can have other explanations than having compact companions. With the information that we have, we cannot rule out the possibility that these sources are Algol-type systems, however the bluest sources should be considered as more promising candidates of dormant black holes because they are nearer the main sequence than redder sources, and therefore cannot easily outshine a MS companion. Finally, we cannot exclude, as commented before, that the unseen companion is the inner binary composed by two MS stars. The periods of these 11 candidates range from 8.2 to 23.5 days, not short enough to exclude the triple system hypothesis.

The data of these 11 candidates are reported in Table 10. Figure 46 shows the phase-folded radial velocity of the source *Gaia* DR3 2966694650501747328, together with its phase-folded TESS and *Gaia* normalised flux.

8. Substellar companions

The two well-known categories of substellar companions, planets and brown dwarfs, have been for a few decades now the objective of long-term ground-based Doppler search programs in the Solar neighbourhood (e.g., Cumming et al. 2008; Howard et al. 2010; Mayor et al. 2011; Bonfils et al. 2013; Butler et al. 2017; Rosenthal et al. 2021; Pinamonti et al. 2022). The *Gaia* DR3 astrometric performance levels reach the sensitivity to detect substellar companions around a statistically significant number of stars, enabling first-time measurements of their three-dimensional orbital architectures and true masses.

[18] *Gaia* DR3 2219809419798508544 and *Gaia* DR3 4514813786980451840 are also classified as eclipsing, but the light curve is clearly ellipsoidal. See Mowlavi et al. (2022) for more details about this type of misclassification.

Table 10. Source candidates with compact object companions with `m2_lower` > 3 $\mathcal{M}_\odot$ and `m2_lower` > `m1_upper` from `SB1` solutions with `significance`>20. The radius R and dereddened $G_{BP,0} - G_{RP,0}$ colour were obtained with IsocLum.

Gaia DR3	Period (days)	$f(\mathcal{M})$ ($\mathcal{M}_\odot$)	$\mathcal{M}_1$ ($\mathcal{M}_\odot$)	`m2_lower` ($\mathcal{M}_\odot$)	R ($R_\odot$)	$a_1 \sin i$ ($R_\odot$)	$G_{BP,0} - G_{RP,0}$
2219809419798508544	10.8653±0.0025	1.287	1.949	3.129	$3.95^{+0.23}_{-0.11}$	22.44	0.598
4514813786980451840	22.0204±0.0124	1.559	2.477	3.746	$4.86^{+0.38}_{-0.36}$	38.30	0.368
5694373091078326784	12.8848±0.0040	1.660	2.161	3.708	$3.82^{+0.19}_{-0.16}$	27.37	0.341
2966694650501747328	10.3980±0.0011	1.158	2.082	3.096	$3.64^{+0.18}_{-0.05}$	21.04	0.385
948585824160038912	8.2019±0.0015	1.472	2.016	3.283	$3.67^{+0.09}_{-0.21}$	19.45	0.427
2197954362764248192	17.5097±0.0070	1.470	2.178	3.359	$5.71^{+0.49}_{-1.37}$	32.24	0.591
2933630927108779776	14.7175±0.0007	1.225	2.178	3.221	$4.39^{+0.19}_{-0.16}$	27.02	0.443
448452383082046208	23.4939±0.0131	1.474	2.318	3.584	$4.61^{+0.36}_{-0.43}$	39.25	0.514
5243109471519822720	14.9137±0.0005	1.565	2.014	3.649	$4.23^{+0.09}_{-0.08}$	29.58	0.603
5536105058044762240	12.1766±0.0039	1.180	2.178	3.000	$4.50^{+0.15}_{-0.17}$	23.52	0.481
6734611563148165632	14.3444±0.0016	1.695	2.103	3.883	$4.22^{+0.12}_{-0.13}$	29.60	0.462

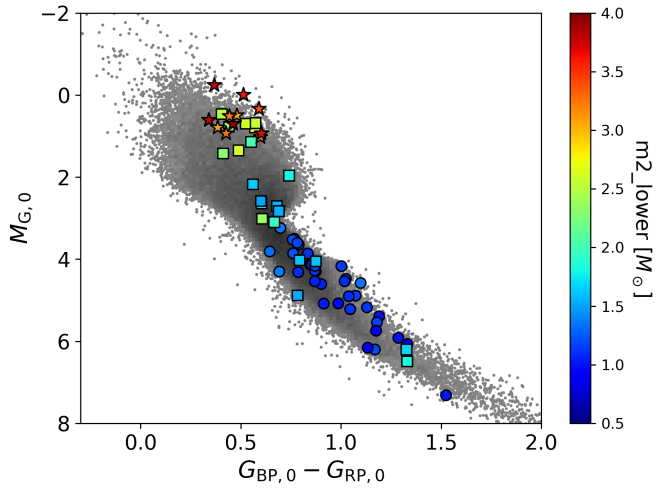

Fig. 45. Dereddened HRD of compact object companion candidates from `SB1` solutions on the main sequence. Circle symbols are for sources with `m2_lower` ≤ 1.4 $\mathcal{M}_\odot$, square symbols are for sources with 1.4 $\mathcal{M}_\odot$ < `m2_lower` ≤ 3 $\mathcal{M}_\odot$, stars symbols for sources with `m2_lower` > 3 $\mathcal{M}_\odot$. The background grey scale shows the density distribution of all `SB1` solutions classified as belonging to the main sequence by IsocLum.

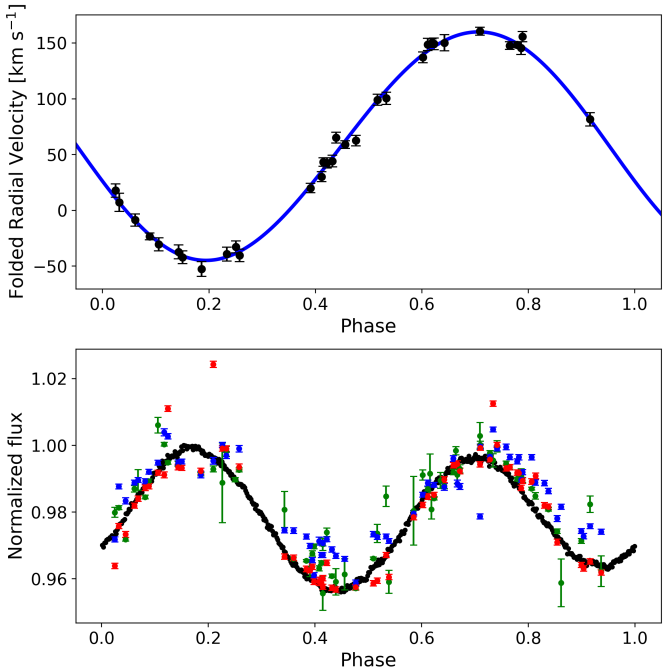

Fig. 46. *Top panel*: Phase-folded radial velocity of *Gaia* DR3 2966694650501747328 (P = 10.398d). *Bottom panel*: phase-folded TESS (black circles) and *Gaia* normalised flux (green, blue and red circles: flux in G, G_{BP} and G_{RP} bands respectively).

8.1. Astrometry: substellar companions

A naive search for substellar companions detected by *Gaia* astrometry might simply select solutions with low values of the astrometric mass function, say $f(\mathcal{M}) < 0.001\ \mathcal{M}_\odot$. However, inspection of Fig. 47 shows that a sizeable fraction of companions of sources with low $f(\mathcal{M})$ do not have small secondary mass with a negligible flux ratio but rather have a flux ratio close to the mass ratio, leaving them to clearly stand above the main sequence.

Keeping this in mind, we browsed the catalogue of masses presented in Sect. 5.1 to investigate the regime of astrometrically detected companions with lower mass bound $\mathcal{M}_c$ (assuming they contribute no flux) in the substellar regime, operationally defined as having $20 \leq \mathcal{M}_c \leq 80\ \mathcal{M}_{\rm Jup}$ and $\mathcal{M}_c \leq 20\ \mathcal{M}_{\rm Jup}$ for brown dwarfs (BDs) and exoplanets (EPs), respectively. For a subset of sources with orbital solutions in the *Gaia* DR3 archive but without a companion mass estimate in our catalogue of masses, the information was derived based on primary mass estimates from the Starhorse catalogue (Anders et al. 2022).

A total of 1843 BDs and 72 EPs were identified in the catalogue of companion masses. This includes 20 sources with `AstroSpectroSB1` solution type that have upper bounds to the companion mass < 80 $\mathcal{M}_{\rm Jup}$, i.e. for which the assumption of negligible flux ratio is confirmed. A small subset of 10 BDs were already known, identified in ground-based RV surveys for planets Ma & Ge (2014); Wilson et al. (2016); Kiefer et al. (2019); Dalal et al. (2021). We report in Table 11 the basic comparison between period and eccentricity from *Gaia* and the literature, minimum and true mass estimates. A total of 9 known EPs were also validated against literature sources, and we report the same information in Table 11. As an illustrative example, the astrometric orbital solution for HD 81040 b is shown in `https://www.cosmos.esa.int/web/gaia/iow_20220131`. Additional plots of *Gaia* DR3 orbits of substellar companions can also be found in Holl et al. (2022b).

Table 11. Known substellar companions with a confirmed mass in the planetary and brown dwarf regime, respectively.

Gaia DR3	Name	$\mathcal{M}_c \sin i$ ($\mathcal{M}_{\rm Jup}$)	$\mathcal{M}_c$ ($\mathcal{M}_{\rm Jup}$)	i (deg)	$P_{\rm lit}$ (days)	$P_{\rm Gaia}$ (days)	$e_{\rm lit}$	$e_{\rm Gaia}$	a_0 (mas)	Refs.
6421118739093252224	HD 175167 b	7.8 ± 3.5	9.5 ± 0.9	28 ± 19	1290 ± 22	898 ± 198	0.54 ± 0.09	0.19 ± 0.12	0.22 ± 0.02	1
4062446910648807168	HD 164604 b	2.7 ± 1.3	14.3 ± 5.5	29 ± 19	606 ± 9	615 ± 12	0.24 ± 0.14	0.61 ± 0.34	0.56 ± 0.22	1,2
1594127865540229888	HD 132406 b	5.6	6.7 ± 2.1	122 ± 14	974 ± 39	893 ± 251	0.34 ± 0.09	0.31 ± 0.29	0.16 ± 0.04	3
4745373133284418816	HR 810 b	2.26 ± 0.18	6.2 ± 0.5	87 ± 6	312 ± 5	332 ± 6	0.15 ± 0.05	0.04 ± 0.2	0.30 ± 0.02	4,5
2367734656180397952	BD -17 0063 b	5.1 ± 0.12	4.3 ± 0.5	80 ± 6	656 ± 0.6	649 ± 36	0.54 ± 0.005	0.28 ± 0.22	0.22 ± 0.02	6
5855730584310531200	HD 111232 b	6.8	8.3 ± 0.6	97 ± 4	1143 ± 14	882 ± 34	0.20 ± 0.01	0.50 ± 0.10	0.51 ± 0.03	7
637329067477530368	HD 81040 b	6.8 ± 0.7	7.9 ± 0.9	108 ± 6	1002 ± 7	851 ± 113	0.53 ± 0.04	0.37 ± 0.15	0.39 ± 0.03	8
4976894960284258048	HD 142 b	1.3 ± 0.2	7.1 ± 1.0	59 ± 7	350 ± 4	319 ± 7	0.26 ± 0.18	0.26 ± 0.23	0.21 ± 0.03	5,9,10
2603090003484152064	GJ 876 b	2.1 ± 0.2	3.6 ± 0.4	101 ± 8	61.08 ± 0.01	61.4 ± 0.2	0.027 ± 0.002	0.16 ± 0.15	0.43 ± 0.05	11-18
2651390587219807744	BD -00 4475 b	25 ± 2	48.4 ± 7.6	129 ± 7	723.2 ± 0.7	780 ± 84	0.39 ± 0.01	0.48 ± 0.11	1.91 ± 0.28	19
2778298280881817984	HD 5433 b	49 ± 3	53.8 ± 1.7	12 ± 39	576.6 ± 1.6	576.7 ± 10.6	0.81 ± 0.02	0.46 ± 0.12	1.04 ± 0.03	19
3309006602007842048	HD 30246 b	55^{+20}_{-8}	40.6 ± 8.3	78 ± 2	990 ± 6	814 ± 141	0.84 ± 0.08	0.59 ± 0.10	1.34 ± 0.24	19
3750881083756656128	HD 91669 b	30.6 ± 2.1	43.2 ± 2.2	58 ± 3	497.5 ± 0.6	500.4 ± 6.9	0.448 ± 0.002	0.32 ± 0.06	0.73 ± 0.04	19
3751763647996317056	HD 89707 b	54^{+8}_{-7}	82.5 ± 12.7	54 ± 10	298.5 ± 0.1	297 ± 2	0.90 ± 0.04	0.68 ± 0.20	1.82 ± 0.30	19
685029558383335168	HD 77065 b	41 ± 2	64.2 ± 5.1	42 ± 3	119.113 ± 0.003	119.1 ± 0.2	0.694 ± 0.0004	0.70 ± 0.04	1.04 ± 0.07	20
855523714036230016	HD 92320 b	59.4 ± 4.0	70 ± 3.1	111 ± 2	145.4 ± 0.01	145.1 ± 0.3	0.323 ± 0.001	0.26 ± 0.05	0.82 ± 0.01	20
824461960796102528	HD 82460 b	73.2 ± 3.0	62.5 ± 6.4	66 ± 1	590.9 ± 0.2	579 ± 6	0.84 ± 0.01	0.73 ± 0.04	1.63 ± 0.09	21
873616860770228352	BD +29 1539 b	59.7 ± 2.0	60.7 ± 23.5	120 ± 9	175.87 ± 0.01	173 ± 3	0.275 ± 0.001	0.43 ± 0.12	0.61 ± 0.14	21
5563001178343925376	HD 52756 b	59.3 ± 2.0	61.2 ± 8.6	73 ± 4	52.8657 ± 0.0001	52.9 ± 0.1	0.678 ± 0.0003	0.54 ± 0.16	0.54 ± 0.08	22

References. (1) Arriagada et al. (2010); (2) Feng et al. (2019); (3) da Silva et al. (2007); (4) Kürster et al. (2000); (5) Butler et al. (2006); (6) Moutou et al. (2009); (7) Mayor et al. (2004); (8) Sozzetti et al. (2006); (9) Tinney et al. (2002); (10) Wittenmyer et al. (2012); (11) Trifonov et al. (2018); (12) Rivera et al. (2005); (13) Rivera et al. (2010); (14) Benedict et al. (2002); (15) Marcy et al. (1998); (16) Marcy et al. (2001); (17) Correia et al. (2010); (18) Nelson et al. (2016); (19) Dalal et al. (2021); (20) Wilson et al. (2016); (21) Kiefer et al. (2019); (22) Sahlmann et al. (2011).

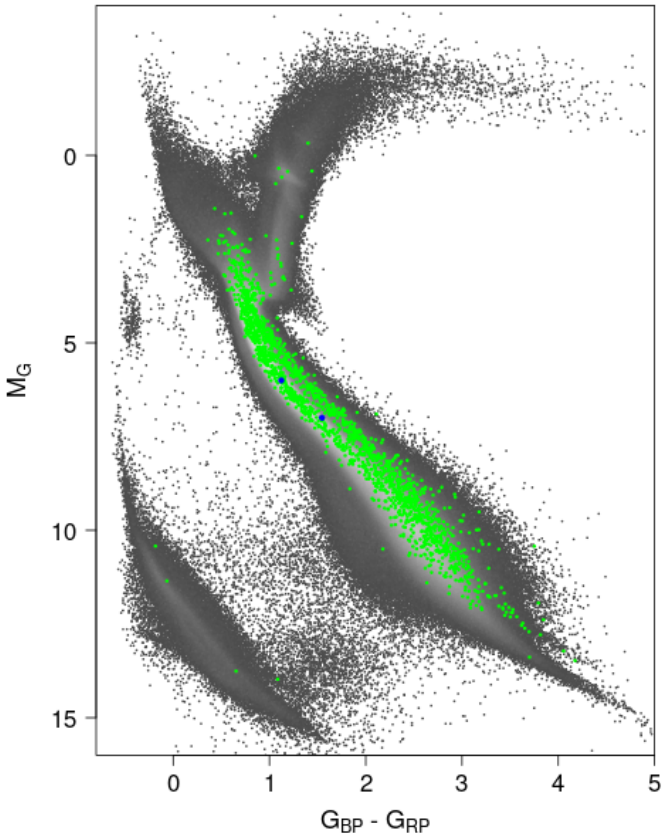

Fig. 47. H-R diagram of sources with low astrometric mass functions ($< 0.001\,\mathcal{M}_\odot$; green dots); the grey background is the DR3 low extinction HRD. A very large fraction are not low-mass companions, rather binaries with a mass ratio similar to their flux ratio. The two blue sources are HD 12800 and HD 3221, described in Sect. 8.7 while the four WDs are discussed in Sect. 8.8.

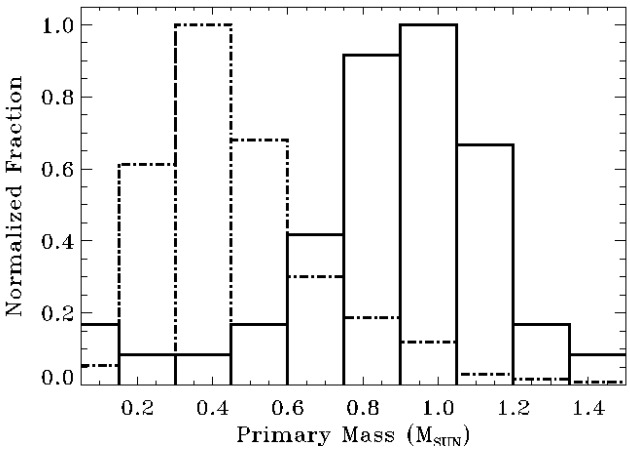

Fig. 48. Primary mass distributions for sources with astrometrically detected substellar companions with `Orbital` (long-dashed histogram) and `OrbitalTargetedSearch*` (solid-line histogram) solution types.

8.2. Astrometric masses: transition regimes

The results of long-term Doppler surveys have allowed studying in some detail the shape of the mass distribution of relatively close-in ($a \lesssim 5$ au or so) companions to solar-type (F-G-K-type) stars, particularly in the two transition regimes between EPs and BDs and between BDs and stars. The most notable feature is the so-called 'brown dwarf desert': the (minimum) mass distribution has a clear decline moving from the planetary-mass to the BD-mass regime, reaches an apparent plateau with a minimum at $\sim 40 - 50\,\mathcal{M}_{\rm Jup}$ ($0.04 - 0.05\,\mathcal{M}_\odot$) and then rises again reaching the stellar-mass regime (e.g., Grether & Lineweaver 2006; Sahlmann et al. 2011; Ma & Ge 2014; Grieves et al. 2017)

Figure 48 shows the distribution of primary masses for sources with astrometrically detected substellar-mass companions for the cases of NSS solution types (`Orbital` and `OrbitalTargetedSearch*`). The medians of the two distributions are $0.42\,\mathcal{M}_\odot$ and $0.91\,\mathcal{M}_\odot$, respectively. The striking difference stems from the different ways the input lists for the two analysis channels were constructed (see Sect. 2.2.1 and Sect. 2.2.2, and references therein). In particular, the bulk of sources with known solutions input to the alternative orbit determination algorithms is constituted by solar-type stars, and this is reflected in Fig. 48. The calibration levels in the bright-star regime is still sub-optimal for *Gaia* DR3; consequently it is expected that nearby, relatively faint low-mass stars might be the sample of primaries around which the chances of detecting substellar companions are maximized, and this is also reflected in Fig. 48.

The three panels of Fig. 49 show the distribution of substellar companion masses for three samples. The distribution for the `OrbitalTargetedSearch*` sample (top panel) corroborates the notion, already provided by Doppler surveys, of a minimum in occurrence at $\sim 40\,\mathcal{M}_{\rm Jup}$ close-in BDs around solar-type stars. For the first time, *Gaia* DR3 offers the opportunity to see the feature in the distribution based on true companion mass estimates, without the ambiguities inherent to studies of the population of substellar companions based on minimum mass values and/or simulation-driven upper mass limits (e.g., Kiefer et al. 2021, and references therein).

The centre and bottom panels of Fig. 49 show the equivalent distribution for the main NSS sample, split into two regimes of companions with substellar masses around M dwarfs ($M_\star < 0.6\,\mathcal{M}_\odot$) and higher-mass primaries, respectively. The first notable feature is the difference in slopes between the two samples rising toward the highest masses: a simple power-law fit returns $N \propto \mathcal{M}_c^{1.56}$ and $N \propto \mathcal{M}_c^{3.03}$ for companions around M dwarfs and higher-mass stars, respectively. A Kolmogorov-Smirnov (K-S) test indicates that the two distributions of substellar companion masses around M dwarfs and higher-mass stars in the center and bottom panels of Fig. 49 have a p-value of $\sim 1 \times 10^{-6}$, allowing to reject the hypothesis that they are drawn from the same distributions. Secondly, the occurrence of detected companions around higher-mass dwarfs appears approximately flat in the approximate range $0.04 \lesssim \mathcal{M}_c \lesssim 0.06\,\mathcal{M}_\odot$. For M dwarf primaries, the distribution continues to show a declining trend towards the lowest-mass end (corresponding to super-Jupiter-mass objects with $\mathcal{M}_c \lesssim 0.01\,\mathcal{M}_\odot$).

The above differences could in principle be mostly due to the not yet well-characterized sensitivity to substellar companions in different mass and orbital separation regimes of *Gaia* DR3 astrometry. However, a few considerations help reinforcing the idea that we are seeing, at least in part, intrinsic features in the distributions rather than effects due to the selection function. Most notably, 1) the flat shape of the distribution in the bottom panel of Fig. 49 is consistent with that of the substellar companions distribution derived from RV surveys (e.g., Kiefer et al. 2019), and 2) the declining trend in the distribution towards the

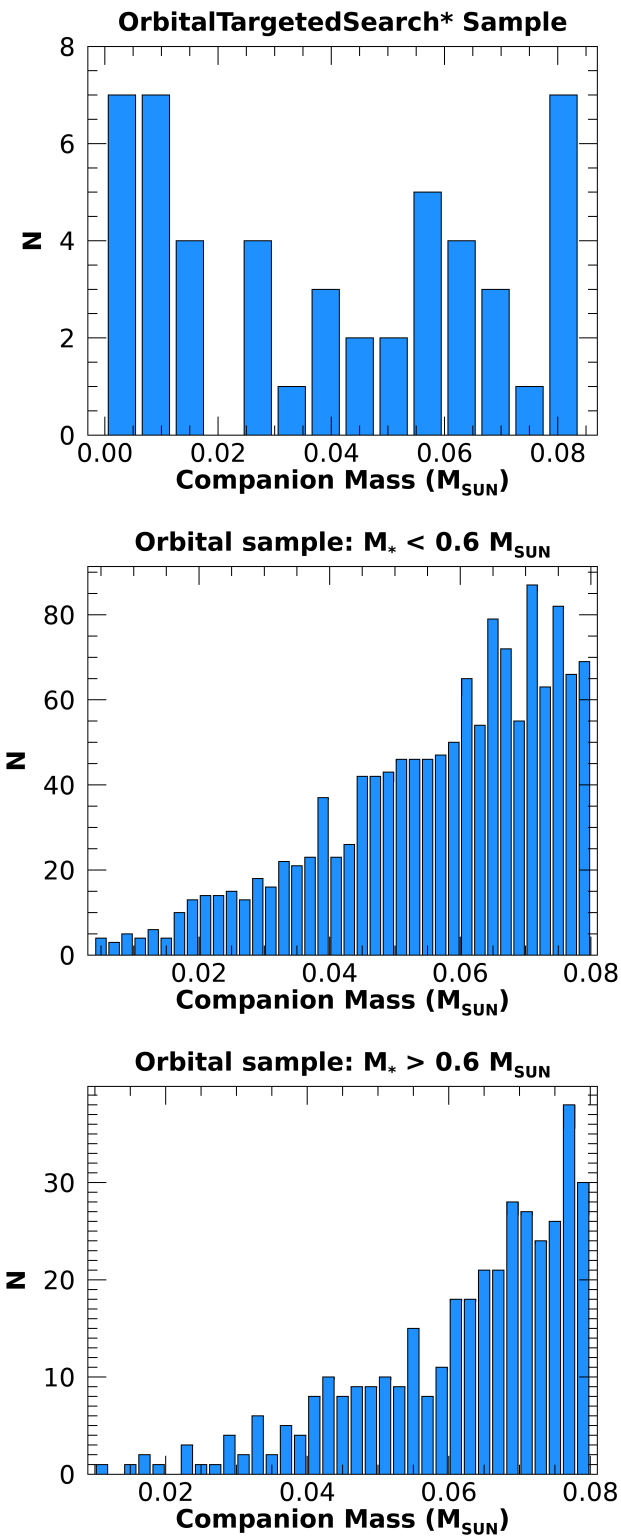

Fig. 49. *Top*: substellar companion mass distribution for the `OrbitalTargetedSearch*` solution type. *Center*: The same, but for the `Orbital` solution type, with a cut-off in the primary mass $\mathcal{M}_\star < 0.6\,\mathcal{M}_\odot$. *Bottom*: the same, but for the `Orbital` solution type, with a cut-off in the primary mass $\mathcal{M}_\star > 0.6\,\mathcal{M}_\odot$.

lowest-mass end in the central panel of Fig. 49 is consistent with the well-established notion of a much lower frequency of giant planets around M dwarfs with respect to solar-type primaries (e.g., Endl et al. 2006; Cumming et al. 2008; Bonfils et al. 2013; Pinamonti et al. 2022). With *Gaia* DR3 we thus achieve the first-ever characterization of a conspicuous population of substellar companions with true mass estimates within typically 1-2 au of nearby M dwarfs.

8.3. Substellar companion frequency in the 100 pc sample

As low-mass stars provide the primary sample around which substellar companions have been detected with *Gaia* DR3 astrometry, we can attempt to derive a first-order estimate of their occurrence rate. Clearly, a detailed assessment of the *Gaia* sensitivity in terms of completeness (estimation of the number of missed companions) and reliability (estimate of the number of false detections) is warranted, but goes beyond the scope of this work, and will be presented elsewhere (Giacobbe et al. in prep.).

Gaia Collaboration et al. (2021b) have shown that *Gaia* DR3 is complete down to the M7 spectral sub-type within 100 pc from the Sun, with an M dwarf sample amounting to 218 366 sources. The NSS sample encompasses 790 astrometrically detected companions with likely substellar masses around M dwarfs within 100 pc. Of these, the vast majority ($\sim$ 94%) are BDs. Under the optimistic assumptions that 1) *Gaia* has homogeneous sensitivity to and is 100% complete for BD companions across the M dwarf 100-pc sample, 2) none of the orbital solutions corresponding to BD companions around this sample are spurious, and 3) the companion does not contribute light, we can then make a first statement on the frequency of BDs around M dwarfs with $P \lesssim 1\,000$ d, which turns out to be $\sim 0.3\%$.

Dieterich et al. (2012) report a BD companion frequency around M dwarfs of $2.3^{+5.0}_{-0.7}\%$ for separation in the range 10-70 au. Bowler et al. (2015) find that such companions in the 10-100 au orbital radius range have an occurrence rate of $2.8^{+2.4}_{-1.5}\%$ around M dwarfs in young moving groups. Susemiehl & Meyer (2022) find a similar frequency ($2.7^{+1.0}_{-0.7}\%$) for field M dwarfs in the same separation interval. Winters et al. (2019) report a formally lower, but still compatible within the uncertainties, $1.3 \pm 0.3\%$ frequency for BDs around M dwarfs within 25 pc in the separation range out to $\sim 300''$.

Our occurrence rate estimate is likely underestimated (pending detailed assessment of the numbers of missed companions vs. those of spurious solutions and incorrectly classified objects), but nevertheless it is a clear example of the fact that *Gaia* DR3 provides critical constraints on the M dwarf binary fraction at close separations and very low mass ratios. Even with corrections for completeness and reliability still to be accounted for, the *Gaia* M dwarf sample in the Solar neighborhood with sensitivity to substellar companions within a few aus is orders of magnitude larger than those of all other spectroscopic surveys combined.

8.4. Astrometric masses: trends with stellar metallicity

The number of new *Gaia* detections of substellar companions in the EP regime is still too small to provide an independent assessment of well-known trends of exoplanet frequency with stellar properties, such as the strong dependence of giant planet occurrence with metallicity (e.g., Fischer & Valenti 2005; Sozzetti et al. 2009; Santos et al. 2011; Mortier et al. 2012; Adibekyan 2019, and references therein). The population of likely BD companions is instead conspicuous, and amenable to verify the outcome of recent statistical investigations.

As an example, Ma & Ge (2014) showed that, using the iron abundance relative to the Sun [Fe/H] as a proxy, the metallicity distribution of BD solar-type hosts has a median and standard deviation [Fe/H] = -0.04 ± 0.28. Using the most recent compilation of BD companions based on Wilson et al. (2016); Kiefer et al. (2019); Dalal et al. (2021), the corresponding values are [Fe/H] = $+0.01 \pm 0.25$. The stellar sample is thus not particularly metal-rich, as is the case of giant-planet hosts (median [Fe/H]$\sim +0.12$, e.g. Adibekyan 2019), but is also not as metal-deficient as the typical field stars in the solar neighbourhood (depending on stellar sample, with median [Fe/H] in the range [–0.10,–0.15], see e.g. Nordström et al. 2004; Raghavan et al. 2010; Sousa et al. 2011; Adibekyan 2019).

In Gaia Collaboration et al. (2022a) recipes are outlined for selection of sources with global metallicity ([M/H]) of good and intermediate quality determined based on *Gaia* data. A total of 17 129 sources with an astrometric orbital solution were selected to have intermediate-quality [M/H] from the archive. Unsurprisingly, the overwhelming majority of [M/H] determinations is for the brighter solar-type stars, therefore the typical M-dwarf primary with a substellar companion does not have a metallicity determination. However, we find [M/H]= -0.02 ± 0.29 for a sample of 143 F-G-K-type BD hosts. For reference, applying a more strict recipe for good-quality [M/H] returns a sample of 74 sources with [M/H]= $+0.01 \pm 0.27$, both estimates are in excellent agreement, and indeed indistinguishable, with literature results. If no quality constraints are used, 327 sources with a substellar companion and a *Gaia*-derived metallicity have [M/H]= -0.25 ± 0.49, which is indicative of the need to restrict ourselves to the regime of primaries with better-calibrated metallicities.

8.5. Known substellar objects: statistics and notable examples

The comparison between *Gaia* orbital solutions and companion mass estimates for known substellar companions and literature results, small as the sample might be, is interesting for a number of reasons.

First of all, a quick look at Table 11 allows us to underline how the angular orbit size for known BDs is always $\gtrsim 0.5$ mas, while the opposite, with a few exceptions, holds for the known EPs, HD 132406 b being the record holder with the smallest measured angular semi-major axis: $a_1 = 136 \pm 40$ μas. Overall, for both EPs and BDs there is a tendency to underestimate orbital periods longer than the time-span of *Gaia* observations. Not unexpectedly, orbital eccentricities are typically more loosely constrained by *Gaia* astrometry with respect to those from Doppler spectroscopy, and very high-eccentricity orbits ($e \gtrsim 0.8$) are typically underestimated. The loss of accuracy in the long-period and high-eccentricity regimes are known effects, already quantified via detailed simulations by Casertano et al. (2008), and further discussed in e.g. Holl et al. (2022b).

Inspection of Table 11 also shows that there is no simple mapping of $\mathcal{M}_c \sin i$ into $\mathcal{M}_c$ given the derived i value. For some objects (e.g. HD 132406 b, HD 81040 b, and HD 52756 b), the minimum mass estimate translates into a larger true mass in agreement with the determined value of inclination, but in other cases (e.g., HD 164604 b, HR 810 b, and HD 142 b), $\mathcal{M}_c$ is estimated to be much larger than the $\sin i$ value would infer it to be, or even lower (e.g., HD 30246 b and HD 82460 b) than $\mathcal{M}_c \sin i$. When the parameter uncertainties are taken into account, the discrepancies are typically not very statistically significant, but the effect will nevertheless require to be understood. As both minimum and true mass estimates depend on the assumptions made for the mass of the primary, part of the reason for the discrepancy might be due to the heterogeneity of methods used to derive the latter. However, the more fundamental explanation is likely to be found in the overall limitations of *Gaia* DR3 detection sensitivity, including the selection effects and biases introduced by astrometric NSS processing, as discussed in Sect. 4.1 and Appendix C, particularly in the limit of relatively low astrometric signal-to-noise ratios and sub-optimal redundancy in the number of visibility periods with respect to the number of model parameters[19].

Among the companions with a derived mass in the planetary regime, the case of GJ 876 b stands out. The planet constitutes one of the earliest radial-velocity discoveries in the field, first announced by Marcy et al. (1998) as a gas giant with $\mathcal{M}_c \sin i \sim 2\,\mathcal{M}_{\rm Jup}$ orbiting a mid-M dwarf in the backyard of the Sun ($d = 4.67$ pc). Benedict et al. (2002), using HST/FGS data, published the astrometric orbit of GJ 876 b (constrained by the RV solution), determining an orbit size of 0.25 ± 0.06 mas, an inclination of 84° and a true mass very close to the minimum mass limit. The GJ 876 planetary system was subsequently found to host 4 planets, the hot super Earth GJ 876 d with period of ~ 2 d, the two Jupiter-type planets GJ 876 c,b with periods of ~ 30 and ~ 61 d, respectively, and the Neptune-mass companion GJ 876 e with a period of ~ 125 d. The three outermost companions are dynamically interacting, locked in a 1:2:4 Laplace mean-motion resonance, which has been the subject of many studies (e.g., Rivera et al. 2005, 2010; Correia et al. 2010; Nelson et al. 2016; Trifonov et al. 2018). The more recent investigations, based on dynamical considerations, infer a close-to-coplanar configuration for the three interacting planets, and a likely inclination of GJ 876 b $\sim 50-60°$. This implies a true mass $\mathcal{M}_c \sim 2.3 - 2.7\,\mathcal{M}_{\rm Jup}$. The amplitude of the astrometric perturbation determined with *Gaia*, 0.43 ± 0.05 mas, is larger than that measured by HST/FGS, and discrepant at the 2.3σ level. The inferred mass, $3.6\,\mathcal{M}_{\rm Jup}$, is correspondingly larger, and also in this case the derived inclination $i = 101°$ does not allow for a simple mapping from the $\mathcal{M}_c \sin i$ value.

A number of known companions, which in the literature have minimum mass estimates in the planetary regime, appear in Table 3 with much higher true mass estimates from Gaia. These appear in the *Gaia* DR3 archive as validated orbital solutions of type `OrbitalTargetedSearchValidated`. A few cases of particular interest are discussed below:

1. HD 114762 (*Gaia* DR3 3937211745905473024): The first substellar companion candidate around a solar-type star with minimum mass $\mathcal{M}_c \sin i = 0.011 \pm 0.001\,\mathcal{M}_\odot$ was inferred from radial velocity variations by Latham et al. (1989). *Gaia* DR1 noise modelling resulted in a considerably higher companion mass estimate of $0.103^{+0.030}_{-0.025}\,\mathcal{M}_\odot$ (Kiefer 2019). The *Gaia* DR3 orbital solution has a period of 83.73 ± 0.12 d in agreement with the radial-velocity orbit and an orbit size of $a_0 = 1.80 \pm 0.07$ mas. Using the primary mass estimate from Table 3, the inferred companion mass is $\mathcal{M}_c = 0.21 \pm 0.01\,\mathcal{M}_\odot$, using standard linear propagation of the uncertainties. *Gaia* DR3 therefore establishes that the companion is a low-mass M dwarf and not a substellar object;
2. HD 164604 (*Gaia* DR3 4062446910648807168): Arriagada et al. (2010) announced a low-confidence detection of a $\mathcal{M}_c \sin i \sim 2.7\,\mathcal{M}_{\rm Jup}$ companion on a 606 ± 9 d orbit, whose

[19] The typical number of visibility periods is only twice the number of fitted parameters in an orbital model (see Appendix C, and also Holl et al. 2022b)

parameters were then refined by Feng et al. (2019) who reported $\mathcal{M}_c \sin i = 1.99 \pm 0.26\,\mathcal{M}_{\rm Jup}$ and $P = 641 \pm 9$ d. The *Gaia* DR3 orbital solution has $P = 615 \pm 12$ d (in agreement at the 1.7σ and 0.6σ level with Feng et al. (2019) and Arriagada et al. (2010), respectively) and $a_0 = 0.56 \pm 0.22$ mas. The inferred companion mass is $\mathcal{M}_c = 14.3 \pm 5.5\,\mathcal{M}_{\rm Jup}$;

3. HD 162020 (*Gaia* DR3 5957920668132624256): Udry et al. (2002) published the discovery of a $P = 8.428$ d, slightly eccentric ($e = 0.28$) $\mathcal{M}_c \sin i \sim 14\,\mathcal{M}_{\rm Jup}$ companion, whose minimum mass was recently updated to $9.8 \pm 2.7\,\mathcal{M}_{\rm Jup}$ by Stassun et al. (2017). The *Gaia* DR3 orbital solution has $P = 8.429 \pm 0.001$ d, $e = 0.23 \pm 0.05$, and $a_0 = 0.91 \pm 0.03$ mas. The detected companion is a low-mass star with $\mathcal{M}_c = 0.39 \pm 0.02\,\mathcal{M}_\odot$;
4. KIC 7917485 (*Gaia* DR3 2075978592919858432): Murphy et al. (2016) published the detection of a $\mathcal{M}_c \sin i = 11.8^{+0.8}_{-0.6}\,\mathcal{M}_{\rm Jup}$ companion on a $P = 840^{+22}_{-20}$ d orbit around the Delta Scuti, A-type star Kepler-1648, based on a pulsation timing variations technique. The *Gaia* DR3 orbital solution has $P = 810 \pm 28$ d and $a_0 = 0.42 \pm 0.02$ mas. At a distance of 1.38 kpc, the companion turns out to be an M dwarf with $\mathcal{M}_c = 0.55 \pm 0.03\,\mathcal{M}_\odot$.

8.6. Validated orbital solutions that can imply new exoplanet discoveries

Two sources have validated astrometric orbital solutions (see Holl et al. 2022b, for details) that imply the presence of previously-unpublished planetary-mass companions if a 'binary scenario' can be excluded. In such scenario the small apparent orbit size would be caused by a binary star with components of similar mass and brightness ratios. These sources are:

1. HIP 66074 (*Gaia* DR3 1712614124767394816): The *Gaia* DR3 orbital solution has $P = 297 \pm 2.8$ d, $e = 0.46 \pm 0.17$, $a_0 = 0.21 \pm 0.03$ mas. Given the primary mass estimate corresponding to an M0 dwarf, the inferred companion mass in the exoplanet scenario is $\mathcal{M}_c = 7.3 \pm 1.1\,\mathcal{M}_{\rm Jup}$.
2. HIP 28193 (*Gaia* DR3 2884087104955208064): The orbital period, semi-major axis and eccentricity of this new exoplanet are 827 ± 50 d, $e = 0.07 \pm 0.10$, and $a_0 = 0.25 \pm 0.02$ mas, respectively. Using the K-dwarf primary mass from Table 3, the inferred companion in the exoplanet scenario is a super-Jupiter with a mass of $5.3 \pm 0.6\,\mathcal{M}_{\rm Jup}$. We note that, had we used Monte Carlo resampling, the semi-major axis distribution would have been asymmetric with larger uncertainties, and this would have been the case for the companion-mass distribution as well. This is an example of a solution with a poorly-constrained eccentricity ($e = 0.07 \pm 0.10$) for which the uncertainties in the Thiele-Innes coefficients are likely overestimated and Monte-Carlo resampling is not advisable (cf. Babusiaux et al. 2022; Holl et al. 2022b).

A third source (*Gaia* DR3 1035000055055287680, HIP 40497) that initially also fell into this category, has been identified as SB2 in the literature (Busà et al. 2007), see also the discussion in Holl et al. (2022b). This illustrates that the risk of confusing the binary and exoplanet scenarios is real when only considering the *Gaia* astrometric orbit.

For HIP 66074 and HIP 28193 we can, however, make use of auxiliary radial-velocity information. To evaluate the binary scenario where the companion is a main-sequence star, we used the mass-luminosity relationships of Henry & McCarthy (1993) to estimate that the two components must have masses that agree within a few percent to be compatible with both the orbital parameters and the photocentre orbit size. Consequently, the primary component's RV semi-amplitudes of HIP 66074 and HIP 28193 would be $K_1 \sim 20$ km s^{-1} and $K_1 \sim 9$ km s^{-1}, respectively, clearly incompatible with the high-precision RVs used for validating the orbital solution that have dispersions that are three orders of magnitude smaller (Butler et al. 2017; Holl et al. 2022b). Similarly, the *Gaia* DR3 `radial_velocity_error`, computed from the dispersion of individual *Gaia* RV measurements, is 0.15 km s^{-1} and 0.16 km s^{-1}, respectively, which lies in the first percentile for sources with $G < 12$, and therefore also appears incompatible with the binary scenario. The blending of the SB2 spectra could possibly lead to such suppressed RV variability. In the case of HIP 28193, the small uncertainties in the ground-based RVs coupled with the estimated FWHM of the underlying cross-correlation functions of $\lesssim 9$ km s^{-1} speak against this possibility[20].

In terms of absolute magnitudes of these systems, the difference between the exoplanet and binary scenario amounts to ~ 0.8 mag, which because of the width of the observed HRD can also not be used to definitely rule out the binary scenario.

In the Hipparcos-*Gaia* catalogues of accelerations produced by Brandt (2021) and Kervella et al. (2022) no statistically significant PMa is reported for HIP 66074 (S/N $\sim$ 1), while a moderately high PMa (S/N$\sim$ 10) at the *Gaia* mean epoch is found for HIP 28193. For the relatively short-period orbit of the companion around HIP 66074, the inferred companion mass is approximately in line with a S/N$\sim$ 1 in the proper motion difference. In the case of the longer-period orbit of the companion around HIP 28193, the PMa value this might point to a companion with a larger mass than the one inferred nominally. An alternative possibility would be that the *Gaia* orbit has significantly underestimated the true period.

To summarize, the most likely scenario for both HIP 66074 and HIP 28193 is therefore the presence of a newly-discovered giant exoplanet. A more detailed analysis and probably more auxiliary data are needed to definitely rule out the binary scenario. When that is achieved, these are to be considered as the first *Gaia* astrometric planet detections and the first examples of confirmed exoplanet discoveries with the astrometry technique.

8.7. Candidates with substellar masses: statistics and notable examples

Among the substellar mass candidates with solution type `OrbitalTargetedSearch`, a few are worth particular mention:

1. HD 12800 (*Gaia* DR3 5221352614625345 28): the *Gaia* DR3 orbital solution for this bright source (54 Cas) has $P = 401 \pm 12$ d, $a_0 = 0.25 \pm 0.05$ mas, and $\mathcal{M}_c = 5.6 \pm 1.4\,\mathcal{M}_{\rm Jup}$. This is the only candidate companion around a main-sequence solar-type star with a mass well in the planetary regime.
2. HD 3221 (*Gaia* DR3 4901802507993393664): the *Gaia* DR3 orbital solution for this bright solar-type star has $P = 476 \pm 5$ d, $a_0 = 0.36 \pm 0.01$ mas, and $\mathcal{M}_c = 14.2 \pm 0.6\,\mathcal{M}_{\rm Jup}$. The primary is a fast-rotating ($v \sin i \sim 70$ km s^{-1}), very young star with an estimated age of $\sim 10 - 30$ Myr in the Tucana/Horologium association. The candidate companion, at the planet-brown dwarf mass

[20] At the times of minimum/maximum RV, the separation between the primary and companion RV should be ~ 18 km s^{-1}, i.e. wider than the spectroscopic cross-correlation function.

boundary according to a classical definition (Burrows et al. 2001), if confirmed, would be the first of this type in an orbital separation regime virtually inaccessible to Doppler and direct imaging surveys.

As mentioned above, the population of substellar mass candidates with solution type `OrbitalTargetedSearch*` is typically found around solar-type primaries. It is interesting to note how the eccentricity distributions for EPs and BDs in this sample are marginally different based on K-S test (p-value of 0.04), with the more massive BDs ($\mathcal{M}_c \gtrsim 50\ \mathcal{M}_{\rm Jup}$) having a median $e \sim 0.5$, while EPs and lower-mass BDs ($\mathcal{M}_c \lesssim 40\ \mathcal{M}_{\rm Jup}$) have typically $e \sim 0.3$. This is in agreement with Ma & Ge (2014), and with the notion that the former might correspond to the low-mass tail of objects formed like stars while the latter sample would map the high-mass tail of objects formed like planets.

The population of substellar mass candidates with solution type `Orbital` is instead predominantly found around low-mass M primaries. In this case, the eccentricity distributions of candidate EPs and BDs detected around this sample are indistinguishable, with typically $e \sim 0.4$ in both cases. This might indicate that most of the detected companions might have formed in the same way, and that some of them are actually of intrinsically larger mass compared to the lower mass bounds adopted in this work as discussed in Sect. 8.1.

8.8. Substellar companion candidates to white dwarfs

The `nss_two_body_orbit` table contains 38 orbital solutions for sources on the white dwarf (WD) sequence, all of them correspond to astrometric orbits. Assuming a fixed mass of $0.6\,M_\odot$ for the WD host and that the companion is dark, there are four sources with substellar companion candidates. These are *Gaia* DR3 2813020961166816512 (LP 522-46) with $\mathcal{M}_c \sim 34\,\mathcal{M}_{\rm Jup}$, *Gaia* DR3 2098419251579450880 with $\mathcal{M}_c \sim 34\,\mathcal{M}_{\rm Jup}$, and *Gaia* DR3 6471102606408911360 (L 279-25) with $\mathcal{M}_c \sim 22\,\mathcal{M}_{\rm Jup}$. The last one *Gaia* DR3 4698424845771339520 (WD 0141-675) stands out as being part of the 10 pc sample and with a companion candidate in the planetary-mass range.

In Fig. 39 these four sources are marked with red symbols. Two sources (LP 522-46 and L 279-25) are located above the hydrogen sequence, which suggests that the companion could itself be degenerate and luminous enough to cause an excess in luminosity and at the same time dilute the astrometric orbit signal. The companions of these sources are therefore likely neither dark nor substellar. On the other hand, *Gaia* DR3 2098419251579450880 and WD 0141-675 lie within the hydrogen sequence and therefore Fig. 39 appears consistent with the interpretation of these sources having substellar companions.

WD 0141-675 in particular was included in the OrbitalTargetedSearch sample (Holl et al. 2022b) because it is nearby and metal-polluted (Debes & Kilic 2010), hence represents a promising target to search for the presence of an orbiting giant planet that could act as the much sought-after perturber of the circumstellar material (Debes et al. 2012). The *Gaia* DR3 orbital solution has a period of 33.65 ± 0.05 d and with a WD mass of $0.57 \pm 0.03\,M_\odot$ (Subasavage et al. 2017), the estimated planet mass is $\mathcal{M}_c = 9.26^{+2.64}_{-1.15}\,\mathcal{M}_{\rm Jup}$, where we accounted for all parameter covariances using Monte-Carlo resampling. The resulting $\mathcal{M}_c$ distribution is asymmetric with its mode at $\sim 8.3\,\mathcal{M}_{\rm Jup}$.

With only a handful of known giant planets orbiting white dwarfs (Veras 2021; Blackman et al. 2021), the *Gaia* discovery of a super-Jupiter candidate planet orbiting WD 0141-675 is remarkable. If the *Gaia* DR3 orbit is confirmed and other possible scenarios, e.g. some kind of WD binary system with nearly equal-brightness components (WD 0141-675 is marked with an orange square in Fig. 39), can be excluded this would represent the discovery of the most nearby planet-hosting WD and the first giant planet around a metal-enriched WD, which will make it an important test for our understanding of the fate of stars and their planetary systems.

8.9. Radial Velocity: Substellar companions

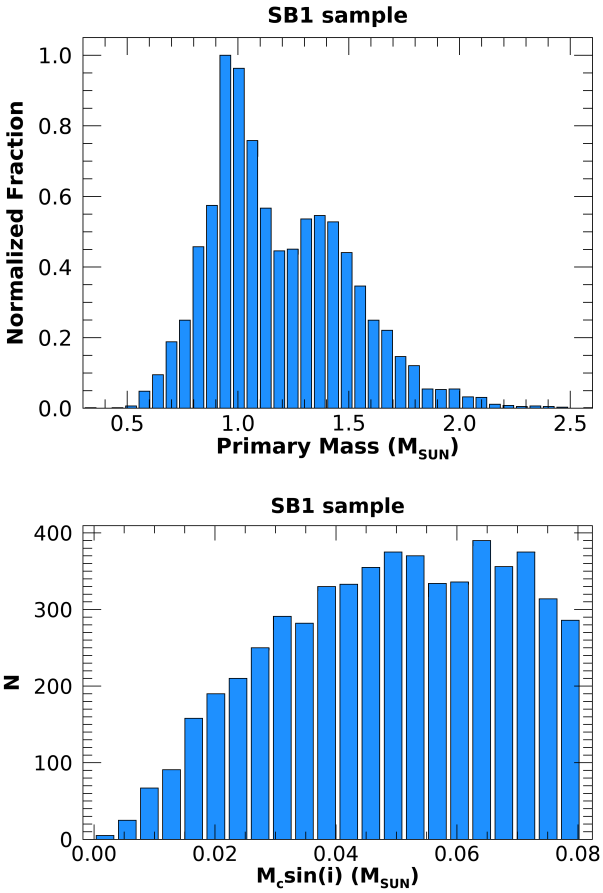

Fig. 50. *Top*: Primary mass distribution for sources with `SB1` solution type and inferred minimum companion masses in the substellar regime. *Bottom*: substellar companion mass distribution for the `SB1` solution type.

Out of 6×10^4 minimum mass estimates for `SB1` solutions (see Table 3), about 10% (5723) have $\mathcal{M}_c \sin i < 0.08\,\mathcal{M}_\odot$, and about 10% of these (437) have $\mathcal{M}_c \sin i < 0.02\,\mathcal{M}_\odot$. Not unexpectedly, the mass distribution for the primaries (see Fig. 50, top panel) has a median of $\sim 1.0\,\mathcal{M}_\odot$, similar to that of the primary mass distribution of `OrbitalTargetedSearch*` sources rather, but with a significantly larger contribution from bright, earlier-type stars. The distribution of $\mathcal{M}_c \sin i$, shown in the lower panel of Fig. 50, contains an expected feature, i.e. the decline in numbers of companions at the low-mass end due to the intrinsic lack of sensitivity of *Gaia* RVS to RV amplitudes of signals typically induced by planetary-mass companions (significantly < 1 km s^{-1}). On the other hand, the number of higher-mass substellar companions appears constant, all the way into the low-mass star regime, and independently on primary mass. This is unexpected, as an intrin-

sically lower frequency of intermediate-mass BDs is observed in RV surveys (Ma & Ge 2014), particularly in the short-period regime to which *Gaia* radial-velocities are sensitive. The eccentricity distributions of SB1 companions with mass estimates in the EP and BD regimes appear entirely indistinguishable, independently of primary mass, and this also is not in agreement with the Ma & Ge (2014) analysis.

For > 80% of the SB1 sample of close-in companions with $\mathcal{M}_c \sin i < 0.08\ \mathcal{M}_\odot$ the orbital solutions have $P < 10$ days, and this fraction grows to > 90% for companions with $\mathcal{M}_c \sin i < 0.02\ \mathcal{M}_\odot$. Such companions, which are detected with typical significance of their K_1-values below 10, typically correspond to primaries with ruwe > 1.4, but they are not expected to be those responsible for high ruwe values, as the typical sizes of the induced astrometric perturbations would escape detection by *Gaia* (e.g. Belokurov et al. 2020). As discussed in Sect. 2.3 a sizeable fraction of these short-period orbits are actually kind of aliases of longer-period ones. For example, the companions reported around HIP 24329, HD 35956, and HD 8691 have $\mathcal{M}_c \sin i \sim 3\ \mathcal{M}_{\rm Jup}$, $\sim 11\ \mathcal{M}_{\rm Jup}$ and $\sim 14\ \mathcal{M}_{\rm Jup}$, respectively, and $P = 0.63$ d, 3.02, and 3.77 d, respectively. However, these sources also have Orbital solutions with P= 1499 d, 1203 d, and 581 d. The latter P values very closely match the published periods of the spectroscopic orbits for the three stars reported by Wilson et al. (2016), Katoh et al. (2013), and Sperauskas et al. (2019), respectively.

The sample of short-period SB1 orbits with minimum masses corresponding to substellar companions should therefore be considered with caution, although not all orbital solutions can be wrong or spurious. For example, a cross-check with the NASA Exoplanet Archive shows that the spectroscopic orbit of WASP-18b (*Gaia* DR3 4955371367334610048), a transiting super-Jupiter with $\mathcal{M}_c \sim 10\ \mathcal{M}_{\rm Jup}$ and $P = 0.94$ d discovered by Hellier et al. (2009) around the Hyades-age F6 dwarf HD 10069, is recovered as an SB1 with the correct period and RV semi-amplitude ($K_1 \sim 1.8$ km s^{-1}). This source has also been detected in the *Gaia* photometry (Eyer et al. 2022) and is present in the vari_planetary_transit table.

The list of most exoplanet candidates detected by *Gaia* using either astrometry, transit or radial velocities is published in https://www.cosmos.esa.int/web/gaia/exoplanets.

9. Multiple stars

Although the NSS pipeline in *Gaia* DR3 produce solutions of binary stars, the results can also be used to uncover higher multiplicity stars. Triple (and higher multiplicity) stars are of particular interest. The study of the architecture and dynamics of hierarchical stellar systems provides precious information on the mechanisms at work during star formation. For example, the fact that the orbits of a hierarchical system are coplanar would indicate that the stars are formed in a viscous accretion disk, while their mass ratios shed light on the disk fragmentation mechanism (see e.g. Tokovinin 2017).

9.1. Multiplicity from spectroscopic and astrometric solutions

A first way to find multiple stars is to look at the sources for which the pipeline produced an astrometric Orbital solution and an SB1/SB2 solution which were not combined. In fact, given that the astrometry is sensitive to long periods/larger orbits, while the spectroscopy is sensitive to shorter periods, in the case of a triple star the astrometry would detect the outer period, while the spectroscopy will unveil the inner period.

Many of the sources for which the Orbital and SB1/SB1C solution was found, but not combined by the pipeline are, however, not triple stars. In many cases they have similar periods but were not combined because of the inconsistency of the other orbital parameters. There are also many cases where the SB solution is actually some kind of alias of the astrometric period; these cases can be spotted noting that the semi-amplitude K_0 of the astrometric motion (defined by Eq. (B.10), substituting a_0/ϖ for a_1) is similar to the semi-amplitude K_1 of the radial velocity curve. These confusing cases have typically a significance lower than 10. We then identify genuine triple stars by selecting those for which the significance of both astrometric and spectroscopic solution is larger than 10, $K_1 > 3 \cdot K_0$ and $P_{\rm Orbital} > 5 \cdot P_{\rm SB}$. With this selection we obtain 81 triple systems from matching Orbital with SB1 solutions, 55 from matching with SB2, 16 from matching with SB2C and none from matching with SB1C. The distribution of the outer vs inner periods of these sources is reported in Fig. 51.

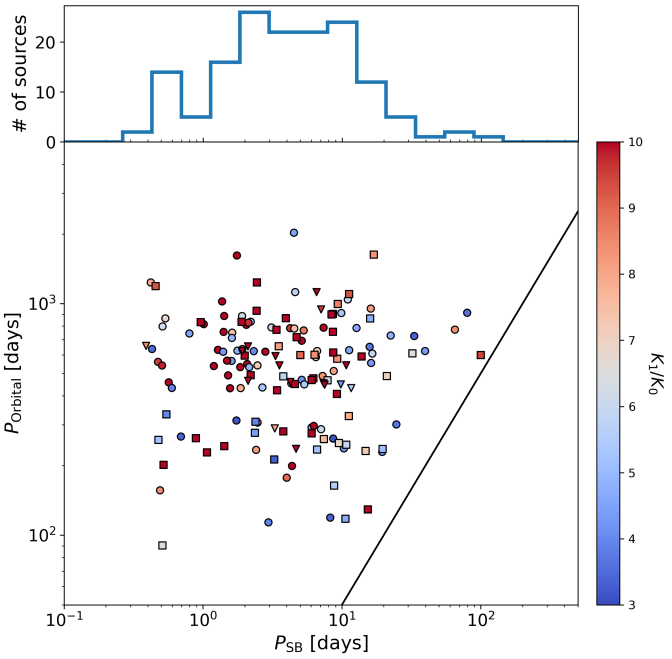

Fig. 51. Distribution of outer vs inner periods for triple systems found matching Orbital with SB1 (circles), SB2 (squares) and SB2C solutions (triangles), coloured by the ratio of spectroscopic over astrometric semi-amplitudes. The solid line shows the limit $P_{\rm Orbital} = 5\ P_{\rm SB}$. Top panel: Integrated distribution of inner periods.

One can also find multiple stars by looking at the sources for which the pipeline produced an astrometric acceleration solution and an SB1/SB2 solution. In this case, the astrometric acceleration would detect outer periods which are around or longer than the length of *Gaia* observations (∼ 1 000 days), while the SB solutions detect the inner periods.

In order to avoid that the astrometric acceleration and the SB solutions are in reality of the same orbit, we selected only SB solutions with a period < 300 days. We also restrain our search to SB solution with significance > 20 to avoid to be polluted by some kind of aliasing.

Distribution of inner periods for triple systems found matching astrometric acceleration and SB solutions is shown in

Fig. 52. We can note that the mode of the distribution is at around 3 days.

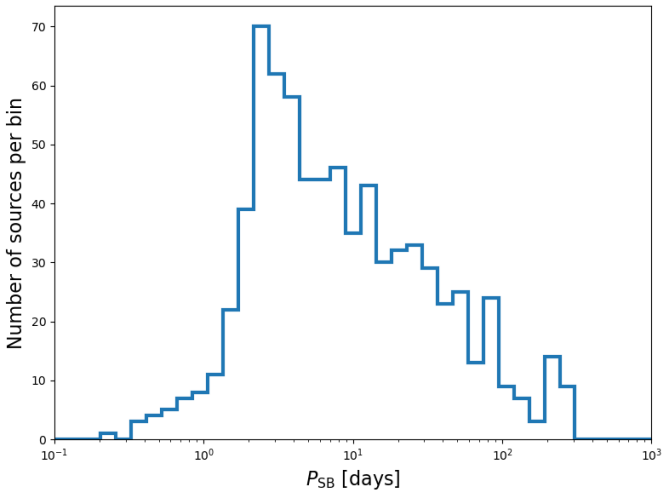

Fig. 52. Distribution of inner periods for triple systems found comparing astrometric acceleration and SB solutions.

9.2. Multiplicity in wide visual binaries

Another method to discover triple or higher multiplicity stars consists in using catalogues of wide visual binaries and see if one of the two components is detected as binary. We started from the El-Badry et al. (2021) catalogue, and selected sources with $\mathcal{R} < 0.01$ (0.08% contamination from chance-alignment), cross-matched with `nss_two_body_orbit` solutions and spectroscopic trends, and we found 10 063 systems for which one of the two components is a non-single star and 52 systems where both components are non-single stars. For 10 of the first group, the non single component is actually a triple star (`Orbital+SB1/SB2`, selected as in Sect. 9.1), making them a quadruple system.

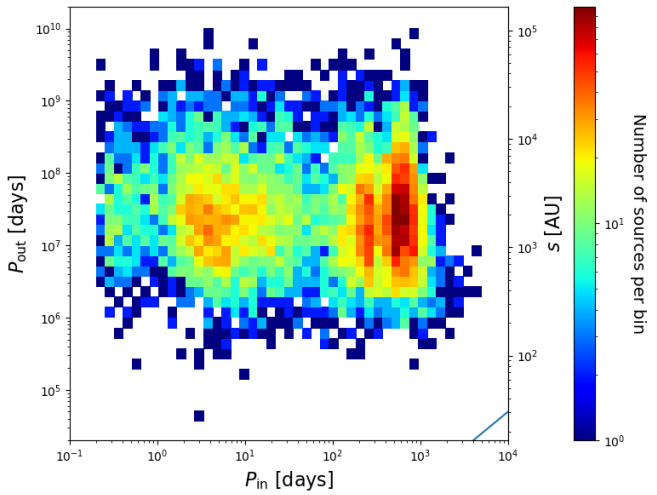

Fig. 53. Distribution of outer vs inner periods for triple systems found in El-Badry catalogue. Left scale: period, right scale: separation. The line, bottom right, shows the limit $P_{out} = 5\ P_{in}$.

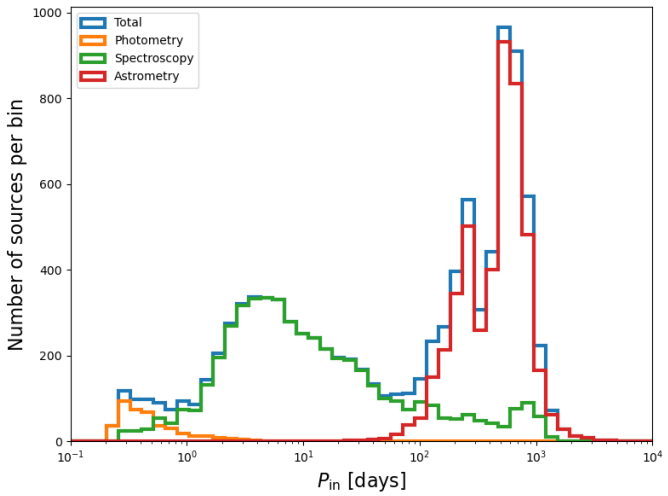

Fig. 54. Distribution of inner periods for triple systems found in El-Badry catalogue.

Figure 53 shows the distribution of the outer vs inner periods for the triple systems found in El-Badry catalogue, where the outer period P_{out} is computed from the separation s (provided in El-Badry catalogue) as $P_{out} = \sqrt{s^3/7.496 \times 10^{-6}(\mathcal{M}_1 + \mathcal{M}_2)}$ and assuming $\mathcal{M}_1 + \mathcal{M}_2 = 1.5\ \mathcal{M}_\odot$, while the inner period P_{in} is the period in the NSS solution.

The drop in the distribution for separations below 200 au is certainly due to selection effects introduced by the processing due to the blending of the two components in a large range of scanning angles. The cut at longer inner periods is dictated by the limited baseline of *Gaia* observations. The shortening of the maximum inner period with the increase of separation, is due to the fact that sources at large separations are also at larger distances, where the astrometric signal of the internal orbit drops.

We note from Fig. 53 that the distribution of the inner period is multimodal. As shown in Fig. 54, this is in part due to the different methods of orbital detection (highlighted with different colours). However, if we compare the distribution of spectroscopic solutions in this sample with respect to the whole NSS solutions (Fig. 2), we can see that the overabundance of solutions with 2 days $< P_{in} <$ 30 days is real. This overabundance is also visible in the Multiple Star catalogue by Tokovinin (2018), figure 7. Tokovinin (2004) attributed the overdensity he observed at $P_{in} < 7$ days to dynamical interaction between the orbits and consequent tidal interaction within the inner couple, as suggested by Kiseleva et al. (1998).

This short analysis shows that the study of multiple systems will greatly benefit from the results of the NSS catalogue.

10. Conclusions

On 24 April 1610, Galileo brought his telescope to demonstrate its performances to his opponents and other scholars in Bologna. Martin Horký, Kepler's student writes: "*I tested the instrument of Galileo's in a thousands ways*"..., "*below it works wonderfully; in the heavens, it deceives one as some fixed stars are seen double.*" (Feyerabend 1970). This is how the discovery of first telescopic double stars failed and how easy it is to consider that facts can be contradicted by one's prejudices.

Four hundreds and twelve years later, the validations and the results obtained so far suggest that NSS entries in *Gaia* DR3 are

binaries, not *Gaia* telescope artefacts, although to be fair, it is also expected that this catalogue contains spurious solutions. We thus need to start this conclusion by stressing that the counterpart of so large a material is some unavoidable contamination that should be kept in mind when analysing the results.

In particular the selection of distribution tails (e.g. small periods, small or large mass functions) is likely to preferentially select the wrong solutions, as happened to us in the course of this verification paper. The abundant partially resolved sources and their impact on the astrometry and epoch radial velocities conspire with the scanning law periodic motions to produce solutions that look like bona fide unresolved binaries. To cope with this, increasing the threshold on the significance of the solutions appears satisfactory but may well represent a Pyrrhic victory, as this decreases drastically the sample sizes.

The NSS catalogue is already the result of a drastic selection of sources. The impact of the total selection effects due successively to the input list, to the data processing, and posterior source filtering need to be taken into account, and the statistical studies of the NSS sample will require dedicated studies. This has not been attempted here, although the main points have probably been mentioned. There are subjects which are already known to represent pitfalls, for example the acceleration solutions which should not be used for physical interpretations.

Although the main impact of the NSS catalogue originates from the simultaneous presence of the main kind of binaries, and consequently an impressive coverage of binary periods, the novelty is mainly brought by the exquisite astrometric precision, allowing the detection of many astrometric binaries. There is however one strength and one weakness concerning astrometric orbits: if the astrometric and the photometric effects are not decoupled, the actual size of the orbit of the primary cannot be found. This is difficult, but when this can be done, then both masses and luminosities of the components become available. Masses that have been estimated here try to take this into account, but the combination with external data, as some examples have shown, will prove very useful if not sometimes mandatory.

Using either astrometric orbits, spectroscopic orbits, or both, the whole H-R diagram can be studied with an abundant material. Obviously, some analyses may be more interesting than others. Here, new ultracool dwarf binaries are found, and the small mass ratios can also be studied down to the substellar domain. True masses are found for substellar companions and two new super-Jupiter candidates may have been found. Twin degenerates and one WD hosting a super-Jupiter companion are also proposed. Concerning compact companions with larger masses, potential companions are present in the mass range of neutron stars or black holes, but which may also be Algol or triple systems: indeed, at this step, we stress that most findings here should be considered as tentative; although verifications have been done, further analyses are warranted. The eccentricity-period relation will also undoubtedly be under scrutiny although interesting substructures for giants are already shown here. The detection of ellipsoidal variables mistaken as long-period variables, or the detection of sources found in a rare evolutionary stage like EL CVn, underlines the potential of acquiring both photometric and orbital data. This is another testimony that *Gaia* is an impressively complete observatory in orbit.

Without any detailed content study nor modelling, that will be the work of the scientific exploitation to come, the multiple topics tackled in the sections above, while only a very preliminary, tentative exploration of the *Gaia* DR3 binaries, clearly demonstrate its scientific potential. Paraphrasing Aaron Levenstein about statistics, what these analyses reveal is suggestive, what they conceal may be essential.

Acknowledgements. This work is dedicated to the memory of our late colleague Dimitri Pourbaix who suggested the title of this article. He had been for many years leader of the Gaia CU4 Coordination Unit and passed away before seeing the Gaia DR3 NSS outcome. This catalogue will remain in a large part the testimony of his involvement.
We would like to thank the referee Andrei Tokovinin, and the DPAC reporter, Lennart Lindegren, for their useful suggestions.
This work presents results from the European Space Agency (ESA) space mission *Gaia*. *Gaia* data are being processed by the *Gaia* Data Processing and Analysis Consortium (DPAC). Funding for the DPAC is provided by national institutions, in particular the institutions participating in the *Gaia* MultiLateral Agreement (MLA). The *Gaia* mission website is `https://www.cosmos.esa.int/gaia`. The *Gaia* archive website is `https://archives.esac.esa.int/gaia`. Further acknowledgements are given in Appendix A.
This publication has also made use of observations collected with the SOPHIE spectrograph on the 1.93-m telescope at Observatoire de Haute-Provence (CNRS), France (program 21B.PNPS.AREN) using support by the French Programme National de Physique Stellaire (PNPS). We thank all the staff of Haute-Provence Observatory for their support at the 1.93-m telescope and on SOPHIE. Observations have also been obtained with the Mercator Telescope and the HERMES spectrograph, which is supported by the Research Foundation – Flanders (FWO), Belgium, the Research Council of KULeuven, Belgium, the Fonds National de la Recherche Scientifique (F.R.S.-FNRS), Belgium, the Royal Observatory of Belgium, the Observatoire de Genève, Switzerland and the Thüringer Landessternwarte Tautenburg, Germany.
This project has received funding from the European Research Council (ERC) under the European Union's Horizon 2020 research and innovation programme (grant agreement No. [951549]). Ts.M. research was supported by Grant No. 2016069 of the United States-Israel Binational Science Foundation (BSF) and by Grant No. I-1498-303.7/2019 of the German-Israeli Foundation for Scientific Research and Development (GIF).

References

Adibekyan, V. 2019, Geosciences, 9, 105
Ahn, C. P., Alexandroff, R., Allende Prieto, C., et al. 2012, ApJS, 203, 21
Albareti, F. D., Allende Prieto, C., Almeida, A., et al. 2017, ApJS, 233, 25
Alvarez, R., Jorissen, A., Plez, B., et al. 2001, A&A, 379, 305
Anders, F., Khalatyan, A., Queiroz, A. B. A., et al. 2022, A&A, 658, A91
Arenou, F., Halbwachs, J.-L., Mayor, M., Palasi, J., & Udry, S. 2000, IAU Symposium, 200, 135
Arriagada, P., Butler, R. P., Minniti, D., et al. 2010, ApJ, 711, 1229
Artigau, É., Gagné, J., Faherty, J., et al. 2015, ApJ, 806, 254
Astropy Collaboration, Price-Whelan, A., Sipőcz, B. M., et al. 2018, AJ, 156, 123
Avvakumova, E. A., Malkov, O. Y., & Kniazev, A. Y. 2013, Astronomische Nachrichten, 334, 860
Babusiaux, C., Fabricius, C., & et al. 2022, A&A, submitted
Bardalez Gagliuffi, D. C., Burgasser, A. J., Gelino, C. R., et al. 2014, ApJ, 794, 143
Barstow, M. A., Bond, H. E., Burleigh, M. R., & Holberg, J. B. 2001, MNRAS, 322, 891
Barstow, M. A., Bond, H. E., Holberg, J. B., et al. 2005, MNRAS, 362, 1134
Barstow, M. A., Holberg, J. B., Fleming, T. A., et al. 1994, MNRAS, 270, 499
Belokurov, V., Penoyre, Z., Oh, S., et al. 2020, MNRAS, 496, 1922
Benedict, G. F., McArthur, B. E., Forveille, T., et al. 2002, ApJ, 581, L115
Bessel, F. W. 1844, MNRAS, 6, 136
Blackman, J. W., Beaulieu, J. P., Bennett, D. P., et al. 2021, Nature, 598, 272
Blake, C. H., Charbonneau, D., & White, R. J. 2010, ApJ, 723, 684
Blake, C. H., Charbonneau, D., White, R. J., et al. 2008, ApJ, 678, L125
Boch, T. & Fernique, P. 2014, in Astronomical Society of the Pacific Conference Series, Vol. 485, Astronomical Data Analysis Software and Systems XXIII, ed. N. Manset & P. Forshay, 277
Bond, H. E., Schaefer, G. H., Gilliland, R. L., et al. 2017, ApJ, 840, 70
Bonfils, X., Delfosse, X., Udry, S., et al. 2013, A&A, 549, A109
Bonnarel, F., Fernique, P., Bienaymé, O., et al. 2000, A&AS, 143, 33
Boubert, D., Strader, J., Aguado, D., et al. 2019, MNRAS, 486, 2618
Bouchy, F., Hébrard, G., Udry, S., et al. 2009, A&A, 505, 853
Bowler, B. P., Liu, M. C., Shkolnik, E. L., & Tamura, M. 2015, ApJS, 216, 7
Brandt, T. D. 2021, ApJS, 254, 42
Brandt, T. D., Dupuy, T. J., Bowler, B. P., et al. 2020, AJ, 160, 196
Bransgrove, A., Levin, Y., & Beloborodov, A. 2018, MNRAS, 473, 2771
Breddels, M. A. & Veljanoski, J. 2018, A&A, 618, A13
Breivik, K., Chatterjee, S., & Larson, S. L. 2017, ApJ, 850, L13

Bressan, A., Marigo, P., Girardi, L., et al. 2012, MNRAS, 427, 127
Breton, R. P., Rappaport, S. A., van Kerkwijk, M. H., & Carter, J. A. 2012, ApJ, 748, 115
Burgasser, A. J. & McElwain, M. W. 2006, AJ, 131, 1007
Burgasser, A. J., Reid, I. N., Siegler, N., et al. 2007, Protostars and Planets V, 427
Burrows, A., Hubbard, W. B., Lunine, J. I., & Liebert, J. 2001, Reviews of Modern Physics, 73, 719
Busà, I., Aznar Cuadrado, R., Terranegra, L., Andretta, V., & Gomez, M. T. 2007, A&A, 466, 1089
Butler, R. P., Vogt, S. S., Laughlin, G., et al. 2017, AJ, 153, 208
Butler, R. P., Wright, J. T., Marcy, G. W., et al. 2006, ApJ, 646, 505
Carter, J. A., Rappaport, S., & Fabrycky, D. 2011, ApJ, 728, 139
Casertano, S., Lattanzi, M. G., Sozzetti, A., et al. 2008, A&A, 482, 699
Chabrier, G. 2001, ApJ, 554, 1274
Chambers, K. C., Magnier, E. A., Metcalfe, N., et al. 2016, ArXiv e-prints [arXiv:1612.05560]
Corral-Santana, J. M., Casares, J., Muñoz-Darias, T., et al. 2016, A&A, 587, A61
Correia, A. C. M., Couetdic, J., Laskar, J., et al. 2010, A&A, 511, A21
Creevey, O., Sordo, R., Pailler, F., et al. 2022, A&A, submitted
Cropper, M., Katz, D., Sartoretti, P., et al. 2018, A&A, 616, A5
Cruzalèbes, P., Petrov, R. G., Robbe-Dubois, S., et al. 2019, MNRAS, 490, 3158
Cumming, A., Butler, R. P., Marcy, G. W., et al. 2008, PASP, 120, 531
da Silva, R., Udry, S., Bouchy, F., et al. 2007, A&A, 473, 323
Dahn, C. C., Harris, H. C., Levine, S. E., et al. 2008, ApJ, 686, 548
Dalal, S., Kiefer, F., Hébrard, G., et al. 2021, A&A, 651, A11
De Angeli, F., Weiler, M., Montegriffo, P., & et al. 2022, A&A, submitted
de Grijs, R., Courbin, F., Martínez-Vázquez, C. E., et al. 2017, Space Sci. Rev., 212, 1743
Debes, J. H. & Kilic, M. 2010, in American Institute of Physics Conference Series, ed. K. Werner & T. Rauch, Vol. 1273, 488–491
Debes, J. H., Walsh, K. J., & Stark, C. 2012, ApJ, 747, 148
Decin, L., Montargès, M., Richards, A. M. S., et al. 2020, Science, 369, 1497
Dieterich, S. B., Henry, T. J., Golimowski, D. A., Krist, J. E., & Tanner, A. M. 2012, AJ, 144, 64
Dupuy, T. J. & Liu, M. C. 2011, ApJ, 733, 122
Dupuy, T. J. & Liu, M. C. 2017, ApJS, 231, 15
Dupuy, T. J., Liu, M. C., Best, W. M. J., et al. 2019, AJ, 158, 174
Eddington, A. S. 1913, MNRAS, 73, 359
Eggleton, P. P. 1983, ApJ, 268, 368
El-Badry, K. & Rix, H.-W. 2018, MNRAS, 480, 4884
El-Badry, K., Rix, H.-W., & Heintz, T. M. 2021, MNRAS, 506, 2269
El-Badry, K., Seeburger, R., Jayasinghe, T., et al. 2022, arXiv e-prints, arXiv:2203.06348
Endl, M., Cochran, W. D., Kürster, M., et al. 2006, ApJ, 649, 436
ESA, ed. 1997, ESA Special Publication, Vol. 1200, The HIPPARCOS and TYCHO catalogues. Astrometric and photometric star catalogues derived from the ESA HIPPARCOS Space Astrometry Mission
Escorza, A., Boffin, H. M. J., Jorissen, A., et al. 2019, A&A, 625, C3
Eyer, L., Audard, M., Holl, B., Rimoldini, L., & et al. 2022, A&A, in prep.
Fabian, A. C., Rees, M. J., Stella, L., & White, N. E. 1989, MNRAS, 238, 729
Fabricius, C., Høg, E., Makarov, V. V., et al. 2002, A&A, 384, 180
Faigler, S., Kull, I., Mazeh, T., et al. 2015, ApJ, 815, 26
Faucher-Giguère, C.-A. & Kaspi, V. M. 2006, ApJ, 643, 332
Feng, F., Crane, J. D., Xuesong Wang, S., et al. 2019, ApJS, 242, 25
Feyerabend, P. 1970, in The Nature and Function of Scientific Theories: Essays in Contemporary Science and Philosophy, ed. R. G. Colodny (University of Pittsburgh Press)
Fischer, D. A. & Valenti, J. 2005, ApJ, 622, 1102
Flewelling, H. A., Magnier, E. A., Chambers, K. C., et al. 2020, ApJS, 251, 7
Frankowski, A., Jancart, S., & Jorissen, A. 2007, A&A, 464, 377
Gaia Collaboration, Babusiaux, C., van Leeuwen, F., et al. 2018a, A&A, 616, A10
Gaia Collaboration, Brown, A., Vallenari, A., et al. 2016a, A&A, 595, A2
Gaia Collaboration, Brown, A. G. A., Vallenari, A., et al. 2018b, A&A, 616, A1
Gaia Collaboration, Brown, A. G. A., Vallenari, A., et al. 2021a, A&A, 649, A1
Gaia Collaboration, Prusti, T., de Bruijne, J., et al. 2016b, A&A, 595, A1
Gaia Collaboration, Recio-Blanco, A., Kordopatis, G., et al. 2022a, A&A, accepted
Gaia Collaboration, Smart, R. L., Sarro, L. M., et al. 2021b, A&A, 649, A6
Gaia Collaboration, Vallenari, A., & et al. 2022b, A&A, in prep.
Garcia, E. V., Ammons, S. M., Salama, M., et al. 2017, ApJ, 846, 97
Gelino, C. R. & Burgasser, A. J. 2010, AJ, 140, 110
Gentile Fusillo, N. P., Tremblay, P. E., Cukanovaite, E., et al. 2021, MNRAS, 508, 3877
Gentile Fusillo, N. P., Tremblay, P.-E., Gänsicke, B. T., et al. 2019, MNRAS, 482, 4570
Giammichele, N., Bergeron, P., & Dufour, P. 2012, ApJS, 199, 29
Gilmore, G., Randich, S., Worley, C. C., et al. 2022, A&A in press
González, G. & González, G. 1956, Boletin de los Observatorios Tonantzintla y Tacubaya, 2, 19
Górski, K. M., Hivon, E., Banday, A. J., et al. 2005, ApJ, 622, 759
Gosset, E. 2022, A&A in prep.
Grether, D. & Lineweaver, C. H. 2006, ApJ, 640, 1051
Grieves, N., Ge, J., Thomas, N., et al. 2017, MNRAS, 467, 4264
Groenewegen, M. A. T. 2013, A&A, 550, A70
Guseinov, O. K. & Zel'dovich, Y. B. 1966, Soviet Ast., 10, 251
Halbwachs, J.-L., Pourbaix†, D., Arenou, F., Galluccio, L., & et al. 2022, A&A, in prep.
Hartkopf, W. I., Mason, B. D., & Worley, C. E. 2001, AJ, 122, 3472
Hellier, C., Anderson, D. R., Collier Cameron, A., et al. 2009, Nature, 460, 1098
Henden, A. A., Templeton, M., Terrell, D., et al. 2016, VizieR Online Data Catalogue, 2336
Henry, T. J. & McCarthy, Jr., D. W. 1993, AJ, 106, 773
Herald, D., Gault, D., Anderson, R., et al. 2020, MNRAS, 499, 4570
Hinkle, K. H., Lebzelter, T., Joyce, R. R., & Fekel, F. C. 2002, AJ, 123, 1002
Høg, E., Fabricius, C., Makarov, V. V., et al. 2000, A&A, 355, L27
Holl, B., Fabricius, C., Portell, J., & et al. 2022a, A&A, in prep.
Holl, B., Sozzetti, A., Sahlmann, J., & et al. 2022b, A&A in prep.
Howard, A. W., Marcy, G. W., Johnson, J. A., et al. 2010, Science, 330, 653
Huber, D., Bryson, S. T., Haas, M. R., et al. 2016, ApJS, 224, 2
Hunter, J. D. 2007, Computing In Science & Engineering, 9, 90
Imbert, M. 1996, A&AS, 116, 497
Jones, E., Oliphant, T., Peterson, P., et al. 2001, SciPy: Open source scientific tools for Python
Jorissen, A. 2004, in AGB stars, ed. H. Habing & H. Olofsson, A&A Library (Springer Verlag, New York)
Jorissen, A. & Frankowski, A. 2008, in American Institute of Physics Conference Series, Vol. 1057, Graduate School in Astronomy: XII Special Courses at the National Observatory of Rio de Janeiro, ed. P. Pellegrini, S. Daflon, J. S. Alcaniz, & E. Telles, 1–55
Jorissen, A., Frankowski, A., Famaey, B., & van Eck, S. 2009, A&A, 498, 489
Jorissen, A., Van Eck, S., Merle, T., & Van Winckel, H. 2019, IAU Symposium, 343, 431
Katoh, N., Itoh, Y., Toyota, E., & Sato, B. 2013, AJ, 145, 41
Katz, D., Sartoretti, P., Cropper, M., et al. 2019, A&A, 622, A205
Katz, D., Sartoretti, P., Guerrier, A., & et al. 2022, A&A, in prep.
Kervella, P., Arenou, F., Mignard, F., & Thévenin, F. 2019a, A&A, 623, A72
Kervella, P., Arenou, F., & Thévenin, F. 2022, A&A, 657, A7
Kervella, P., Gallenne, A., Remage Evans, N., et al. 2019b, A&A, 623, A116
Kiefer, F. 2019, A&A, 632, L9
Kiefer, F., Hébrard, G., Lecavelier des Etangs, A., et al. 2021, A&A, 645, A7
Kiefer, F., Hébrard, G., Sahlmann, J., et al. 2019, A&A, 631, A125
Kiseleva, L. G., Eggleton, P. P., & Mikkola, S. 1998, MNRAS, 300, 292
Klüter, J., Bastian, U., & Wambsganss, J. 2020, A&A, 640, A83
Koren, S. C., Blake, C. H., Dahn, C. C., & Harris, H. C. 2016, AJ, 151, 57
Kounkel, M., Covey, K. R., Stassun, K. G., et al. 2021, AJ, 162, 184
Kürster, M., Endl, M., Els, S., et al. 2000, A&A, 353, L33
Lallement, R., Babusiaux, C., Vergely, J. L., et al. 2019, A&A, 625, A135
Lasker, B. M., Lattanzi, M. G., McLean, B. J., et al. 2008, AJ, 136, 735
Latham, D. W., Stefanik, R. P., Mazeh, T., Mayor, M., & Burki, G. 1989, Nature, 339, 38
Lebzelter, T., Trabucchi, M., Mowlavi, N., et al. 2019, A&A, 631, A24
Leverington, D. 1995, A history of astronomy from 1890 to the present (Berlin, New York: Springer)
Lindegren, L. 1997, in ESA Special Publication, Vol. 402, Hipparcos - Venice '97, ed. R. M. Bonnet, E. Høg, P. L. Bernacca, L. Emiliani, A. Blaauw, C. Turon, J. Kovalevsky, L. Lindegren, H. Hassan, M. Bouffard, B. Strim, D. Heger, M. A. C. Perryman, & L. Woltjer, 13–18
Lindegren, L. 2022, Gaia Data Processing and Analysis Consortium (DPAC) technical note GAIA-C3-TN-LU-LL-136-01, http://www.cosmos.esa.int/web/gaia/public-dpac-documents
Lindegren, L., Klioner, S., Hernández, J., et al. 2021, A&A, 649, A2
Luo, A. L., Zhao, Y. H., Zhao, G., et al. 2015, Research in Astronomy and Astrophysics, 15, 1095
Ma, B. & Ge, J. 2014, MNRAS, 439, 2781
Magnier, E. A., Chambers, K. C., Flewelling, H. A., et al. 2020a, ApJS, 251, 3
Magnier, E. A., Schlafly, E. F., Finkbeiner, D. P., et al. 2020b, ApJS, 251, 6
Magnier, E. A., Sweeney, W. E., Chambers, K. C., et al. 2020c, ApJS, 251, 5
Makarov, V. V. & Kaplan, G. H. 2005, AJ, 129, 2420
Marcy, G. W., Butler, R. P., Fischer, D., et al. 2001, ApJ, 556, 296
Marcy, G. W., Butler, R. P., Vogt, S. S., Fischer, D., & Lissauer, J. J. 1998, ApJ, 505, L147
Martin, C., Mignard, F., & Froeschle, M. 1997, A&AS, 122, 571
Mashian, N. & Loeb, A. 2017, MNRAS, 470, 2611
Maxted, P. F. L., Anderson, D. R., Burleigh, M. R., et al. 2011, MNRAS, 418, 1156
Maxted, P. F. L., Bloemen, S., Heber, U., et al. 2014, MNRAS, 437, 1681
Mayor, M., Marmier, M., Lovis, C., et al. 2011, arXiv e-prints, arXiv:1109.2497

Mayor, M., Udry, S., Naef, D., et al. 2004, A&A, 415, 391
Mazeh, T. 2008, in EAS Publications Series, Vol. 29, EAS Publications Series, ed. M. J. Goupil & J. P. Zahn, 1–65
Mortier, A., Santos, N. C., Sozzetti, A., et al. 2012, A&A, 543, A45
Moutou, C., Mayor, M., Lo Curto, G., et al. 2009, A&A, 496, 513
Mowlavi, N., Holl, B., Lecoeur-Tabi, I., Barbian, F., & et al. 2022, A&A, in prep.
Murphy, S. J., Bedding, T. R., & Shibahashi, H. 2016, ApJ, 827, L17
Napiwotzki, R., Karl, C. A., Lisker, T., et al. 2020, A&A, 638, A131
Navarro, S. G., Corradi, R. L. M., & Mampaso, A. 2012, A&A, 538, A76
Nelson, B. E., Robertson, P. M., Payne, M. J., et al. 2016, MNRAS, 455, 2484
Nordström, B., Mayor, M., Andersen, J., et al. 2004, A&A, 418, 989
Ochsenbein, F., Bauer, P., & Marcout, J. 2000, A&AS, 143, 23
Oliphant, T. E. 2007, Computing in Science Engineering, 9, 10
Onken, C. A., Wolf, C., Bessell, M. S., et al. 2019, PASA, 36, e033
Orosz, J. A., McClintock, J. E., Narayan, R., et al. 2007, Nature, 449, 872
Ortiz, R. & Guerrero, M. A. 2021, ApJ, 912, 93
Otero, S. A. 2008, Open European Journal on Variable Stars, 0083, 1
Paczyński, B. 1971, ARA&A, 9, 183
Pecaut, M. J. & Mamajek, E. E. 2013, ApJS, 208, 9
Penoyre, Z., Belokurov, V., & Evans, N. W. 2021, arXiv e-prints, arXiv:2111.10380
Pérez, F. & Granger, B. E. 2007, Computing in Science and Engineering, 9, 21
Pietrzyński, G., Graczyk, D., Gallenne, A., et al. 2019, Nature, 567, 200
Pinamonti, M., Sozzetti, A., Maldonado, J., et al. 2022, arXiv e-prints, arXiv:2203.04648
Pourbaix, D. & et al. 2022, Gaia DR3 documentation Chapter 7: Non-Single Stars, Gaia DR3 documentation
Pourbaix, D., Tokovinin, A. A., Batten, A. H., et al. 2004, A&A, 424, 727
R Core Team. 2013, R: A Language and Environment for Statistical Computing, R Foundation for Statistical Computing, Vienna, Austria
Raghavan, D., McAlister, H. A., Henry, T. J., et al. 2010, ApJS, 190, 1
Randich, S., Gilmore, G., Magrini, L., et al. 2022, A&A in press
Rappaport, S., Nelson, L., Levine, A., et al. 2015, ApJ, 803, 82
Raskin, G., van Winckel, H., Hensberge, H., et al. 2011, A&A, 526, A69
Reback, J., jbrockmendel, McKinney, W., et al. 2022, pandas-dev/pandas: Pandas 1.4.2
Remillard, R. A. & McClintock, J. E. 2006, ARA&A, 44, 49
Ricker, G. R., Winn, J. N., Vanderspek, R., et al. 2015, Journal of Astronomical Telescopes, Instruments, and Systems, 1, 014003
Riello, M., De Angeli, F., Evans, D. W., et al. 2021, A&A, 649, A3
Rivera, E. J., Laughlin, G., Butler, R. P., et al. 2010, ApJ, 719, 890
Rivera, E. J., Lissauer, J. J., Butler, R. P., et al. 2005, ApJ, 634, 625
Robertson, T. H. & Jordan, T. M. 1989, AJ, 98, 1354
Roeser, S., Demleitner, M., & Schilbach, E. 2010, AJ, 139, 2440
Rosenthal, L. J., Fulton, B. J., Hirsch, L. A., et al. 2021, ApJS, 255, 8
Rousseau, J., Martin, N., Prévot, L., et al. 1978, A&AS, 31, 243
Sahai, R., Findeisen, K., Gil de Paz, A., & Sánchez Contreras, C. 2008, ApJ, 689, 1274
Sahlmann, J. 2019, Johannes-Sahlmann/pystrometry
Sahlmann, J., Burgasser, A. J., Bardalez Gagliuffi, D. C., et al. 2020, MNRAS, 495, 1136
Sahlmann, J., Burgasser, A. J., Martín, E. L., et al. 2015, A&A, 579, A61
Sahlmann, J., Dupuy, T. J., Burgasser, A. J., et al. 2021, MNRAS, 500, 5453
Sahlmann, J., Lazorenko, P. F., Ségransan, D., et al. 2014a, Mem. Soc. Astron. Italiana, 85, 674
Sahlmann, J., Lazorenko, P. F., Ségransan, D., et al. 2014b, A&A, 565, A20
Sahlmann, J., Lazorenko, P. F., Ségransan, D., et al. 2013, A&A, 556, A133
Sahlmann, J., Ségransan, D., Queloz, D., et al. 2011, A&A, 525, A95+
Santos, N. C., Mayor, M., Bonfils, X., et al. 2011, A&A, 526, A112
Satō, I., Buie, M., Maley, P. D., et al. 2014, International Journal of Astronomy and Astrophysics, 4, 91
Seabroke, G. M., Fabricius, C., Teyssier, D., et al. 2021, A&A, 653, A160
Shahaf, S., Mazeh, T., Faigler, S., & Holl, B. 2019, MNRAS, 487, 5610
Shao, Y. & Li, X.-D. 2019, ApJ, 885, 151
Siebert, H. 2005, Journal for the History of Astronomy, 36, 251
Siopis, C. 2022, A&A in prep.
Skrutskie, M. F., Cutri, R. M., Stiening, R., et al. 2006, AJ, 131, 1163
Smart, R. L., Marocco, F., Sarro, L. M., et al. 2019, MNRAS, 485, 4423
Söderhjelm, S., Lindegren, L., & Perryman, M. A. C. 1997, in ESA Special Publication, Vol. 402, Hipparcos - Venice '97, ed. R. M. Bonnet, E. Høg, P. L. Bernacca, L. Emiliani, A. Blaauw, C. Turon, J. Kovalevsky, L. Lindegren, H. Hassan, M. Bouffard, B. Strim, D. Heger, M. A. C. Perryman, & L. Woltjer, 251–256
Sousa, S. G., Santos, N. C., Israelian, G., Mayor, M., & Udry, S. 2011, A&A, 533, A141
Sozzetti, A., Torres, G., Latham, D. W., et al. 2009, ApJ, 697, 544
Sozzetti, A., Udry, S., Zucker, S., et al. 2006, A&A, 449, 417
Sperauskas, J., Deveikis, V., & Tokovinin, A. 2019, A&A, 626, A31
Stassun, K. G., Collins, K. A., & Gaudi, B. S. 2017, AJ, 153, 136
Stassun, K. G. & Torres, G. 2021, ApJ, 907, L33
Steinmetz, M., Guiglion, G., McMillan, P. J., et al. 2020a, AJ, 160, 83
Steinmetz, M., Matijevič, G., Enke, H., et al. 2020b, AJ, 160, 82
Subasavage, J. P., Jao, W.-C., Henry, T. J., et al. 2017, AJ, 154, 32
Susemiehl, N. & Meyer, M. R. 2022, A&A, 657, A48
Taylor, M. B. 2005, in Astronomical Society of the Pacific Conference Series, Vol. 347, Astronomical Data Analysis Software and Systems XIV, ed. P. Shopbell, M. Britton, & R. Ebert, 29
Taylor, M. B. 2006, in Astronomical Society of the Pacific Conference Series, Vol. 351, Astronomical Data Analysis Software and Systems XV, ed. C. Gabriel, C. Arviset, D. Ponz, & S. Enrique, 666
Tinney, C. G., Butler, R. P., Marcy, G. W., et al. 2002, ApJ, 571, 528
Tokovinin, A. 2004, in Revista Mexicana de Astronomia y Astrofisica Conference Series, Vol. 21, Revista Mexicana de Astronomia y Astrofisica Conference Series, ed. C. Allen & C. Scarfe, 7–14
Tokovinin, A. 2017, ApJ, 844, 103
Tokovinin, A. 2018, ApJS, 235, 6
Trifonov, T., Kürster, M., Zechmeister, M., et al. 2018, A&A, 609, A117
Trimble, V. L. & Thorne, K. S. 1969, ApJ, 156, 1013
Trumpler, R. J. & Weaver, H. F. 1953, Statistical astronomy (Dover Publication, Inc., New York.)
Udry, S., Mayor, M., Naef, D., et al. 2002, A&A, 390, 267
van Kerkwijk, M. H., Rappaport, S. A., Breton, R. P., et al. 2010, ApJ, 715, 51
van Leeuwen, F. 2007, Hipparcos, the New Reduction of the Raw Data, Astrophysics and Space Science Library. Vol. 350 edn. (Springer)
van Leeuwen, F. 2007, A&A, 474, 653
van Roestel, J., Kupfer, T., Ruiz-Carmona, R., et al. 2018, MNRAS, 475, 2560
Veras, D. 2021, in Oxford Research Encyclopedia of Planetary Science (Oxford University Press), 1
Verbunt, F. & Phinney, E. S. 1995, A&A, 296, 709
Waters, C. Z., Magnier, E. A., Price, P. A., et al. 2020, ApJS, 251, 4
Wenger, M., Ochsenbein, F., Egret, D., et al. 2000, A&AS, 143, 9
Wielen, R., Dettbarn, C., Jahreiß, H., Lenhardt, H., & Schwan, H. 1999, A&A, 346, 675
Wiktorowicz, G., Wyrzykowski, Ł., Chruslinska, M., et al. 2019, ApJ, 885, 1
Wilson, P. A., Hébrard, G., Santos, N. C., et al. 2016, A&A, 588, A144
Winters, J. G., Henry, T. J., Jao, W.-C., et al. 2019, AJ, 157, 216
Winters, J. G., Irwin, J., Newton, E. R., et al. 2018, AJ, 155, 125
Wittenmyer, R. A., Horner, J., Tuomi, M., et al. 2012, ApJ, 753, 169
Zacharias, N., Finch, C., Subasavage, J., et al. 2015, AJ, 150, 101
Zacharias, N., Finch, C. T., Girard, T. M., et al. 2013, AJ, 145, 44
Zahn, J. P. & Bouchet, L. 1989, A&A, 223, 112
Ziolkowski, J. 2014, MNRAS, 440, L61

Appendix A:

The *Gaia* mission and data processing have financially been supported by, in alphabetical order by country:

- the Algerian Centre de Recherche en Astronomie, Astrophysique et Géophysique of Bouzareah Observatory;
- the Austrian Fonds zur Förderung der wissenschaftlichen Forschung (FWF) Hertha Firnberg Programme through grants T359, P20046, and P23737;
- the BELgian federal Science Policy Office (BELSPO) through various PROgramme de Développement d'Expériences scientifiques (PRODEX) grants, the Fonds Wetenschappelijk Onderzoek through grant VS.091.16N, the Fonds de la Recherche Scientifique (FNRS), and the Research Council of Katholieke Universiteit (KU) Leuven through grant C16/18/005 (Pushing AsteRoseismology to the next level with TESS, GaiA, and the Sloan DIgital Sky SurvEy – PARADISE);
- the Brazil-France exchange programmes Fundação de Amparo à Pesquisa do Estado de São Paulo (FAPESP) and Coordenação de Aperfeicoamento de Pessoal de Nível Superior (CAPES) - Comité Français d'Evaluation de la Coopération Universitaire et Scientifique avec le Brésil (COFECUB);
- the Chilean Agencia Nacional de Investigación y Desarrollo (ANID) through Fondo Nacional de Desarrollo Científico y Tecnológico (FONDECYT) Regular Project 1210992 (L. Chemin);
- the National Natural Science Foundation of China (NSFC) through grants 11573054, 11703065, and 12173069, the China Scholarship Council through grant 201806040200, and the Natural Science Foundation of Shanghai through grant 21ZR1474100;
- the Tenure Track Pilot Programme of the Croatian Science Foundation and the École Polytechnique Fédérale de Lausanne and the project TTP-2018-07-1171 'Mining the Variable Sky', with the funds of the Croatian-Swiss Research Programme;
- the Czech-Republic Ministry of Education, Youth, and Sports through grant LG 15010 and INTER-EXCELLENCE grant LTAUSA18093, and the Czech Space Office through ESA PECS contract 98058;
- the Danish Ministry of Science;
- the Estonian Ministry of Education and Research through grant IUT40-1;
- the European Commission's Sixth Framework Programme through the European Leadership in Space Astrometry (ELSA) Marie Curie Research Training Network (MRTN-CT-2006-033481), through Marie Curie project PIOF-GA-2009-255267 (Space AsteroSeismology & RR Lyrae stars, SAS-RRL), and through a Marie Curie Transfer-of-Knowledge (ToK) fellowship (MTKD-CT-2004-014188); the European Commission's Seventh Framework Programme through grant FP7-606740 (FP7-SPACE-2013-1) for the *Gaia* European Network for Improved data User Services (GENIUS) and through grant 264895 for the *Gaia* Research for European Astronomy Training (GREAT-ITN) network;
- the European Cooperation in Science and Technology (COST) through COST Action CA18104 'Revealing the Milky Way with *Gaia* (MW-Gaia)';
- the European Research Council (ERC) through grants 320360, 647208, and 834148 and through the European Union's Horizon 2020 research and innovation and excellent science programmes through Marie Skłodowska-Curie grant 745617 (Our Galaxy at full HD – Gal-HD) and 895174 (The build-up and fate of self-gravitating systems in the Universe) as well as grants 687378 (Small Bodies: Near and Far), 682115 (Using the Magellanic Clouds to Understand the Interaction of Galaxies), 695099 (A sub-percent distance scale from binaries and Cepheids – CepBin), 716155 (Structured ACCREtion Disks – SACCRED), 951549 (Sub-percent calibration of the extragalactic distance scale in the era of big surveys – UniverScale), and 101004214 (Innovative Scientific Data Exploration and Exploitation Applications for Space Sciences – EXPLORE);
- the European Science Foundation (ESF), in the framework of the *Gaia* Research for European Astronomy Training Research Network Programme (GREAT-ESF);
- the European Space Agency (ESA) in the framework of the *Gaia* project, through the Plan for European Cooperating States (PECS) programme through contracts C98090 and 4000106398/12/NL/KML for Hungary, through contract 4000115263/15/NL/IB for Germany, and through PROgramme de Développement d'Expériences scientifiques (PRODEX) grant 4000127986 for Slovenia;
- the Academy of Finland through grants 299543, 307157, 325805, 328654, 336546, and 345115 and the Magnus Ehrnrooth Foundation;
- the French Centre National d'Études Spatiales (CNES), the Agence Nationale de la Recherche (ANR) through grant ANR-10-IDEX-0001-02 for the 'Investissements d'avenir' programme, through grant ANR-15-CE31-0007 for project 'Modelling the Milky Way in the *Gaia* era' (MOD4Gaia), through grant ANR-14-CE33-0014-01 for project 'The Milky Way disc formation in the *Gaia* era' (ARCHEOGAL), through grant ANR-15-CE31-0012-01 for project 'Unlocking the potential of Cepheids as primary distance calibrators' (UnlockCepheids), through grant ANR-19-CE31-0017 for project 'Secular evolution of galaxies' (SEGAL), and through grant ANR-18-CE31-0006 for project 'Galactic Dark Matter' (GaDaMa), the Centre National de la Recherche Scientifique (CNRS) and its SNO *Gaia* of the Institut des Sciences de l'Univers (INSU), its Programmes Nationaux: Cosmologie et Galaxies (PNCG), Gravitation Références Astronomie Métrologie (PNGRAM), Planétologie (PNP), Physique et Chimie du Milieu Interstellaire (PCMI), and Physique Stellaire (PNPS), the 'Action Fédératrice *Gaia*' of the Observatoire de Paris, the Région de Franche-Comté, the Institut National Polytechnique (INP) and the Institut National de Physique nucléaire et de Physique des Particules (IN2P3) co-funded by CNES;
- the German Aerospace Agency (Deutsches Zentrum für Luft- und Raumfahrt e.V., DLR) through grants 50QG0501, 50QG0601, 50QG0602, 50QG0701, 50QG0901, 50QG1001, 50QG1101, 50QG1401, 50QG1402, 50QG1403, 50QG1404, 50QG1904, 50QG2101, 50QG2102, and 50QG2202, and the Centre for Information Services and High Performance Computing (ZIH) at the Technische Universität Dresden for generous allocations of computer time;
- the Hungarian Academy of Sciences through the Lendület Programme grants LP2014-17 and LP2018-7 and the Hungarian National Research, Development, and Innovation Office (NKFIH) through grant KKP-137523 ('SeismoLab');
- the Science Foundation Ireland (SFI) through a Royal Society - SFI University Research Fellowship (M. Fraser);
- the Israel Ministry of Science and Technology through grant 3-18143 and the Tel Aviv University Center for Artificial Intelligence and Data Science (TAD) through a grant;

- the Agenzia Spaziale Italiana (ASI) through contracts I/037/08/0, I/058/10/0, 2014-025-R.0, 2014-025-R.1.2015, and 2018-24-HH.0 to the Italian Istituto Nazionale di Astrofisica (INAF), contract 2014-049-R.0/1/2 to INAF for the Space Science Data Centre (SSDC, formerly known as the ASI Science Data Center, ASDC), contracts I/008/10/0, 2013/030/I.0, 2013-030-I.0.1-2015, and 2016-17-I.0 to the Aerospace Logistics Technology Engineering Company (ALTEC S.p.A.), INAF, and the Italian Ministry of Education, University, and Research (Ministero dell'Istruzione, dell'Università e della Ricerca) through the Premiale project 'MIning The Cosmos Big Data and Innovative Italian Technology for Frontier Astrophysics and Cosmology' (MITiC);
- the Netherlands Organisation for Scientific Research (NWO) through grant NWO-M-614.061.414, through a VICI grant (A. Helmi), and through a Spinoza prize (A. Helmi), and the Netherlands Research School for Astronomy (NOVA);
- the Polish National Science Centre through HARMONIA grant 2018/30/M/ST9/00311 and DAINA grant 2017/27/L/ST9/03221 and the Ministry of Science and Higher Education (MNiSW) through grant DIR/WK/2018/12;
- the Portuguese Fundação para a Ciência e a Tecnologia (FCT) through national funds, grants SFRH/BD/128840/2017 and PTDC/FIS-AST/30389/2017, and work contract DL 57/2016/CP1364/CT0006, the Fundo Europeu de Desenvolvimento Regional (FEDER) through grant POCI-01-0145-FEDER-030389 and its Programa Operacional Competitividade e Internacionalização (COMPETE2020) through grants UIDB/04434/2020 and UIDP/04434/2020, and the Strategic Programme UIDB/00099/2020 for the Centro de Astrofísica e Gravitação (CENTRA);
- the Slovenian Research Agency through grant P1-0188;
- the Spanish Ministry of Economy (MINECO/FEDER, UE), the Spanish Ministry of Science and Innovation (MICIN), the Spanish Ministry of Education, Culture, and Sports, and the Spanish Government through grants BES-2016-078499, BES-2017-083126, BES-C-2017-0085, ESP2016-80079-C2-1-R, ESP2016-80079-C2-2-R, FPU16/03827, PDC2021-121059-C22, RTI2018-095076-B-C22, and TIN2015-65316-P ('Computación de Altas Prestaciones VII'), the Juan de la Cierva Incorporación Programme (FJCI-2015-2671 and IJC2019-04862-I for F. Anders), the Severo Ochoa Centre of Excellence Programme (SEV2015-0493), and MICIN/AEI/10.13039/501100011033 (and the European Union through European Regional Development Fund 'A way of making Europe') through grant RTI2018-095076-B-C21, the Institute of Cosmos Sciences University of Barcelona (ICCUB, Unidad de Excelencia 'María de Maeztu') through grant CEX2019-000918-M, the University of Barcelona's official doctoral programme for the development of an R+D+i project through an Ajuts de Personal Investigador en Formació (APIF) grant, the Spanish Virtual Observatory through project AyA2017-84089, the Galician Regional Government, Xunta de Galicia, through grants ED431B-2021/36, ED481A-2019/155, and ED481A-2021/296, the Centro de Investigación en Tecnologías de la Información y las Comunicaciones (CITIC), funded by the Xunta de Galicia and the European Union (European Regional Development Fund – Galicia 2014-2020 Programme), through grant ED431G-2019/01, the Red Española de Supercomputación (RES) computer resources at MareNostrum, the Barcelona Supercomputing Centre - Centro Nacional de Supercomputación (BSC-CNS) through activities AECT-2017-2-0002, AECT-2017-3-0006, AECT-2018-1-0017, AECT-2018-2-0013, AECT-2018-3-0011, AECT-2019-1-0010, AECT-2019-2-0014, AECT-2019-3-0003, AECT-2020-1-0004, and DATA-2020-1-0010, the Departament d'Innovació, Universitats i Empresa de la Generalitat de Catalunya through grant 2014-SGR-1051 for project 'Models de Programació i Entorns d'Execució Parallels' (MPEXPAR), and Ramon y Cajal Fellowship RYC2018-025968-I funded by MICIN/AEI/10.13039/501100011033 and the European Science Foundation ('Investing in your future');
- the Swedish National Space Agency (SNSA/Rymdstyrelsen);
- the Swiss State Secretariat for Education, Research, and Innovation through the Swiss Activités Nationales Complémentaires and the Swiss National Science Foundation through an Eccellenza Professorial Fellowship (award PCEFP2_194638 for R. Anderson);
- the United Kingdom Particle Physics and Astronomy Research Council (PPARC), the United Kingdom Science and Technology Facilities Council (STFC), and the United Kingdom Space Agency (UKSA) through the following grants to the University of Bristol, the University of Cambridge, the University of Edinburgh, the University of Leicester, the Mullard Space Sciences Laboratory of University College London, and the United Kingdom Rutherford Appleton Laboratory (RAL): PP/D006511/1, PP/D006546/1, PP/D006570/1, ST/I000852/1, ST/J005045/1, ST/K00056X/1, ST/K000209/1, ST/K000756/1, ST/L006561/1, ST/N000595/1, ST/N000641/1, ST/N000978/1, ST/N001117/1, ST/S000089/1, ST/S000976/1, ST/S000984/1, ST/S001123/1, ST/S001948/1, ST/S001980/1, ST/S002103/1, ST/V000969/1, ST/W002469/1, ST/W002493/1, ST/W002671/1, ST/W002809/1, and EP/V520342/1.

The *Gaia* project and data processing have made use of:

- the Set of Identifications, Measurements, and Bibliography for Astronomical Data (SIMBAD, Wenger et al. 2000), the 'Aladin sky atlas' (Bonnarel et al. 2000; Boch & Fernique 2014), and the VizieR catalogue access tool (Ochsenbein et al. 2000), all operated at the Centre de Données astronomiques de Strasbourg (CDS);
- the National Aeronautics and Space Administration (NASA) Astrophysics Data System (ADS);
- the SPace ENVironment Information System (SPENVIS), initiated by the Space Environment and Effects Section (TEC-EES) of ESA and developed by the Belgian Institute for Space Aeronomy (BIRA-IASB) under ESA contract through ESA's General Support Technologies Programme (GSTP), administered by the BELgian federal Science Policy Office (BELSPO);
- the software products TOPCAT, STIL, and STILTS (Taylor 2005, 2006);
- Matplotlib (Hunter 2007);
- IPython (Pérez & Granger 2007);
- Astropy, a community-developed core Python package for Astronomy (Astropy Collaboration et al. 2018);
- SCIPY (Jones et al. 2001),
- NUMPY (Oliphant 2007),
- PANDAS (Reback et al. 2022),
- R (R Core Team 2013);

- Vaex (Breddels & Veljanoski 2018);
- the Hipparcos-2 catalogue (van Leeuwen 2007). The Hipparcos and *Tycho* catalogues were constructed under the responsibility of large scientific teams collaborating with ESA. The Consortia Leaders were Lennart Lindegren (Lund, Sweden: NDAC) and Jean Kovalevsky (Grasse, France: FAST), together responsible for the Hipparcos Catalogue; Erik Høg (Copenhagen, Denmark: TDAC) responsible for the *Tycho* Catalogue; and Catherine Turon (Meudon, France: INCA) responsible for the Hipparcos Input Catalogue (HIC);
- the *Tycho*-2 catalogue (Høg et al. 2000), the construction of which was supported by the Velux Foundation of 1981 and the Danish Space Board;
- The *Tycho* double star catalogue (TDSC, Fabricius et al. 2002), based on observations made with the ESA Hipparcos astrometry satellite, as supported by the Danish Space Board and the United States Naval Observatory through their double-star programme;
- data products from the Two Micron All Sky Survey (2MASS, Skrutskie et al. 2006), which is a joint project of the University of Massachusetts and the Infrared Processing and Analysis Center (IPAC) / California Institute of Technology, funded by the National Aeronautics and Space Administration (NASA) and the National Science Foundation (NSF) of the USA;
- the ninth data release of the AAVSO Photometric All-Sky Survey (APASS, Henden et al. 2016), funded by the Robert Martin Ayers Sciences Fund;
- the first data release of the Pan-STARRS survey (Chambers et al. 2016; Magnier et al. 2020a; Waters et al. 2020; Magnier et al. 2020c,b; Flewelling et al. 2020). The Pan-STARRS1 Surveys (PS1) and the PS1 public science archive have been made possible through contributions by the Institute for Astronomy, the University of Hawaii, the Pan-STARRS Project Office, the Max-Planck Society and its participating institutes, the Max Planck Institute for Astronomy, Heidelberg and the Max Planck Institute for Extraterrestrial Physics, Garching, The Johns Hopkins University, Durham University, the University of Edinburgh, the Queen's University Belfast, the Harvard-Smithsonian Center for Astrophysics, the Las Cumbres Observatory Global Telescope Network Incorporated, the National Central University of Taiwan, the Space Telescope Science Institute, the National Aeronautics and Space Administration (NASA) through grant NNX08AR22G issued through the Planetary Science Division of the NASA Science Mission Directorate, the National Science Foundation through grant AST-1238877, the University of Maryland, Eotvos Lorand University (ELTE), the Los Alamos National Laboratory, and the Gordon and Betty Moore Foundation;
- the second release of the Guide Star Catalogue (GSC2.3, Lasker et al. 2008). The Guide Star Catalogue II is a joint project of the Space Telescope Science Institute (STScI) and the Osservatorio Astrofisico di Torino (OATo). STScI is operated by the Association of Universities for Research in Astronomy (AURA), for the National Aeronautics and Space Administration (NASA) under contract NAS5-26555. OATo is operated by the Italian National Institute for Astrophysics (INAF). Additional support was provided by the European Southern Observatory (ESO), the Space Telescope European Coordinating Facility (STECF), the International GEMINI project, and the European Space Agency (ESA) Astrophysics Division (nowadays SCI-S);
- the eXtended, Large (XL) version of the catalogue of Positions and Proper Motions (PPM-XL, Roeser et al. 2010);
- data products from the Wide-field Infrared Survey Explorer (WISE), which is a joint project of the University of California, Los Angeles, and the Jet Propulsion Laboratory/California Institute of Technology, and NEOWISE, which is a project of the Jet Propulsion Laboratory/California Institute of Technology. WISE and NEOWISE are funded by the National Aeronautics and Space Administration (NASA);
- the first data release of the United States Naval Observatory (USNO) Robotic Astrometric Telescope (URAT-1, Zacharias et al. 2015);
- the fourth data release of the United States Naval Observatory (USNO) CCD Astrograph Catalogue (UCAC-4, Zacharias et al. 2013);
- the sixth and final data release of the Radial Velocity Experiment (RAVE DR6, Steinmetz et al. 2020a,b). Funding for RAVE has been provided by the Leibniz Institute for Astrophysics Potsdam (AIP), the Australian Astronomical Observatory, the Australian National University, the Australian Research Council, the French National Research Agency, the German Research Foundation (SPP 1177 and SFB 881), the European Research Council (ERC-StG 240271 Galactica), the Istituto Nazionale di Astrofisica at Padova, the Johns Hopkins University, the National Science Foundation of the USA (AST-0908326), the W.M. Keck foundation, the Macquarie University, the Netherlands Research School for Astronomy, the Natural Sciences and Engineering Research Council of Canada, the Slovenian Research Agency, the Swiss National Science Foundation, the Science & Technology Facilities Council of the UK, Opticon, Strasbourg Observatory, and the Universities of Basel, Groningen, Heidelberg, and Sydney. The RAVE website is at `https://www.rave-survey.org/`;
- the first data release of the Large sky Area Multi-Object Fibre Spectroscopic Telescope (LAMOST DR1, Luo et al. 2015);
- the K2 Ecliptic Plane Input Catalogue (EPIC, Huber et al. 2016);
- the ninth data release of the Sloan Digitial Sky Survey (SDSS DR9, Ahn et al. 2012). Funding for SDSS-III has been provided by the Alfred P. Sloan Foundation, the Participating Institutions, the National Science Foundation, and the United States Department of Energy Office of Science. The SDSS-III website is `http://www.sdss3.org/`. SDSS-III is managed by the Astrophysical Research Consortium for the Participating Institutions of the SDSS-III Collaboration including the University of Arizona, the Brazilian Participation Group, Brookhaven National Laboratory, Carnegie Mellon University, University of Florida, the French Participation Group, the German Participation Group, Harvard University, the Instituto de Astrofísica de Canarias, the Michigan State/Notre Dame/JINA Participation Group, Johns Hopkins University, Lawrence Berkeley National Laboratory, Max Planck Institute for Astrophysics, Max Planck Institute for Extraterrestrial Physics, New Mexico State University, New York University, Ohio State University, Pennsylvania State University, University of Portsmouth, Princeton University, the Spanish Participation Group, University of Tokyo, University of Utah, Vanderbilt University, University of Virginia, University of Washington, and Yale University;
- the thirteenth release of the Sloan Digital Sky Survey (SDSS DR13, Albareti et al. 2017). Funding for SDSS-IV has been provided by the Alfred P. Sloan Foundation, the United States Department of Energy Office of Science, and the Participating Institutions. SDSS-IV acknowledges support and

resources from the Center for High-Performance Computing at the University of Utah. The SDSS web site is https://www.sdss.org/. SDSS-IV is managed by the Astrophysical Research Consortium for the Participating Institutions of the SDSS Collaboration including the Brazilian Participation Group, the Carnegie Institution for Science, Carnegie Mellon University, the Chilean Participation Group, the French Participation Group, Harvard-Smithsonian Center for Astrophysics, Instituto de Astrofísica de Canarias, The Johns Hopkins University, Kavli Institute for the Physics and Mathematics of the Universe (IPMU) / University of Tokyo, the Korean Participation Group, Lawrence Berkeley National Laboratory, Leibniz Institut für Astrophysik Potsdam (AIP), Max-Planck-Institut für Astronomie (MPIA Heidelberg), Max-Planck-Institut für Astrophysik (MPA Garching), Max-Planck-Institut für Extraterrestrische Physik (MPE), National Astronomical Observatories of China, New Mexico State University, New York University, University of Notre Dame, Observatário Nacional / MCTI, The Ohio State University, Pennsylvania State University, Shanghai Astronomical Observatory, United Kingdom Participation Group, Universidad Nacional Autónoma de México, University of Arizona, University of Colorado Boulder, University of Oxford, University of Portsmouth, University of Utah, University of Virginia, University of Washington, University of Wisconsin, Vanderbilt University, and Yale University;

- the second release of the SkyMapper catalogue (SkyMapper DR2, Onken et al. 2019, Digital Object Identifier 10.25914/5ce60d31ce759). The national facility capability for SkyMapper has been funded through grant LE130100104 from the Australian Research Council (ARC) Linkage Infrastructure, Equipment, and Facilities (LIEF) programme, awarded to the University of Sydney, the Australian National University, Swinburne University of Technology, the University of Queensland, the University of Western Australia, the University of Melbourne, Curtin University of Technology, Monash University, and the Australian Astronomical Observatory. SkyMapper is owned and operated by The Australian National University's Research School of Astronomy and Astrophysics. The survey data were processed and provided by the SkyMapper Team at the Australian National University. The SkyMapper node of the All-Sky Virtual Observatory (ASVO) is hosted at the National Computational Infrastructure (NCI). Development and support the SkyMapper node of the ASVO has been funded in part by Astronomy Australia Limited (AAL) and the Australian Government through the Commonwealth's Education Investment Fund (EIF) and National Collaborative Research Infrastructure Strategy (NCRIS), particularly the National eResearch Collaboration Tools and Resources (NeCTAR) and the Australian National Data Service Projects (ANDS);
- the *Gaia*-ESO Public Spectroscopic Survey (GES, Gilmore et al. 2022; Randich et al. 2022). The *Gaia*-ESO Survey is based on data products from observations made with ESO Telescopes at the La Silla Paranal Observatory under programme ID 188.B-3002. Public data releases are available through the ESO Science Portal. The project has received funding from the Leverhulme Trust (project RPG-2012-541), the European Research Council (project ERC-2012-AdG 320360-Gaia-ESO-MW), and the Istituto Nazionale di Astrofisica, INAF (2012: CRA 1.05.01.09.16; 2013: CRA 1.05.06.02.07).

The GBOT programme uses observations collected at (i) the European Organisation for Astronomical Research in the Southern Hemisphere (ESO) with the VLT Survey Telescope (VST), under ESO programmes 092.B-0165, 093.B-0236, 094.B-0181, 095.B-0046, 096.B-0162, 097.B-0304, 098.B-0030, 099.B-0034, 0100.B-0131, 0101.B-0156, 0102.B-0174, and 0103.B-0165; and (ii) the Liverpool Telescope, which is operated on the island of La Palma by Liverpool John Moores University in the Spanish Observatorio del Roque de los Muchachos of the Instituto de Astrofísica de Canarias with financial support from the United Kingdom Science and Technology Facilities Council, and (iii) telescopes of the Las Cumbres Observatory Global Telescope Network.

Appendix B: Parameters describing the orbital motion

The parameters relative to the orbital motion as presented in the nss_two_body_orbit are introduced in what follows. More details can be found in the online documentation and articles accompanying the data release Halbwachs et al. (2022); Holl et al. (2022b); Gosset (2022); Siopis (2022) for astrometric, spectroscopic, and eclipsing binaries respectively.

Appendix B.1: Astrometry

The *Gaia* along-scan astrometric measurement w (abscissa) for a binary system can be modelled by the combination of a single-source model $w_{\rm ss}$, describing the standard astrometric motion of the system's barycentre, and a Keplerian model $w_{\rm k1}$.
The single-source model can be written as

$$w_{\rm ss} = (\Delta\alpha^\star + \mu_{\alpha^\star}\, t)\, \sin\psi + (\Delta\delta + \mu_\delta\, t)\, \cos\psi + \varpi\, f_\varpi, \tag{B.1}$$

where $\Delta\alpha^\star = \Delta\alpha\cos\delta$ and $\Delta\delta$ are small offsets in equatorial coordinates from some fixed reference point, $\mu_{\alpha^\star}$, μ_δ are proper motions in these coordinates, t is time, ϖ is the parallax, f_ϖ is the parallax factor, and ψ is the scan angle. The astrometric motion corresponding to a Keplerian orbit of a binary system has generally seven independent parameters, the Campbell elements. These are the period P, the epoch of periastron passage T_0, the eccentricity e, the inclination i, the ascending node Ω, the argument of periastron ω, and the semi-major axis of the photocentre a_0. The Thiele-Innes coefficients A, B, F, G are defined as

$$\begin{aligned} A &= a_0\,(\cos\omega\cos\Omega - \sin\omega\sin\Omega\cos i) \\ B &= a_0\,(\cos\omega\sin\Omega + \sin\omega\cos\Omega\cos i) \\ F &= -a_0\,(\sin\omega\cos\Omega + \cos\omega\sin\Omega\cos i) \\ G &= -a_0\,(\sin\omega\sin\Omega - \cos\omega\cos\Omega\cos i). \end{aligned} \tag{B.2}$$

The elliptical rectangular coordinates X and Y are functions of eccentric anomaly E and eccentricity:

$$E - e\sin E = \frac{2\pi}{P}(t - T_0) \tag{B.3}$$

$$X = \cos E - e \tag{B.4}$$

$$Y = \sqrt{1-e^2}\sin E\ . \tag{B.5}$$

The single Keplerian model can then be written as

$$w_{\rm k1} = (B\,X + G\,Y)\sin\psi + (A\,X + F\,Y)\cos\psi. \tag{B.6}$$

The combined model $w^{(\rm model)}$ for the *Gaia* along-scan astrometry is

$$\begin{aligned} w^{(\rm model)} &= w_{\rm ss} + w_{\rm k1} \\ &= (\Delta\alpha^\star + \mu_{\alpha^\star}\, t)\, \sin\psi + (\Delta\delta + \mu_\delta\, t)\, \cos\psi + \varpi\, f_\varpi \\ &\quad + (B\,X + G\,Y)\sin\psi + (A\,X + F\,Y)\cos\psi. \end{aligned} \tag{B.7}$$

This model has been extensively used for modelling the Hipparcos epoch data of non-single stars (e.g. Sahlmann et al. 2011).

Appendix B.2: Spectroscopy

The radial motion of the primary is given by

$$\mathrm{RV}_1(t) \;=\; \gamma \;+\; K_1\,[\cos(v(t)+\omega) \;+\; e\,\cos(\omega)\,], \tag{B.8}$$

with $v(t)$ the true anomaly deriving from the eccentric anomaly E by

$$\tan\frac{v}{2} \;=\; \sqrt{\frac{1+e}{1-e}}\;\tan\frac{E}{2}, \tag{B.9}$$

and with the semi-amplitude of the primary (resp. secondary)

$$K_{1,2} = \frac{\kappa}{P}\frac{a_{1,2}\sin i}{\sqrt{1-e^2}}, \tag{B.10}$$

where $\kappa \sim 10879$ when K_i is expressed in $\mathrm{km\,s^{-1}}$, P in days and a_i the semi-major axis of the primary (resp. secondary) in au.

This model has been used to produce the NSS solutions for `SB1` and `SB2`. When astrometry and spectroscopy have been combined (`AstroSpectroSB1` solutions), in order to avoid correlations with the Campbell elements, it was easier to complete the Thiele-Innes elements with

$$\begin{aligned} C &= +a_1\sin\omega\sin i \\ H &= +a_1\cos\omega\sin i, \end{aligned} \tag{B.11}$$

and these parameters have been published instead.

Appendix C: Analytic orbit detection sensitivity as a function of orbit inclination

Our toy orbit model is shown in Fig. C.1. To keep the expressions simple we aligned the ellipse major-axis a with α^* and introduced the inclination as rotation around the α^*-axis. The orbital-phase (ϕ)-dependent position $(x(t), y(t))$ is projected to the on-sky position α^*, δ via:

$$\alpha^*(\phi) \;=\; x(\phi) \;\;\;\;\;\;\;\; = a\,\sin\phi \tag{C.1}$$

$$\delta(\phi) \;=\; y(\phi)\,\cos i \;\; = b\,\cos\phi\,\cos i \tag{C.2}$$

The orbit signal in the along-scan (AL, i.e. along ψ) and across-scan (AC, rotated 90 degrees counter-clockwise) directions is

$$\boldsymbol{d}_{\mathrm{AL}} \;=\; \begin{pmatrix}\alpha^*(\phi)\\ \delta\;(\phi)\end{pmatrix}\begin{pmatrix}\sin\psi\\ \cos\psi\end{pmatrix}^T \tag{C.3}$$

$$\boldsymbol{d}_{\mathrm{AC}} \;=\; \begin{pmatrix}\alpha^*(\phi)\\ \delta\;(\phi)\end{pmatrix}\begin{pmatrix}-\cos\psi\\ \sin\psi\end{pmatrix}^T \tag{C.4}$$

To derive the RMS of $\boldsymbol{d}_{\mathrm{AL}}$ and $\boldsymbol{d}_{\mathrm{AC}}$, we make the following simplifying assumptions: (a) The orbit is circular, i.e. $a = b$: The angular velocity $\dot{\phi}$ is constant and integration over ϕ is straightforward. (b) At each observation the orbital phase ϕ is random: The orbital-average value can be obtained by simply integrating over ϕ. (c) At each observation the scan-angle ψ is random. The mean square amplitude of $\boldsymbol{d}_{\mathrm{AL}}$ for a given scan angle ψ under assumptions (a) and (b) reduces to

$$\begin{aligned} \hat{d}^2_{\mathrm{AL},\psi} &= \frac{1}{2\pi}\int_0^{2\pi} \|\boldsymbol{d}_{\mathrm{AL}}\|^2\; d\phi \\ &= \frac{1}{2\pi}\int_0^{2\pi} (a\,\sin\phi\,\sin\psi + a\,\cos\phi\,\cos i\,\cos\psi)^2\; d\phi \\ &= \frac{a^2}{2}\left(\sin^2\psi + \cos^2\psi\cos^2 i\right), \end{aligned} \tag{C.5}$$

where we used the identity

$$\int_0^{2\pi} (u\,\sin x + v\,\cos x)^2\; dx = \pi\left(u^2+v^2\right). \tag{C.6}$$

Similarly we obtain in the AC direction

$$\hat{d}^2_{\mathrm{AC},\psi} = \frac{a^2}{2}\left(\cos^2\psi + \sin^2\psi\cos^2 i\right). \tag{C.7}$$

Applying assumption (c) we get

$$\begin{aligned} \hat{d}^2_{\mathrm{AL}} &= \frac{1}{2\pi}\int_0^{2\pi} \hat{d}^2_{\mathrm{AL},\psi}\; d\psi \\ &= \frac{a^2}{4\pi}\int_0^{2\pi} \sin^2\psi + \cos^2\psi\cos^2 i\; d\psi \\ &= \frac{a^2}{4}\left(1+\cos^2 i\right) \end{aligned} \tag{C.8}$$

and in AC

$$\hat{d}^2_{\mathrm{AC}} = \frac{a^2}{4}\left(1+\cos^2 i\right). \tag{C.9}$$

Assuming constant weights W_{AL} and W_{AC} for the AL and AC observations, respectively, the resulting RMS level is

$$\mathrm{RMS}(i) = \sqrt{\hat{d}^2_{\mathrm{AL}} + \hat{d}^2_{\mathrm{AC}}} = \frac{a}{2}\sqrt{(W_{\mathrm{AL}}+W_{\mathrm{AC}})\,(1+\cos^2 i)}. \tag{C.10}$$

It is instructive to examine the two extreme scenarios:

1. One-dimensional astrometry, i.e. $W_{\mathrm{AL}} = 1$ and $W_{\mathrm{AC}} = 0$, which approximates the *Gaia* DR3 astrometric solution: we obtain

$$\mathrm{RMS}_{1\mathrm{D}}(i) = \frac{a}{2}\;\sqrt{1+\cos^2 i}, \tag{C.11}$$

   which results in a $\sqrt{2}$ reduction for edge-on systems compared to the face-on configuration.
2. Two-dimensional astrometry with equal weights, i.e. $W_{\mathrm{AL}} = W_{\mathrm{AC}} = 1$, which approximates conventional CCD imaging:

$$\mathrm{RMS}_{2\mathrm{D}}(i) = \frac{a}{2}\;\sqrt{2\,(1+\cos^2 i)}, \tag{C.12}$$

   i.e. same inclination-dependency as one-dimensional observations but with a $\sqrt{2}$ boost in RMS because the number of observations is doubled[21].

[21] This two-dimensional case was formally derived with a random rotation of the frame per observation, which does not correspond to fixed-axis orientation CCD observation. In our toy model, the scan-angle integral takes care of considering the random (Ω-)orientation of the orbit since we assumed the rotation axis is aligned with $\alpha^\star$. Alternatively the sky rotation angle reminiscent of Ω could be introduced and integrated over to achieve this averaging, and then there is no need to integrate over scan angle for a fixed orientation telescope. As long as ψ and/or Ω are assumed to be randomly oriented without range restriction, the simpler model used here is accurate.

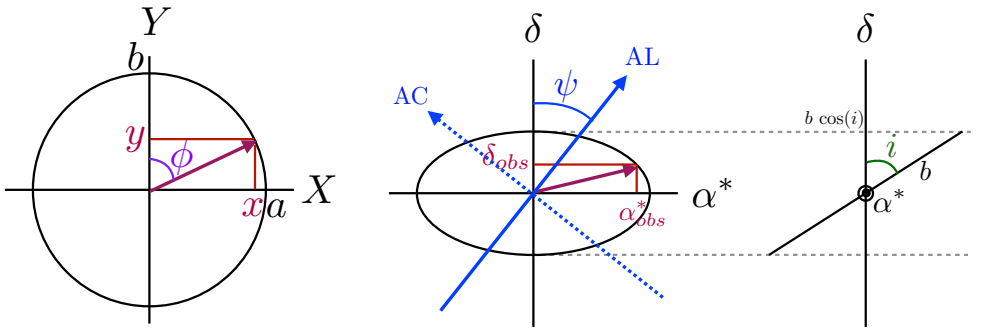

Fig. C.1. *Left:* Orbital plane ellipse with width a and height b (the circular case $a = b = 1$ is shown). *Middle:* Sky-projected plane with scan angle ψ and projected orbit due to inclination i shown in the right panel.

Appendix D: Biases and uncertainties of Thiele-Innes parameters

Appendix D.1: Biases introduced by fitting Thiele-Innes parameters to noisy data

All *Gaia* processing pipelines for fitting astrometric orbits[22] follow a similar parametrisation scheme (Sect. B.1; DR3 documentation; Halbwachs et al. 2022; Holl et al. 2022b): the three non-linear parameters P, e, and T_0 are fitted using different algorithms but the four remaining parameters are represented by the Thiele-Innes coefficients A, B, F, G, which linearise part of the equations.

Since the features in the distributions of DR3 orbit parameters hinted at signal-dependent effects, we simulated the A, B, F, G recovery performance as a function of noise level. We applied the same simulation approach as in Sect. 3.2 to compute the along-scan signal $w_{\rm k1}$ of the Keplerian orbit (Eq. (B.6)) for an ensemble of binary systems with the same distance, period, and semi-major axis. We computed the rectangular coordinates X and Y according to the simulated parameters and then solved the linear equation

$$w_{\rm k1} + \epsilon_w = (B\,X + G\,Y)\sin\psi + (A\,X + F\,Y)\cos\psi \qquad \text{(D.1)}$$

for the unknown A, B, F, G, where ϵ_w is a random noise term that we added to the noise-less simulated abscissa. For simplicity, we chose uniform abscissa uncertainties σ_w and zero covariances. We used a standard matrix-inversion solver[23] to determine the solution.

For the noise term ϵ_w, we chose its amplitude relative to the simulated semi-major axis, which was the same for all simulated systems ($a_0 = 0.059$ mas, see Sect. 3.2) but independent of the number of simulated observation epochs for a given source. For a signal-to-noise of S/N= 5, for example, a random noise term was added to w according to a normal distribution with dispersion $\epsilon_{w,5} = a_0/5$. This setup does intentionally not account for the inclination-dependent sensitivity (Sect. 3.2).

Figure D.1 show the simulated and recovered distributions of $\cos i$ for various levels of noise. At high S/N=100 the simulated distribution is recovered but for progressively smaller S/N a lack of face-on configurations starts to appear and the inclinations extracted from the fitted A, B, F, G are biased towards edge-on configurations. At very small S/N=0.01, where the A, B, F, G are essentially unconstrained except for their amplitude term dependent on a_0, the $\cos i$ distribution is peaked at $\cos i = 0$, i.e. edge-on configurations.

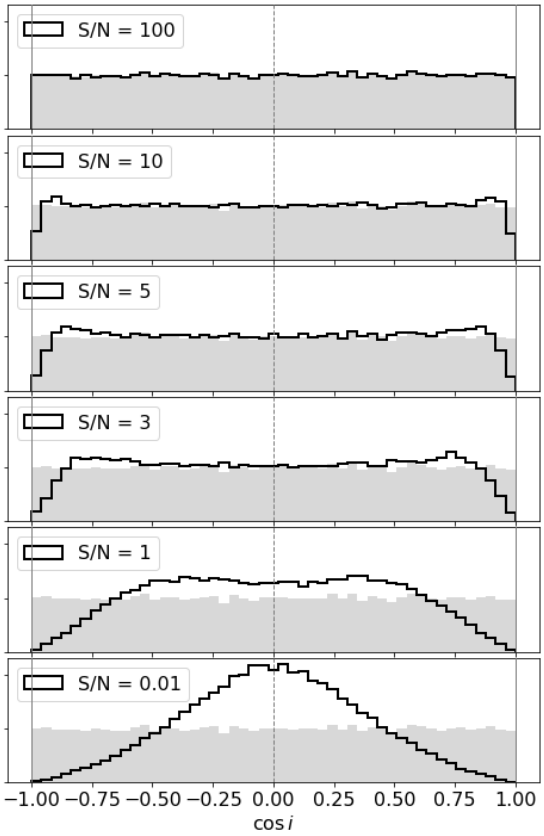

Fig. D.1. Simulated (filled grey) and recovered (solid line) distributions of $\cos i$ for six levels of signal-to-noise as explained in the text. The vertical dashed line at $i = 90°$ indicates the edge-on configurations.

The apparent dearth of face-on configurations for `Orbital` solutions (Fig. 11) is therefore the consequence of extracting the Thiele-Innes parameters A, B, F, G from noisy data. The dependence on S/N expected from the simulations is observed in the actual data as well (Fig. 12). Since the DR3 solutions contain a continuum of S/N levels, the corresponding $\cos i$ distribution is a superposition of the distributions for individual S/N levels.

Figure D.2 shows the recovered Ω distribution in the lowest S/N case we simulated. The suppression of orbits with $\Omega = 90°$ observed for `Orbital` solutions is reproduced by the simulation.

[22] There are three flavours: (1) the 'binary pipeline' (Halbwachs et al. 2022) (2) the Genetic Algorithm channel of the 'exoplanet pipeline' (Holl et al. 2022b) (3) the Markov Chain Monte Carlo channel of the 'exoplanet pipeline'.

[23] `https://github.com/Johannes-Sahlmann/linearfit`

This modulation becomes very weak for higher levels of S/N. We conclude that this feature can therefore also be attributed to a bias introduced by fitting the A, B, F, G coefficients.

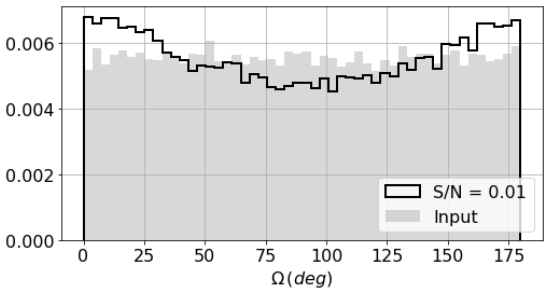

Fig. D.2. Simulated (filled grey) and recovered (solid line) distributions of Ω at S/N=0.01.

To simulate the effect on ω we simulated non-circular orbits with eccentricity $e = 0.5$, all other parameters remained the same. Figure D.3 shows a bimodal modulation of the recovered ω distribution. However, the minima at $\omega = 0°$ or 180° do not match the ones observed for `Orbital` solutions at $\omega = 90°$ or 270°. Instead, they reproduce the minima seen in the orb6 solutions shown in Fig. 11.

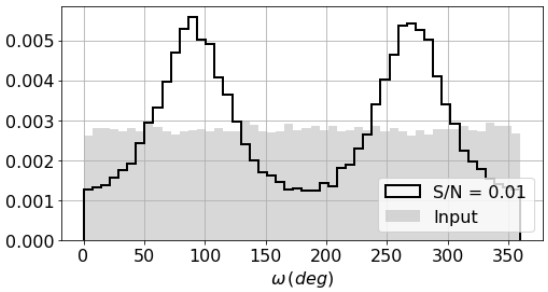

Fig. D.3. Simulated (filled grey) and recovered (solid line) distributions of ω for non-circular orbits with $e = 0.5$ at S/N=0.01.

Appendix D.2: Selection effect causing the modulation in the ω distribution

The accepted `Orbital` solutions have to pass a period-dependent threshold on their significance, defined as the ratio between the semi-major axis and its uncertainty a_0/σ_{a_0} (Halbwachs et al. 2022). Figure D.4 shows that there is a bimodal correlation between the published significance and ω with minima at $\omega = 90°$ or 270°. The application of an ω-independent significance threshold therefore leads to a suppression of solutions around these values. We argue that this is the explanation for the observed modulation in the ω distribution of *Gaia* `Orbital` solutions.

Appendix D.3: Geometric element conversion from Thiele-Innes parameters in the presence of uncertainties.

The archive tables list the fitted astrometric-orbit parameters P, e, T_0, A, B, F, G with their formal uncertainties and the `corr_vec` field contains the correlation strengths between those parameters. When converting A, B, F, G to geometric orbit elements and determining their uncertainties we therefore have to account for their covariances. This can be done with classical error propagation using some form of linearisation of the parameter dependencies or by Monte Carlo simulations. As also pointed out in Babusiaux et al. (2022), the distributions of the geometric parameters are often non-Gaussian, which favours the latter approach.

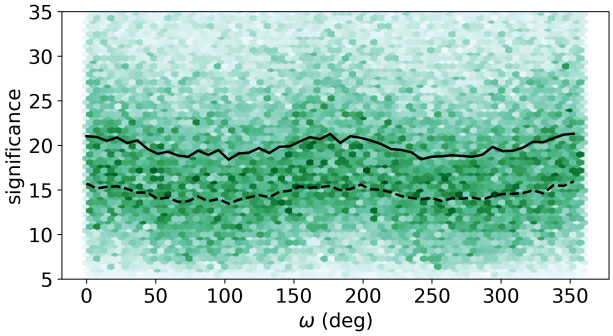

Fig. D.4. Density histogram of published significance as a function of ω for DR3 `Orbital` solutions. The solid curve shows the running median value. The dashed curve shows the median of the Monte-Carlo-resampled significance.

We used `Python` implementations of both methods[24] to investigate the value and uncertainty estimates of i, Ω, and ω for the non-circular `Orbital` solution in DR3. One finding is that the inclination uncertainty generally increases towards face-on configurations and that the linearised uncertainty estimate is usually comparable to the Monte-Carlo estimate, except for large uncertainties $\gtrsim 10°$ where the former is larger. There are only few cases where the discrepancy between the two different inclination estimates is larger than the linearised uncertainty.

The significance estimates using linearised error propagation can be different from alternative estimates that use Monte-Carlo resampling for obtaining σ'_{a_0}. These differences typically become important for solutions with poorly-constrained eccentricities (i.e. $e/\sigma_e < 1$) for which Monte Carlo resampling is not recommended because of overestimated variances of the Thiele-Innes coefficients (Babusiaux et al. 2022; Holl et al. 2022b). In Fig. D.4 we see that the correlation between the Monte-Carlo-resampled semi-major axis significance and ω is slightly weaker, i.e. has a smaller-amplitude variation, than for the published significance.

Appendix E: Primary mass computation

We use the PARSEC isochrones[25] (Bressan et al. 2012) with ages τ by steps of 0.01 in $\log(\tau)$ and metallicity [M/H] from –2 to 0.4 dex by steps of 0.05. Considering that the mass distribution of the isochrones is not uniform and that the age sampling is in log, weights need to be applied to each isochrone point i: $P(i) = P(\mathcal{M}, \tau, [M/H]) = P(\mathcal{M})P(\tau)P([M/H])$. For $P(\mathcal{M})$ we use the Chabrier (2001) IMF, for $P(\tau)$ a flat star formation rate and for $P([M/H])$ a Gaussian centered on zero with a dispersion of 0.05 so that by default the solar isochrones will drive the mass determination. The default mass sampling being too sparse at the bottom of the main sequence, we interpolated the isochrones with finer mass steps. We removed the lowest mass stars which present a step feature in the isochrone H-R diagram which is not observed in the *Gaia* DR3 HRD, so that the masses can only be

[24] `https://github.com/Johannes-Sahlmann/pystrometry` (Sahlmann 2019)

[25] http://stev.oapd.inaf.it/cmd V3.6

derived for $M_G < 14.4$ which corresponds to $\mathcal{M} > 0.1\,\mathcal{M}_\odot$. We also removed points outside a very crude age-metallicity relation that is $[M/H] < -0.4 - 0.05\tau$ for $\tau > 10$ or $[M/H] > 0.5 - 0.05\tau$.

Our observables are the absolute magnitude M_G and the colour $(BP - RP)_0$, noted below $\tilde{O}$. Through Bayes's theorem and considering that the isochrone point i contains the $\mathcal{M}$ information, we have:

$$P(\mathcal{M}|\tilde{O}) \propto \sum_i P(\tilde{O}|i)P(i) \quad \text{(E.1)}$$

To allow for small systematics in the *Gaia* photometry, we quadratically add a 0.01 mag error to the G, $G_{\rm BP}$, $G_{\rm RP}$ formal magnitude errors.

To avoid the presence of outliers in `azero_gspphot`, especially at the bottom of the main-sequence (Babusiaux et al. 2022), we use the 3D extinction map of Lallement et al. (2019) to provide an estimate of the extinction A_0. Most of the sources in the main-sequence are within the completeness limit of this map. A 10% relative error on the extinction with a minimum error of 0.01 is assumed. We derive the extinction coefficients k_G, k_{BP}, k_{RP} from the EDR3 extinction law[26].

We know that the position on the H-R diagram provides a direct estimate on the mass only for main-sequence stars. We therefore remove all isochrone points with PARSEC label = 0 (pre-main sequence stage) before applying Eq. E.1 and only provide a mass estimate for stars with more than half of the isochrone points at 3σ from the observables with PARSEC label=1 (main sequence stage). When several flux ratios are tested, the label of the smallest valid one is used for the main-sequence star selection. Therefore no mass estimate is provided for giant stars and mass estimates for pre-main-sequence stars will not be valid.

For each flux ratio F_2/F_1 tested, we obtain the absolute magnitude to be compared with the isochrones with:

$$M_G = G - k_G\,A_0 + 5 + 5\log(\varpi/1000) + 2.5\log(1 + \frac{F_2}{F_1}) \quad \text{(E.2)}$$

and the colour simply with $G_{\rm BP} - G_{\rm RP} - (k_{BP} - k_{RP})A_0$. Note that we do not consider the change in colour induced by the presence of the secondary. The mass is then fully driven by M_G. We consider that the resulting mass distribution obtained through Eq. E.1 is valid if we have more than 5 isochrone points within 3σ in both magnitude and colour to be compared with our star and if the closest isochrone point has a χ^2 p-value larger than 0.01.

Our derived masses are compared with the `FLAME` ones for systems with a small flux ratio in Fig. E.1. As expected those are fully consistent within the errors quoted, with less than 1% of 5σ outliers. For the small masses, we see the over-estimation trend of the `FLAME` masses due to the over-estimation of the GSP-Phot extinction for stars with $M_G > 7$ (Babusiaux et al. 2022), corresponding to $\mathcal{M} < 0.7\,\mathcal{M}_\odot$.

Figure E.2 shows the location in the HRD of the sources with an astrometric solution but no primary mass estimate obtained from our procedure. They have all been corrected by the extinction except those without an extinction estimate. Apart from giants, young stars above the main sequence are missed by construction as well as a few sub-dwarfs and sources too faint to have a reliable $G_{\rm BP}$.

[26] `https://www.cosmos.esa.int/web/gaia/edr3-extinction-law`

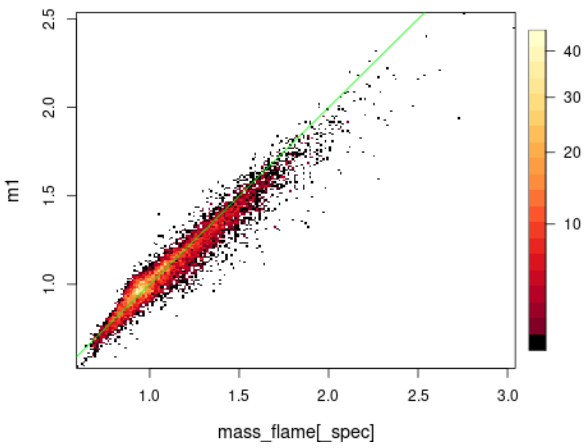

Fig. E.1. Density plot of the comparison between the primary masses derived here with the `FLAME` ones for systems with `fluxratio` < 0.01.

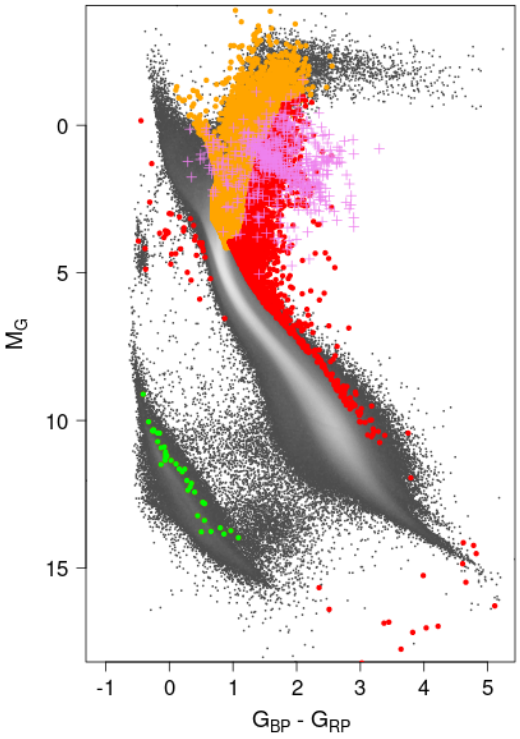

Fig. E.2. H-R diagram of the NSS astrometric solutions without a primary mass estimate. The grey background is the HRD of the full DR3 low extinction stars ($A_0 < 0.05$ according to Lallement et al. 2019), equivalent of Fig. 5 of Gaia Collaboration et al. (2018a)). The orange points are identified as giants. The red points do not have isochrone match. Violet + do not have an extinction estimate and un-corrected magnitude and colour are therefore used for those. Green points are the white dwarfs with a mass of $0.65\pm0.16\,\mathcal{M}_\odot$ assumed for Table 3.

Appendix F: Acronyms

Acronym	Description
2MASS	Two-Micron All Sky Survey
ADQL	Astronomical Data Query Language
AGB	Asymptotic Giant Branch (star)
AL	ALong scan (direction)
AP	Astrophysical Parameters
BH	Black hole
BP	Gaia Blue Photometer
CMD	Colour Magnitude Diagram
DoF	Degree(s) of Freedom
DPAC	Data Processing and Analysis Consortium
DR1	Gaia Data Release 1
DR2	Gaia Data Release 2
DR3	Gaia Data Release 3
EB	Eclipsing Binary
EDR3	Gaia Early Data Release 3
FLAME	Final Luminosity Age Mass Estimator
FWHM	Full Width at Half-Maximum
GALEX	GALaxy Evolution eXplorer
GoF	Goodness of Fit
GSPPhot	Generalised Stellar Parametriser PHOTometry
GSPSpec	Generalised Stellar Parametriser SPECtroscopy
GUCD	Gaia Ultra-cool Dwarf
HealPix	Hierarchical Equal Area isoLatitude Pixelisation
HPM	High Proper Motion
HRD	Hertzsprung-Russell diagram
IMF	Initial Mass Function
LMC	Large Magellanic Cloud
LPV	Long Period Variables
MAD	Median Absolute Deviation
MS	Main Sequence (star)
NLS	Non linear spectro
NS	Neutron star
NSS	Non-Single Star
PMa	proper motion anomaly
RGB	Red Giant Branch (star)
RMS	Root-Mean-Square
RP	Gaia Red Photometer
RUWE	Re-normalised unit-weight error
RV	Radial Velocity
RVS	Radial Velocity Spectrometer
SB	Spectroscopic Binary
SB1	Single-line Spectroscopic Binary
SB2	Double-line Spectroscopic Binary
SB*C	Circular orbit
SNR	Signal-to-Noise ratio (also denoted SN and S/N)
TBO	Two body orbits
UCD	Ultra cool dwarf (star)
UV	UltraViolet
VIMF	variable-induced movers fixed
WD	White dwarf